ULTRASOUND THREE-DIMENSIONAL SURFACE RENDERING WITH ELASTOGRAPHY-BASED FRACTURE LOCALIZATION OF THE SPINE

A Dissertation

by

PEER MOHAMED SHAFEEQ SHAJUDEEN

Submitted to the Office of Graduate and Professional Studies of
Texas A&M University
in partial fulfillment of the requirements for the degree of

DOCTOR OF PHILOSOPHY

Chair of Committee,	Raffaella Righetti
Committee Members,	Xiaoning Qian
	Aniruddha Datta
	Sevan Goenezen
Head of Department,	Miroslav Begovic

August 2018

Major Subject: Electrical Engineering

ABSTRACT

Ultrasound (US) has recently emerged as an attractive imaging modality for applications like accurate epidural placement and intraoperative guidance during surgeries. However, operators like anesthesiologists or surgeons untrained in US have difficulty interpreting the anatomy in noisy spinal US images. This problem is exacerbated by presence of fractures which is integral to the assessment of spinal cord injuries and stability. A method to automatically isolate and perform a 3D rendering of the spine anatomy from scanned US images is proposed. In the case of fractures, ultrasound elastography techniques are proposed by assessing the mechanical response to a uniaxial compression at the posterior vertebra-soft tissue boundary.

Experiments are performed by scanning the lumbar and thoracic vertebrae of 17 healthy volunteers BMI ranging from 19.5 to 27.9. A local phase-symmetry technique is applied to the US B-mode images for enhancement of bone-like ridges and the spine blobs are subsequently classified. The segmented spine surface from the blobs is compared against the radiologist's manual delineation of the spine surface. This performance assessment analysis is also consequently extended to 3D surfaces. For investigating spine fractures, experiments are performed on ex-vivo rabbit lumbar spine samples. 3D finite element models of the vertebra-soft tissue complex are generated to simulate axial normal and shear strains. Also, experiments on the same samples are performed to corroborate simulation findings. The numerical characteristics of axial strain's spatial distribution are further used to construct two shape descriptors to make inferences on spinal abnormalities.

The proposed techniques accurately generate a 3D surface rendering of multiple vertebrae specifically showing landmarks like the laminae, ligamentum flava, spinous, transverse and articular processes. These techniques are also extended for bone regeneration applications which has implications for the monitoring of postoperative bone healing. Results from studies on spine fractures indicate that the disruption of axial strains manifest as distinct patterns around intact and fractured vertebrae. These along with the shape descriptor features resulting from the surrounding soft tissue deformation can serve as a useful adjunct to B-mode images in uniquely determining the location of fracture sites.

DEDICATION

To my parents.

ACKNOWLEDGEMENTS

If my stumbling has created even the tiniest dent in this field of ultrasound image analysis, it is all thanks to two individuals' instrumental to the success of this work: my advisor Dr. Raffaella Righetti and my father P. Shajudeen.

I would like to first thank my advisor Dr. Righetti for her unending wisdom, creativity, guidance and, most importantly, encouragement. Her immense wealth of knowledge in ultrasound imaging, signal processing and tendency to dream big with a greater sense of purpose in saving lives has been the backbone for this work. She incubated an intellectually stimulating and conducive environment for maximizing my creative output. There are also aspects from her character I try to emulate like her kindness, her infectious enthusiasm and energy brimming with positivity. Her willingness to listen with tremendous humility while fostering a judgement-free environment is, dare I say it, a rare quality in my limited purview of academia.

I would like to thank my father who has, needless to say, been an inspiration to me my entire life. In innumerable ways, my father essentially paved the path for my education in leading to this PhD. My penchant for research would not have been possible without his dedication and hard work especially during my formative years of math and science training. This could have been as tedious as driving me around for several hours in the sweltering middle eastern heat for tutoring or as memorable as teaching me the value of handling failure with grace.

There is no greater attribute to completing a long and arduous PhD journey than perseverance. My mother has always been the walking embodiment of this quality. I would like to thank my mother for constantly trying to instill this in me along with her limitless stream of duas and support. Another person who essentially took the place of my mother during all these years of higher education has been my sister. I would like to thank her along with my brother and my brother-in law for being a constant source of reprieve during this journey. Of course, my niece and nephew share a sizeable portion of this credit (also who at times have helped me in the form of manual labor).

I would also like to particularly thank my academic peers and professors, discussions with whom many ideas were borne into fruits scattered throughout this work. My lab colleagues undoubtedly deserve a large portion of this acknowledgement. In each of these individuals, I have admired their unique abilities: Songyuan's relentless work ethic, Anuj's critical and big picture thinking, Namhee, Tauhid and Xu's methodical approach to engineering solutions, Sanjay and Alfredo's reductionist approach to learning and Biren's straight shooting. My committee members Dr. Qian, Dr. Datta and Dr. Goenezen have played an important role in providing feedback. Conversations with Dr. Braga-Neto, Dr. Yoon and Dr. Dougherty have also been vital to my machine learning knowledge base. I would like to thank Dr. Cabrera, Dr. Van Eps, Dr. Tasciotti, Dr. Weiner and the CMP team at Houston Methodist Research Institute for their invaluable clinical input and samples. I would like to thank my friend Chin for talking me through many ideas in computer vision during my foundational years and also being an adventure partner in appreciating many a vista across state lines. I would also like to thank Dr. Villareal for his invaluable career advice and allowing me in having a taste of capstone design. Also, the value of

the wider open-source community in disseminating knowledge on platforms like Github and Mathworks file exchange cannot be underestimated.

Like dreams that perform the crucial reset function in helping us cope with our memories and emotions during the day, my friends served an equivalent purpose. Many of them have made quite an impact in my well-being that I cannot possibly name all of them. Of the memorable culprits, I would like to thank Alfredo, Chadi, Chris, Harshad, Shibin, Siddharth, Somreeta, Thanh and The Crew (especially Faisal, Mak and Shiv in my later years). I would also like to thank Fred, Maxine, Nelson, Steve and Sushil who have made lasting impressions at some point during my journey.

Last and most definitely not the least, I would like to thank my beautiful wife Farzana for providing me with my daily dose of oxytocin. She joined me at a critical point but made, what seemed unlikely, a seamless transition. I am indebted to her unfettered willingness to pick up the slack with a smile and even proof-read my papers. Suffice to say, akin to a sleight of hand, she jumpstarted my motivation to complete this degree.

CONTRIBUTORS AND FUNDING SOURCES

Contributors

The mechanical simulations incorporating finite element modeling depicted in Chapter 5 were conducted by Songyuan Tang of the Department of Electrical and Computer Engineering and Namhee Kim of the Department of Mechanical Engineering. All other work conducted for the dissertation was completed by the student independently. Mr. Daryl G. Schulz of the Preclinical Catheterization Lab at Houston Methodist Research Institute performed the CT scans on samples used in this study.

Funding sources

This work was supported by funding from the Department of Defense (grant W81XWH-14-1-0600, Log #SC130156). *In vivo* data acquisition was approved by the Texas A&M University, Human Research Protection Program (IRB #2014-0461D).

NOMENCLATURE

2D	Two-dimensional
3D	Three-dimensional
3NN	Three nearest neighbors
ANSE	Axial normal strain elastography
AP	Articular Process
ASSE	Axial shear strain elastography
ASE	Acoustic shadowing energy
BMI	Body mass index
CT	Computed Tomography
FE	Finite-element
IQR	Interquartile range
LF	Ligamentum flavum/dura mater complex (epidural space)
MAE	Mean absolute error
MI	Mean Intensity
PLC	Posterior ligament complex
PSRE	Phase-based ridge enhancement
PSF	Point spread function
RF	Radio-frequency
SNR	Signal-to-noise ratio
SP	Spinous Process
SRRM	Shadow region row means
TP	Transverse Process

US	Ultrasound
USE	Ultrasound Elastography

TABLE OF CONTENTS

LIST OF FIGURES

LIST OF TABLES

CHAPTER 1

INTRODUCTION

1.1 OBJECTIVE

This thesis is concerned with detection, localization and three-dimensional (3D) visualization of structural information about the spine using volumetric ultrasound data. This can be useful for medical personnel untrained in ultrasound in easily interpreting spinal anatomy for inferring fractures, abnormalities or in providing guidance for intraoperative imaging. This work focuses on the automated extraction of the 3D spine surface and highlights spinal abnormalities by utilizing information from surrounding soft tissue deformations. Although the clinical utility of this work is demonstrated for the spine, there are potential implications for this work by extension to long bones. These could serve as a useful addendum to a software framework within a portable ultrasound imaging system. This could also serve as part of a larger workflow in computer assisted surgery systems for which surgical instruments can be guided using precise real-time feedback from visualizing the 3D spine volume.

1.2 THE NEED FOR SPINAL ULTRASOUND IMAGING

The spinal cord is the central communication link between the body and the brain. Pain is one such signal that is linked to the brain. Administration of regional anesthesia before surgical procedures suppresses the pain by numbing this link. However, needle placement is hindered by a protective bony cage known as the spine or vertebral column. Anesthesiologists generally palpate to find an intervertebral portion of the back between two protruding spinous processes (the backbone that can be felt). Such anatomical landmarks can be challenging to obtain from obese or pregnant patients. Thus, medical imaging plays a critical role in identifying such

structures. Clinical diagnosis of spinal cord injuries, spinal fractures or abnormalities is achieved through the use of imaging modalities. Spinal imaging methods are used for the localization of the injury or the fracture, the assessment of diagnostically relevant details, the assessment of risk or probability of injury, the monitoring of bone healing or regrowth and the evaluation of treatment outcomes [1-3] . In several of these applications, imaging plays a critical role to improve the diagnosis and treatment of the spinal pathologies, monitor the associated tissue response to the underlying etiology, and provide anatomical insight before or during spinal procedures.

Spinal fractures and abnormalities are typically evaluated using computed tomography (CT), while magnetic resonance imaging (MRI) is used to assess soft tissue trauma and spinal cord injuries [4-7]. The strength of these modalities lies in their superior sensitivity and specificity; the weaknesses in their requirement of large, often structurally fixed, machinery, the need for specially trained technicians to take and develop images, the high costs and, in the case of CT imaging, the reliance upon radiation for image generation [8, 9]. While these methods are currently the gold-standard for spinal imaging applications, some of their drawbacks make them unattractive for applications such as pediatrics, military and regeneration studies using stem cells [10]. The effects of radiation exposure in patients from fluoroscopy (c-arm), computed tomography (CT) and nuclear medicine have been well documented. CT scans of the spine are associated with substantial exposure compared to extremities (dosage of 18 and 19 mSv for thoracic and lumbar CT scans respectively) [11-13].

Spinal ultrasound imaging has emerged as an important player for image-guided procedures due to its real-time imaging feedback in addition to the modality being highly portable. Moreover, it is known for not producing ionizing radiation and being relatively cost-effective. An area where a lot of work has been concentrated on is the use of ultrasound in guiding epidural placement. In Fig 1.2, the graphic demonstrates epidural administration at the L3-L4 interspace. The objective of an anesthesiologist is to identify the appropriate interspace followed by an estimation of the optimal puncture depth i.e. the distance from the skin to the epidural space. US facilitates exact identification of the epidural spaces within which optimal puncture depth can be determined.

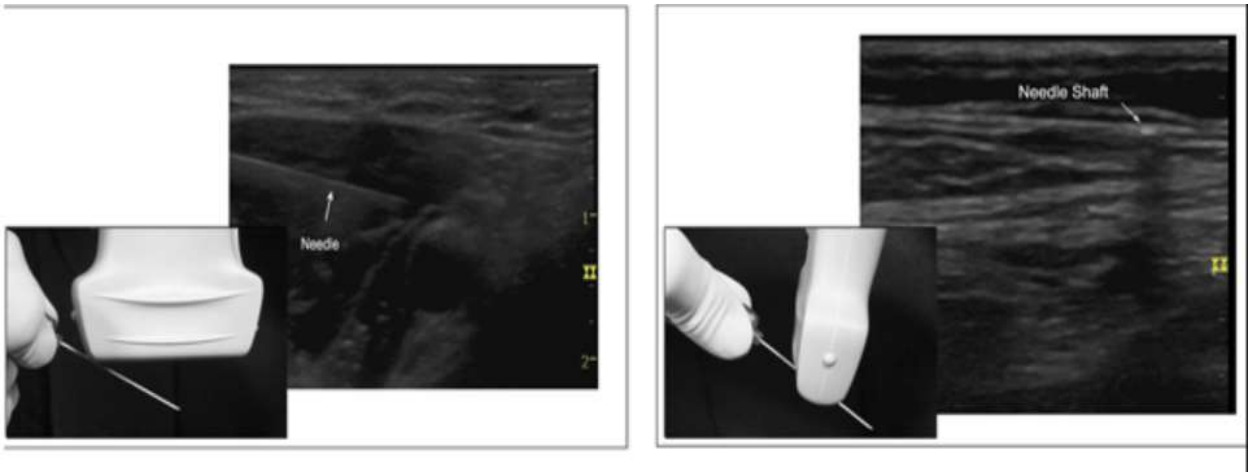

Fig 1.1. The process of planning the epidural with needle visualization shown in the US image. The transverse view is shown on the right and the paramedian view on the left. [Printed with permission from The New York School of Regional Anesthesia (NYSORA) (http://www.nysora.com)].

US has been successfully used in addressing the need for accurate epidural placement [2,3,6,7]. However, the learning curve for anasthesiologists has not been established to fruition [7]. There are two approaches to performing spinal US scans. Scanning along the transverse plane involves placing the US probe perpendicular to the long axis of the vertebral column, and the paramedian

plane involves placing the US probe parallel to the long axis of the vertebral column while tilted at an angle. These methodologies are shown in Fig 1.1. The anesthesiologist/operator would first identify the appropriate interspace level using the paramedian approach and then place the transducer along the transverse plane when administering the epidural or spinal. Most of the related literature has focused on using the paramedian approach for identifying lumbar interspace levels [14-17]. However, the transverse plane approach, which is predominantly used in obtaining the US images for this paper, has been found to be preferred method for the accurate estimation of the insertion point [18]. This is due to easy identification of the depth from the skin to the ligamentum flavum. Despite its potential advantages, US has not yet become the standard-of-care due to the difficulty interpreting spinal anatomy by anesthesiologists untrained in ultrasound [19].

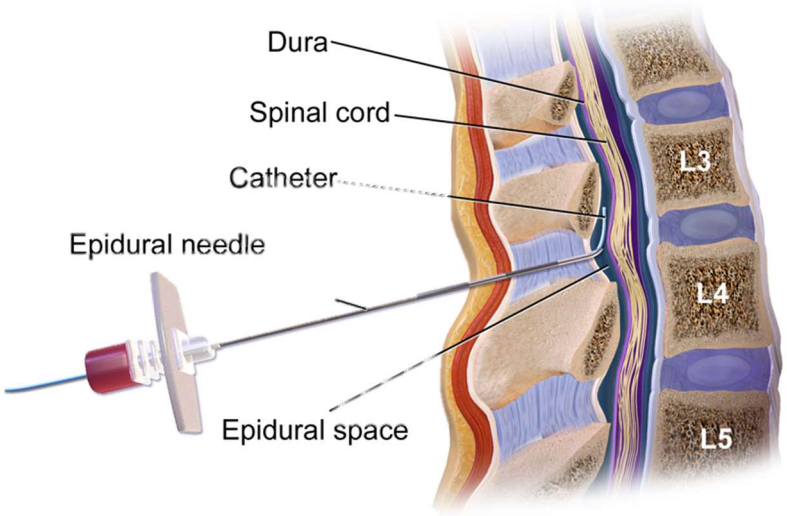

Fig 1.2. Epidural administration at the L3-L4 interspace. The needle is punctured onto the epidural space to induce numbness generating pain relief. [Reprinted from Wikimedia Commons licensed under the Creative Commons Attribution 4.0 (https://commons.wikimedia.org/wiki/File:Epidural_Anesthesia.png)]

Another area for which US is gaining traction are in spinal fusion surgeries involving pedicle screw fixation for stabilizing the spine. Fusion surgeries are performed for a wide spectrum of indications, including correction of degenerative disc deformities, spondylolisthesis, trauma, infection, tumor, and congenital anomalies such as scoliosis [20-21]. It works by fusing two vertebral segments (adjacent vertebrae) with a bone graft material which acts as a scaffold to promote bone growth. Spine surgeons also use bone graft for spine fracture reduction. These procedures require fluoroscopic image guidance in establishing the locations for implanting the screws. But fluoroscopy poses a radiation risk to everyone inside the operating room. Also, depending on the experience of the surgeon multiple fluoroscopic planes may be captured to determine anchor point positioning compounding this risk. In practice, a significant degree of uncertainty arises in determining the pose of 3D objects from 2D projection images and under some circumstances this can lead to inaccurate navigation [22].

Position tracked US images obtained intraoperatively can be aligned with the preoperative CT in determining precise location for screw placement. Consider the important example of posterolateral gutter fusion surgeries, which are procedures in which the screws are placed at the posterolateral sides to help align the spinal anatomy and restore normal movement of the vertebrae. Fig 1.3 shows a posterolateral aspect of the procedure with screws on the sides. Bone graft material from either the patient's body or a cadaver is then placed posterior to the screws to fuse the vertebral segments. It also shows grafting at the empty space in place of the removed disc between the vertebral segments to account for cases like degenerative disc disease. The assessment of bone integrity and growth facilitated by the grafting postoperatively can have important implications in bone healing applications.

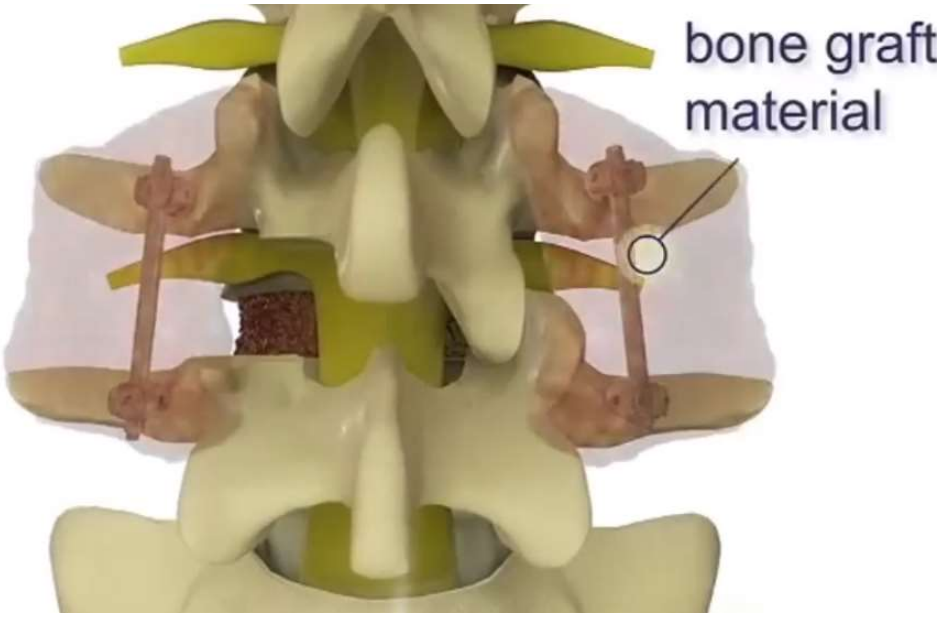

Fig 1.3. Spine fusion surgery with implanted screws on the sides for stabilization. Bone graft is placed on top to fuse the vertebral segments and in between for disc repair. [Reprinted from "L4-L5 and L5-S1 TLIF for Multi-level Bilateral Foraminal Stenosis" by Henry Dimaano (https://vimeo.com/88443576)]

Fig 1.4 shows the manner in which a cross-sectional portion of the US image is obtained (Fig 1.4a) from an L3 level of the lumbar vertebrae and fed back to the system (Fig 1.4b) in the form of a "brightness" mode or B-mode image. Note that the posterior, middle and anterior columns is a simple division of the vertebral column proposed by Dennis for classifying the types of spinal fractures [23]. The middle and anterior columns represent the vertebral body of the spine. Each lumbar vertebra (Fig 1.4a for instance) has four protrusions facing the ultrasound transducer: The spinous process (SP) located at the midline, two articular processes on the left and right of the SP and two transverse processes on the left and right at the extremes. The laminae constitute the relatively level regions between these protrusions. Each articular process (AP) lies at the junction

between the respective transverse process (TP) and the bottom pedicle that connects to the middle column. The superior AP of one vertebra is connected to the inferior AP of the successive vertebra using facet joints.

Acoustic waves from the transducer are emitted, which are then absorbed and reflected by multiple interfaces including connective tissues, fat and muscle layers below the skin. Bony regions, proportional to the material density, almost completely reflect the acoustic waves indicated by a bright hyperechoic line. This results in a dark region underneath the strongly reflective bone surface producing what is known as acoustic shadowing (seen below the SP, AP and TP in Fig 1.4b and below SP and laminae in Fig 1.5). Thus, US limits image visibility to the surface of the posterior column of the spine and the posterior side of the middle column surface within the interspaces. In other words, what the image ends up showing is the top boundary of the posterior column (where the arrows touch in Fig 1.4a) above each vertebra and the top surface of the middle column (shown in light blue) in between vertebral segments.

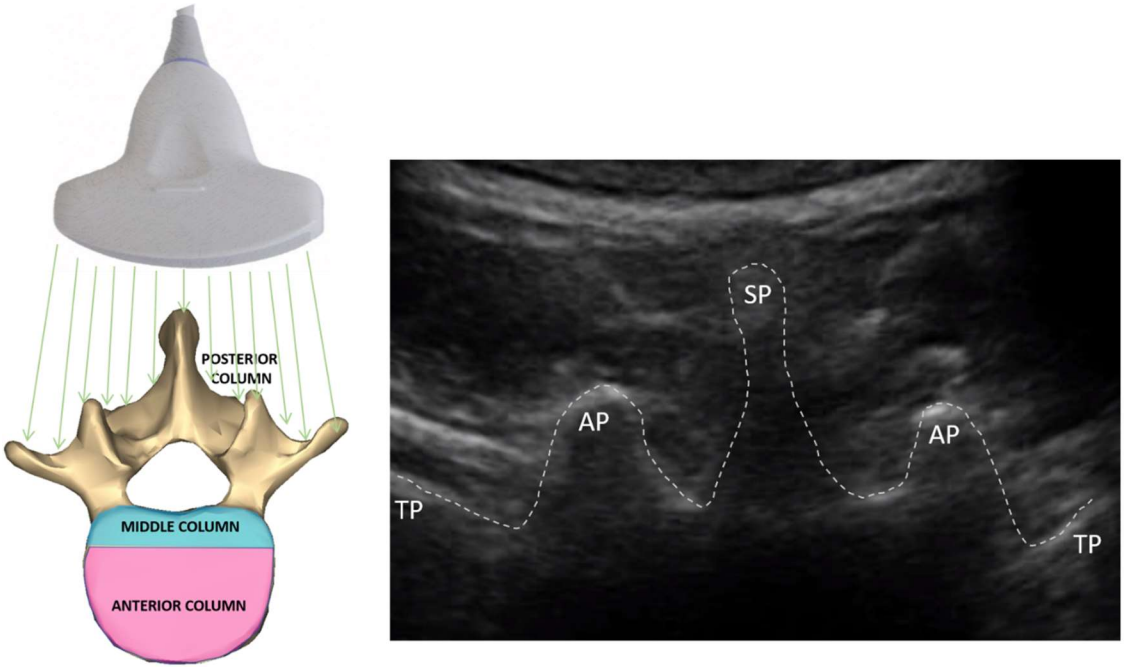

(a) (b)

Fig 1.4. (a) 3D cross-section of a single vertebra. (b) Associated US image at the L3-L4 with protrusions highlighted.

Epidural placement, pedicle screw placement and monitoring of postoperative bone growth require the identification of structural landmarks from the spine surface. But the spine has a peculiar geometry compared to the smoother, more curvilinear, bones in the body. The posterior column anatomy varies its geometric structure across multiple slices taken in the transverse plane within a single vertebra. So, such structural landmarks can be incredibly challenging to interpret for an operator untrained in ultrasound physics and spine anatomy. For example, Fig 1.4 and 1.5 are displaced 0.5 mm apart in the elevational direction but have varying geometries. More to the point, US imaging generally has a poorer visual quality and a low SNR compared to other modalities. Obese and/or muscular patients may have multiple layers of fat, dense connective

tissue and muscle posterior to the vertebra exacerbating problems in image interpretation. This could result in not all structures being evenly distributed by high intensity line profiles. Contrast variations may occur with increased depth. This can be seen in Fig 1.4b and Fig 1.5 which do not show bright intensities at the SP region and this is obtained from a healthy patient of BMI 22.5.

Diagnostic ultrasound is generally disseminated in the form of 2D cross-sectional views of the 3D anatomy. A 2D viewpoint may be insufficient in capturing the anatomy comprehensively. Ultrasound artifacts present in the image also cloud the operator's judgments in inferring the existence of certain structures. For example, it is unclear from the 2D slices exactly how much acoustic shadowing has to be present in an image to judge the existence of a bone surface above it. An operator may interpret any amount of shadowing within an image as evidence for existence of the SP. In these cases, a 3D spine rendering can provide the operator with multiple viewpoints. Thus, the operator can have a better understanding correlating the anatomy with a typical spine model.

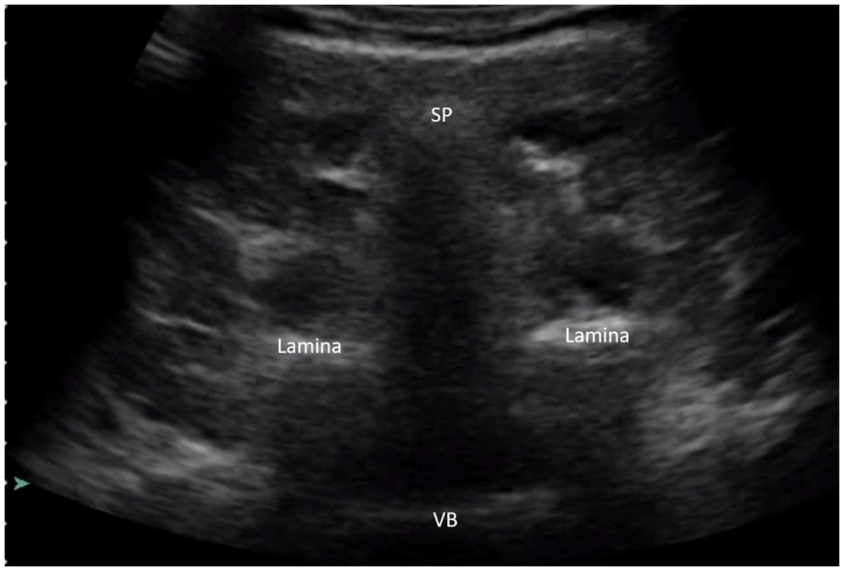

Fig 1.5. US image at the L3-L4 interspace.

Spinal fractures complicate the above issues even further. Based on the fracture orientation and gap size, the low resolution and brightness may not be sufficiently capture it. Spinal cord injuries are often associated with spinal fractures and musculoskeletal abnormalities. Initial mechanical trauma for spinal cord injury includes traction and axial compression forces, hyperflexion and rotational stresses, which may result in vertebral column fractures, lower extremity fractures and dislocated bone fragments. Post-traumatic imaging of the spine and the soft tissue in proximity of the spine provides essential information for accurate diagnosis and prognosis of spinal and spinal cord injuries and may be used to assess treatment efficacy. In most cases, spinal injury due to fracture, often resulting from trauma or conditions such as osteoporosis, are associated with changes of mechanical properties of the tissue at the bone interface [25]. However, there is a no available literature investigating fractures in the context of US imaging.

The above applications stress the need for extracting structural information from the vertebrae to paint a clear picture of the anatomy. Such information could serve as landmark points in preoperative surgical planning, intraoperative surgery and postoperative monitoring of the bone healing process. This thesis serves to convert noisy spinal US images to an interpretable form for any medical personnel with minimal US training.

1.3 APPROACH

As mentioned above multiple factors can affect an observer's interpretation of bone in US images. Automatic delineation purely based on some function of brightness can be limiting especially with the variations that can arise from different contrast levels, transducer physics-based artifacts and inherent noisy conditions. We make a case for the isolation of important anatomical *features* that are invariant to such conditions. A prominent approach to the problem of bone segmentation has been the use of phase-based estimation [22, 26]. The approach has gained a lot traction due to the robustness offered by invariant measures such as local phase symmetry and phase congruency particularly for applications involving extraction of low-level features. The following paragraph provides a rationale for using this technique.

Consider the US image in Fig 1.4. Each column represents the signal output of an acoustic wave that has had "interactions" (reflections, refractions etc) with each tissue layer starting its path from the transducer on top. This signal has both energy and structure. We can achieve separation of energy and structure in a real-valued signal $f(t)$ by virtue of its analytic signal $f_a(t)$. This is done by introducing the purely imaginary part of the signal which is its Hilbert transform $f_h(t)$ such that:

$$f_a(t) = f(t) + f_h(t) \qquad (1)$$

This allows us to decompose the signal into local amplitude (energy) and local phase (structure):

$$f(t) = |A(t)|.\exp\big(\varphi(t)\big) \qquad (2)$$

Where, local amplitude is given by:

$$A(t) = \sqrt{f(t)^2 + f_h(t)^2} \qquad (3)$$

And local phase is given by:

$$\varphi(t) = \tan^{-1}\left(\frac{f_h(t)}{f(t)}\right) \qquad (4)$$

Energy and structure are independent information contained in a signal unless the signal is a combination of partial signals with different local phases on different scales [27]. In other words, the polar decomposition in Eqn (2) makes it possible to separate the original signal into partial signals due to band-pass filtering that removes signals with non-linear phase and in turn preserves the invariance property. We will use the Log-Gabor filter consistently in this thesis to provide band-pass filtered local amplitude and phase information. More details are provided in Chapter 1.

The phase information will in turn be used to extract structural information about the signal or rather local phase will enable us to use the signal's *features* as opposed to the signal intensity. However, phase-based techniques are extremely prone to the influence of noise in the signals. A fundamental operation to isolating noise in a signal is thresholding its amplitude. But, how do we create a methodology for thresholding signal structure? One parameter considered in this thesis is the width or *scale* of the band-pass filter used in the phase estimation. And since a US

image is a concatenation of the acoustic signal outputs to form a 2D signal, directionality or *orientation* of the filter is also considered. Moreover, isolation of the bony regions in US images requires removal of surrounding tissue structures in addition to the noise arising from local phase. This now become a *classification* problem of which feature engineering is a key aspect.

A discriminating aspect of bony regions observable in Fig 1.4 and Fig 1.5 is the shadowing feature immediately following the spine surface. This can provide some insight into the overall morphology of the spine surface. Therefore, this is an important feature that is incorporated in the algorithm for discerning the spine regions from the surrounding tissue structures. Note that any amount of shadowing is characterized by its low signal amplitude underneath the bone surface. Thus, an intensity-based method should suffice for extracting this information (see Chapter 1).

The robustness of the above methods can fail in the presence of fractures due to the further complications of the spine geometry and the signal affected as a result. A solution to this problem is to look for additional features that can be extracted from the surrounding tissues. Investigating the degree of soft tissue deformation around the bone can provide an insight into the bone integrity and thereby fractures and abnormalities.

1.4 THESIS OVERVIEW

Chapter 2 reviews the major work done in the field of automatic long bone and spine segmentation in US imaging. An important difference from the existing techniques is the

applicability of the proposed method to the spine geometry that takes on a complex structure. Structural information such as the SP, AP, TP, laminae and epidural space is obtained. Bone-like regions are first obtained by a local 2D phase symmetry features and followed by a classification of the spine regions. Overlaying automatically obtained structures onto the ultrasound image can help guide an operator in epidural placement. The advantage of the proposed technique is its minimal reliance on algorithm parameters and thus generalizes well for the in vivo experiments.

Chapter 3 extends the work in Chapter 2 by obtaining structural information of the spine and performing a 3D reconstruction of multiple vertebrae. A survey of the previous literature in 3D rendering within the context of visualizing the bone surface is done. The comparison also yields evidence that this is the first body of work in extracting the 3D surface rendering of the spine. A statistical analysis highlighting the accuracy assessment of the surface rendering against a manual surface delineation by an expert has been proposed. Furthermore, the 2D local phase symmetry technique has been modified to obtained 3D local phase symmetry features for the context of bone regeneration.

Chapter 4 discusses an approach using ultrasound elastography by incorporating surrounding soft tissue deformations in localizing spinal fractures. It is important to note that is the first body of work done in visualizing posterior spinal fractures within the context of US imaging. Strain-based shape descriptors constructed from the unique spine geometry are also proposed to make inferences on spinal abnormalities and fractures.

Finally, Chapter 5 concludes the work and discusses the areas that might be developed for future work.

CHAPTER 2

SPINE SURFACE DETECTION FROM 2D LOCAL PHASE-SYMMETRY ENHANCED RIDGES IN ULTRASOUND IMAGES*

2.1 INTRODUCTION[1]

Spinal ultrasound (US) has known to offer many potential benefits for intra-operative surgery scenarios. This can be attributed to some of the distinctive qualities of US such as portability, safety and cost effectiveness. US has been used as a screening tool for administering spinal injections [1]. Epidural anesthesia is performed in 75 percent of all childbirths in the United States with a 70 percent failure rate among obese patients [2]. Regional anesthesia for placement of the epidural needle relies on palpation of anatomical landmarks, but the optimal puncture depth cannot be determined from inspection or palpation especially for obese patients. This can result in patient discomfort, accidental dural puncture and potential trauma to the nerves, vessels, bones and ligaments [3]. Multiple insertion attempts could result in nerve damage causing epidural abscess infection [4]. Other complications of neuraxial anesthesia involve spinal hematomas, bleeding diathesis and left ventricular outflow obstruction. X-ray based fluoroscopy is the only competing real-time intra-operative modality with US [5], but it is not portable and uses ionizing radiations.

Spine surface detection in US images requires a robust bone segmentation technique that reduces the influence of the soft tissue interface and ultrasonic imaging artifacts (reverberation, speckle, etc.). A bone feature is a hyperechoic line profile with a perceivable level of posterior acoustic

*Reprinted with permission from "Spine surface detection from local phase-symmetry enhanced ridges in ultrasound images" by Peer Shajudeen and Raffaella Righetti, 2018. Medical Physics, Volume 44, Issue 11, Pages 5755-5767, Copyright 2018 by American Association of Physicists in Medicine.

shadowing (black region) underneath the feature. Fig. 2.2 shows an ideal segmentation of the lumbar spine (bone feature) for an US image obtained using the transverse plane approach.
This level of continuity in the spine line profile is rarely possible. The intensity along the ideal line profile between the laminae and the spinous process is not sufficiently pronounced, which leads to a large discontinuity in the automatically segmented image.

US bone segmentation has been extensively investigated in the past. US images of bones usually feature non-uniform intensity due to scattering between bone-tissue interfaces. Therefore, simple intensity-based thresholding methods are, in general, inadequate for US bone segmentation. Some groups have employed intensity information and gradient-based operators for the segmentation. However, these methods are sensitized to machine setting parameters (operating frequency, gain, and acoustic power), which affect the image contrast and resolution. US artifacts and high curvature bone anatomy also affect the hyperechogenecity of the bone surface. For example, Kowal *et al.* proposed a fast-automated bone contour detection algorithm where a higher intensity weighting is applied for deeper structures [33]. While the method may be suitable for deep bony regions that may have non-uniform intensities, the merging of large area connected components may not work for bone fractures or a discontinuous spine line profile. To address this limitation, *a priori* knowledge about the bone appearance has been incorporated into the bone contour modeling criteria, but this can be limiting when applied to the complex geometry of a spine especially in the transverse view [34-37]. Due to the large discontinuities in the hyperechogenecity of the spine line profile, especially between the laminae and the spinous processes, evolving a contour can result in it veering out of the spine boundary constraints. Active contour techniques are also susceptible to

contrast and intensity variations due to the intensity gradient influence on the external energy term in the models.

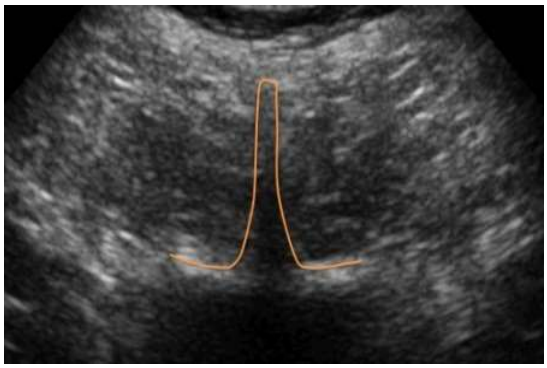

Fig.2.1. Lumbar spine region given in orange on a US image obtained in the transverse plane

Elastography has been suggested as a potential aid to ultrasonography for bone surface localization due to the high mechanical contrast between bones and surrounding soft tissue, but it has not been investigated for spinal applications yet [38-40]. Strain patterns in proximity of spines may be affected by the complexity of the spine geometry as well as adjoining soft tissues, erector spinae muscles and ligaments conjoined with the laminae, transverse and articular processes that lie deeper down the skin surface.

Local phase-based localization of the bone surface has gained a lot of traction in recent years due to its robustness from using intensity invariant measures. Hacihaliloglu *et al.* and Hacihaliloglu *et al.* used a Log-Gabor filter based phase-symmetry measure to produce a strong response on the bone surface [41-42]. The automated parameter estimation technique for Log-Gabor filters attempts to suppress non-bone responses elsewhere in the B-mode image but is prone to false

positive bone responses at soft tissue interfaces that have similar intensity profiles as the bone surface [26, 41-42].

Little attention has been paid to spine surface segmentation in US images especially those obtained in the transverse plane. Khallaghi *et al.*, Behnami *et al.*, Rasoulian *et al.* and Nagpal *et al.* have incorporated statistical shape, pose and scale priors obtained from segmented vertebral CT slices co-registered with spinal US images [43-46]. Since the spinal US images have no prior enhancement, the quality of the vertebral features used for registration depends on the intensity profile of the spine surface. Hacihaliloglu *et al.* overcame this limitation by using phase-based localization as applied to spine surfaces [47]. Despite the promising results of laminae enhancement, the influence of soft tissue was still evident. In some cases, this was reduced by the addition of bottom-up ray casting, which could fail in the presence of non-zero intensities following the bone surface. Tran and Rohling have proposed the use of a lamina template to detect laminae obtained using phase-based localization [14]. Both techniques are restricted to work for paramedian plane images. Yu *et al.* proposed a template-based technique to detect the epidural space in transverse plane images, but this technique may be sensitive to contrast and gain parameters set in the machine [48]. In addition, template-driven techniques are restricted to work for lumbar anatomy and are not scalable to structural changes in the vertebra. Berton *et al.* developed a spine detection algorithm for the transverse plane deriving features like phase symmetry, rupture points for shadowing and texture descriptors to classify the spinous process and acoustic shadow [49]. This technique is restricted to detecting the spinous process region, which is beneficial for scoliosis measurement. The authors did not demonstrate a procedure for extracting other anatomical structures characteristic of the vertebrae such as the laminae.

A fully automatic spine surface segmentation technique that detects spine surface regions such as spinous processes, articular processes, transverse processes, laminae and also dense fibrous tissue like the ligamenta flava-dura mater interface (LF) for US images obtained in both the transverse plane and paramedian plane has been proposed. The novelty of our method lies in the feature development for the design of our classifier that detects the spine surface regions. Potential applications of our technique include:

- Superimposing the detected spine surface line profile on the B-mode image in the transverse plane enables easy visualization of the skin to LF distance/puncture depth facilitating accurate epidural placement.
- The 2D images post-spine surface detection along with position coordinates information can be stacked together to perform 3D volume reconstruction of the vertebral column.

2.2. METHODS

2.2.1. Speckle Reduction using a First-order Statistics Filter

Degradation of US images can rise from speckle, which can be modeled as locally correlated multiplicative noise. Speckle is caused by the constructive and destructive interference between US waves scattered from tissues. A linear filter using first order statistics such as local mean and variance from sliding window operations has been proposed for speckle reduction [50]:

$$f(x,y) = \bar{I_n} + \left[\frac{\sigma_n^2 - \sigma^2}{\sigma_n^2}\right](I(x,y) - \bar{I_n}) \qquad (5)$$

where $f(x,y)$ is the speckle reduced pixel, $I(x,y)$ is the pixel intensity from the original US image and σ^2 is the variance of the original US image. Local statistics such as mean and variance of the 3×3 pixel neighborhood of $I(x,y)$ are given by $\bar{I_n}$ and σ_n^2, respectively. The speckle-reduced

image (an example is shown in Fig. 2.3b) is normalized between zero and one to enhance the contrast of the image. The speckle-reduced image is the input to the ridge enhancement and classification steps of the algorithm and will be termed as the "US image" in the remaining of the paper.

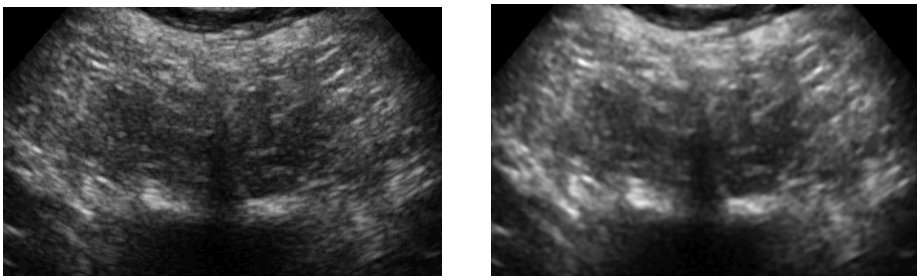

(a) (b)

Fig. 2.3. (a) Original 2D US image of a human subject's lumbar vertebra *in-vivo.* (b) The image after the application of a first order statistics filter on Fig. 3a.

2.2.2. Local Phase-Symmetry based Ridge Enhancement (PSRE) in Spinal US Images

Our proposed phase-symmetry ridge enhancement (PSRE) algorithm can be applied to surface localization of any type of bones in addition to spine. Therefore, we will use the terms "bone" and "spine" interchangeably in this section. Bone surfaces in US images are generally described by a continuous bright region. In Fig. 2.4, we show an elevation map of an US image depicting a cross-sectional view of a spine with intensity of the image along the elevational direction in the map. The elevation map is analogous to a mountain range. Edges are double line patterns representing the upward and downward slopes of each mountain. Their strength is proportional to the steepness of the slope of a mountain. Ridges, which capture highly specular surfaces including bone surfaces, have maximal strength at the medial axis on each mountain.

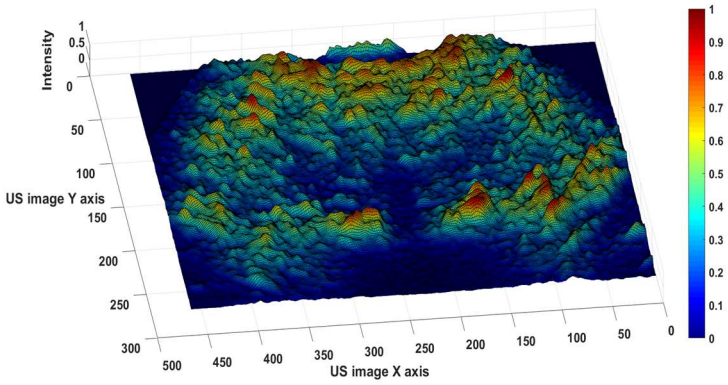

Fig. 2.4. An elevation map of an US image in which the red regions mark the high intensity regions corresponding to spine surfaces.

In our algorithm, bone surface localization is performed using phase symmetry, and it is inspired by studies presented in [40] and [41]. Phase symmetry is a contrast and illumination invariant ridge detection technique. This invariance is primarily due to the symmetry analysis done in the frequency domain [51]. That is, we use Fourier components that are maximally in phase to quantify gray level variation instead of the derivative based edge detection in the spatial domain. Extracting step features of an image (stepwise discontinuity in the intensity) involves a phase angle of 0 or 180 degrees. But, ridge feature extraction using Log-Gabor filters helps localize features at any phase angle. A Log-Gabor filter bank is used to construct the phase symmetry model. The broad bandwidth of Log-Gabor filters provides maximal spectral coverage, and the zero DC value ensures maximal spatial localization. Due to the absence of a DC component, Log-Gabor filters have to be constructed in the frequency domain. In the frequency domain, these filters are formed by the product of the Gaussian radial component that responds to the filter's spectral bandwidth and the angular component that responds to the filter's orientation, i.e.,

$$G(\omega,\varphi) = \exp\left[-\left(\frac{\ln\left|\frac{\omega}{\omega_0}\right|^2}{\ln\left|\frac{\kappa}{\omega_0}\right|^2}\right)\right] \times \exp\left[-\left(\frac{(\phi - \phi_0)^2}{2{\sigma_\varphi}^2}\right)\right] \quad (6)$$

where ω_0 is the filter's center frequency given by the reciprocal of the filter scale or $1/s$ and ϕ_0 is the orientation of the filter. In our study, we empirically set the Gaussian angular bandwidth $\sigma_\varphi = 50^\circ$. The ratio κ/ω_0 = 0.33 is obtained as a function of the speckle size's full width half maximum (FWHM) as described in [40].

The local phase of an image is obtained by convolving the US image with the even response and the odd response of the Log-Gabor filter. In the frequency domain, this convolution becomes a multiplication, and it is given in Eq. (3), with $\mathcal{F}$ denoting the respective Fourier transforms:

$$L(x,y) = \mathcal{F}^{-1}\{\mathcal{F}\{f(x,y)\} \cdot G(\omega,\phi)\} \quad (7)$$

The 2D phase symmetry measure is the difference between the even filter and odd filter responses denoted by the real part and imaginary part of the Log-Gabor filter response, respectively. When a feature with medial axis symmetry is encountered, the difference between the even and odd filter responses is relatively large resulting in the detection of a ridge in the image. This difference is defined in Eq. (4) summed over $N_s = 3$ scales, and $N_\varphi = 3$ orientations and is sufficient to enhance a smooth, continuous spine ridge.

$$PS(x,y) = \sum_{N_\varphi}\sum_{N_s} \frac{|Re\{L(x,y)\}| - |Im\{L(x,y)\}| - T}{\sqrt{(Re\{L(x,y)\})^2 + (Im\{L(x,y)\})^2} + \epsilon} \quad (8)$$

Here, ϵ is a small number that prevents division by zero and T is the shrinkage noise threshold calculated from the smallest scale filter response. T is computed to be 3 standard deviations from the mean of the Rayleigh distributed noise [52]. Inadequate selection of the scale s and orientation

ϕ_0 parameters could result in amplification of speckle noise, artifact enhancement or significant blurring of the bone feature in the US images.

We want to ensure that that features that characterize bone anatomy such as shape and orientation are accounted for in the parameter selection. The algorithm for the automatic selection of these parameters proposed in [41] is employed. The three initial filter orientations are obtained from taking the radon transform of the US image and clustering the highest means. Integration along a bone-like feature like bone, muscle, long connective tissue that isn't bone produces a higher sum than integration along non-bone like features like speckle, fat layer and, to some effect, US artifacts. The radon transform images are classified into 5 intensity levels, the thresholds of which are determined by the proximity of every pixel to the mean of each class. The fifth class represents the highest threshold of intensities. The mean of the orientations in the fifth class and two standard deviations from it are used for the initial orientations. These initial orientations are used in for selection of optimal filter scales. The scale selection procedure is generated by a ridge strength measure A_γ using the γ- normalized eigenvalue difference of the Hessian matrix such that:

$$A_\gamma = s^{0.75}\left[\left(\frac{\partial^2 L(x,y)}{\partial x^2} - \frac{\partial^2 L(x,y)}{\partial y^2}\right)^2 + 4\left(\frac{\partial^2 L(x,y)}{\partial x \partial y}\right)^2\right] \quad (9)$$

The sum of all pixels is computed for each ridge strength image generated from scale values ranging from $s = 10$ pixels through $s = 100$ pixels. The scale value corresponding to the maximum sum is used as the optimal filter scale and is shown in Eq. (10).

$$s^{(i)} = \underset{s}{\operatorname{argmax}} \sum_{x,y} A_\gamma(s,x,y) \quad (10)$$

The radon transform R_ϕ of the ridge strength image is computed for each scale such that the orientation corresponding to the maximum value of R_ϕ is extracted as shown below:

$$\phi_0^{(i)} = \underset{\phi}{\operatorname{argmax}}\, R_\phi\left[A_\gamma\left(s^{(i)}, x, y\right)\right] \qquad (11)$$

The above Log-Gabor filter parameters are used in Eq. (4) for obtaining the PSRE image (Fig. 2.5a). The PSRE image is then binarized for morphological processing (Fig. 2.5b).

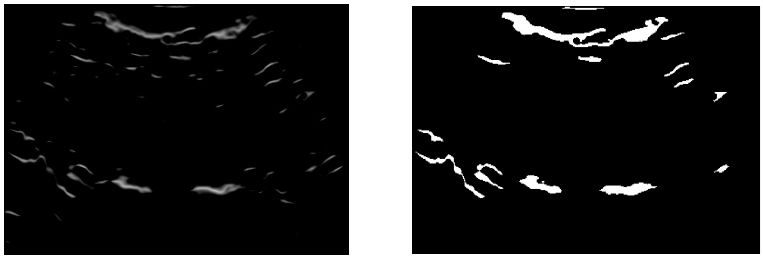

(a) (b)

Fig. 2.5. (a) Ridge enhanced image using phase symmetry (PSRE image). (b) The binarized PSRE image after morphological area opening with 14 blobs retained.

2.2.3. Feature Space Design for Spine Blob Classification

For the remaining of the paper, we will be using the term "blobs" for ridge features. The blobs can represent spine but also soft tissue that isn't bone or specular artifacts. We observe that the spinous process blobs appear to be the smallest sized blobs in the US images. A simple morphological opening operation eliminating connected components below 50 pixels is used to eliminate small blobs that can be typified as specular artifacts or the influence of scatterers. The connected component threshold of 50 pixels was chosen based on the following observation. A set of 60 spinous process blobs were randomly chosen from vertebral US images and the lowest areas were found to be roughly 100 pixels. The connected component threshold is conservatively set to be half the minimum value. From the remaining foreground pixels, which serve as the binarized PSRE

image shown in Fig. 5b, we will be extracting features for classifying these pixels into spine or non-spine blobs. The non-spine blobs are the ones corresponding to soft tissue or artifacts. We will be using two features to perform the spine surface detection of the blobs: 1) Mean Pixel Intensity and 2) Sum of Squared residuals of the Shadow region row means signal as detailed below.

2.2.3.1. Mean Pixel Intensity

The mean intensity of each blob can be obtained by multiplying the binarized PSRE image with the US image and calculating the mean of pixel intensities of each blob. Since the non-spine blob regions could result in some equal or higher mean values of the spine blob regions, a spinal region enhanced US image is necessitated. The enhancement should lead to a higher weighting for the shadow region and the blobs immediately above it. A shadow function inspired by is used in which each intensity value in the US image is taken to be the average cumulative sum of the previous intensity values in each scanline. We then take the image complement of the normalized shadow function and square it to get the Acoustic Shadowing Energy (ASE) (Eq. (12)). The $Norm_{[0,1]}$ operator indicates normalization of image intensities between zero and one.

$$ASE(x,y) = \left(1 - Norm_{[0,1]}\left\{\frac{1}{\#\ of\ rows}\sum_{i=x}^{\#\ of\ rows} f(i,y)\right\}\right)^2 \qquad (12)$$

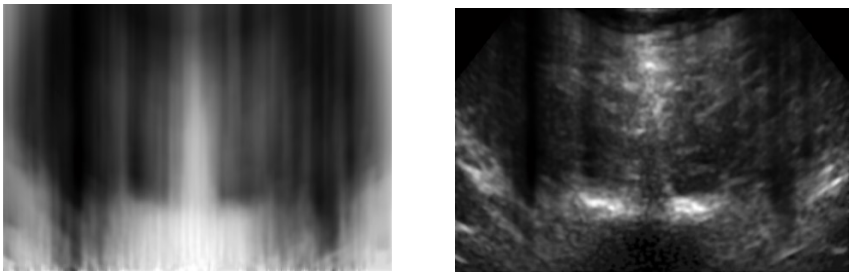

(a) (b)

Fig. 2.6. (a) The ASE image. (b) The product between the ASE image and the US image.

A non-linear contrast stretching is then performed on the product image ($f(x,y) \cdot ASE(x,y)$) shown in Fig. 2.6b over a default piecewise value of the midpoint. The transformation is quantified as:

$$\mu(x,y) = \begin{cases} 2[f(x,y) \cdot ASE(x,y)]^2 & 0 \leq ASE(x,y) \leq 0.5 \\ 1 - 2[1 - f(x,y) \cdot ASE(x,y)]^2 & 0.5 < ASE(x,y) \leq 1 \end{cases} \quad (13)$$

The mean intensity for each blob B_n is computed as:

$$MI(B_n) = \frac{1}{Area(B_n)} \sum_{(p,q) \in B_n} \mu(p,q) \quad (14)$$

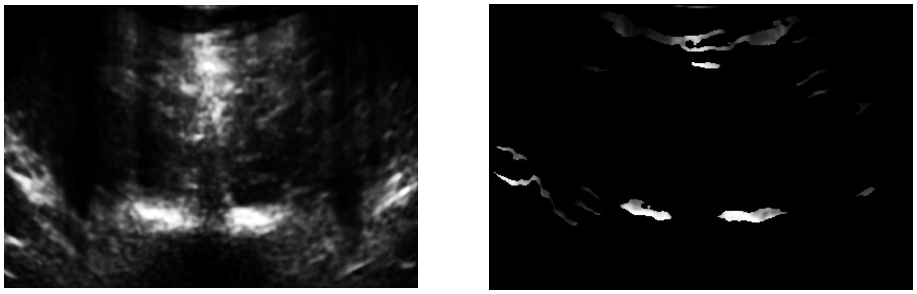

(a) (b)

Fig. 2.7. (a) The fuzzy contrast enhanced image. (b) Result after multiplication with the binarized PSRE image.

2.2.3.2. Sum of Squared Residuals of the Shadow Region Row Means (SRRM) Signal

In order to differentiate the spine blobs from the non-spine blobs, we cannot solely rely on the mean intensity of each ridge. For example, muscle can also represent elongated blobs with comparable mean intensities. For the selection of the following feature, we will use the notion of minimal penetration of the US signal through the bone as evidenced by the acoustic shadowing present underneath the bone surface. *In-vivo* spinal US images usually do not have a completely dark region to signify acoustic shadowing but normally have a non-zero signal immediately following the spine surface. We quantify this region using the signal formed by progression of row

means in the supposed shadow region beneath each blob. The scope of this region starts from the sectoral row containing the intensity weighted centroid to the bottom oriented towards the blob's medial axis as seen in Fig. 2.8.

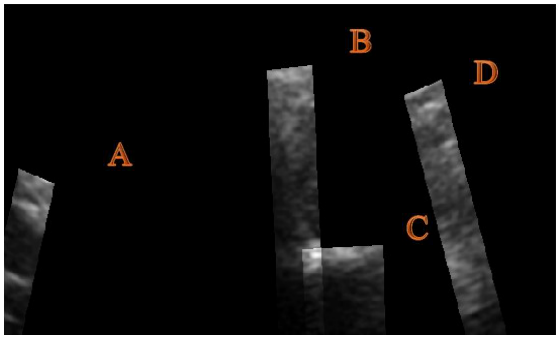

Fig. 2.8. The shadow region for 4 blobs out of 14 is shown here. B, C are spine blobs and A, D are non-spine blobs.

The upper side of the region is measured between scanlines containing the two extremes of the blob. Bresenham's line algorithm is used to fit a straight-line pixel approximation to the sides of the region [53]. For images obtained from a linear array transducer, these regions become rectangular with the last row being the bottom side. The SRRM is given by the mean intensity of each row constrained within the width of the region. The local maxima in the signal represent the presence of a high intensity, high gradient anatomical structure like bone or connective tissue. The SRRM should ideally be a monotonically decreasing function.

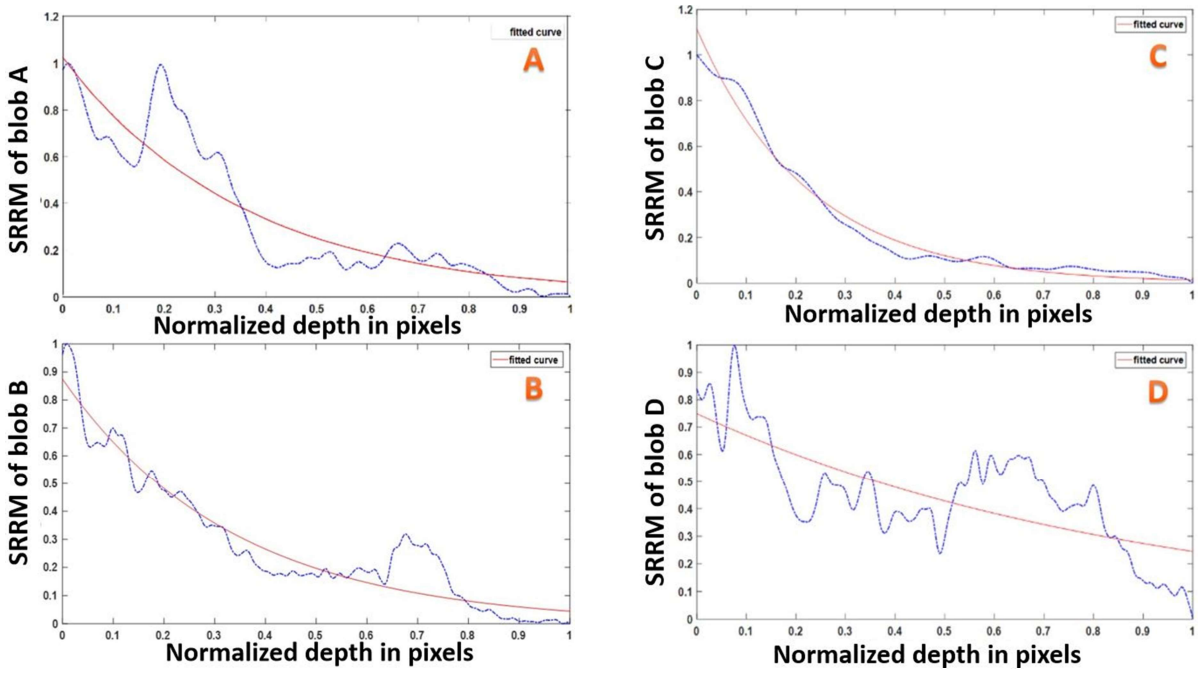

Fig. 2.9. The SRRM from the center of the blob (depth = 0) to the bottom of the US image (depth = 1) for the blobs A, B, C and D shown in Fig. 2.8.

An exponential decay function is modeled to fit the SRRM. The optimal fit for the exponential decay function is obtaining by minimizing parameters α_n and β_n for each blob B_n using the Levenberg-Marquardt algorithm:

$$SSR(B_n, \alpha_n, \beta_n) = \min_{\alpha_n, \beta_n} \sum_{i=1}^{N} (y_i - \alpha_n \cdot exp(-\beta_n x_i))^2 \qquad (15)$$

where y denotes the SRRM signal with size N and x is the depth in pixels from the intensity-weighted centroid of each blob. The minimized sum of squared residuals (SSR) for each blob will be populated in the feature space for spine surface classification. Large residual errors from the exponential fit function would indicate, at the very least, the occurrence of a high local maximum in the signal. From Fig. 2.9, we observe that the SSR values from the exponential fit function for

blobs B and C (spine blobs) is relatively small in comparison to blobs A and D (non-spine blobs), where the SSR is increased due to the presence of high local maxima. Therefore, a lower sum of these residual errors would lead to a higher likelihood of the blob corresponding to a spine surface region.

2.2.4. Classification of Spine Blobs

In the classification step, we aim to classify each blob in the binarized PSRE image into being either a spine blob or a non-spine blob. Each blob described by the two features is a data point populated in the feature space. For every binarized PSRE image given as an input to the algorithm, a test set vector in $\mathbb{R}^{n\times 2}$ is generated for the n blobs in the binarized PSRE image. A 3-nearest neighbor classification rule (3NN) is chosen to determine the points in the testing set as being a spine or non-spine blob. This is achieved by first storing all the training examples $< X_{(i)}, Y_{(i)} >$ and labeling them to be $g(X_{(i)}, Y_{(i)}) = 1$ when the data point is a spine blob or 0 otherwise. When a test point $< X_{(t)}, Y_{(t)} >$ is encountered, the blob can be classified as spine when the majority label among the 3 closest training examples is 1 and non-spine otherwise. The Euclidean distance metric is used to measure "closeness". An advantage to using the 3NN rule is that any complex decision boundary can be learned, which makes it more adaptable to noisy data. The 3NN classification shown in Fig. 2.10 clearly demarcates the spine blobs (green points).

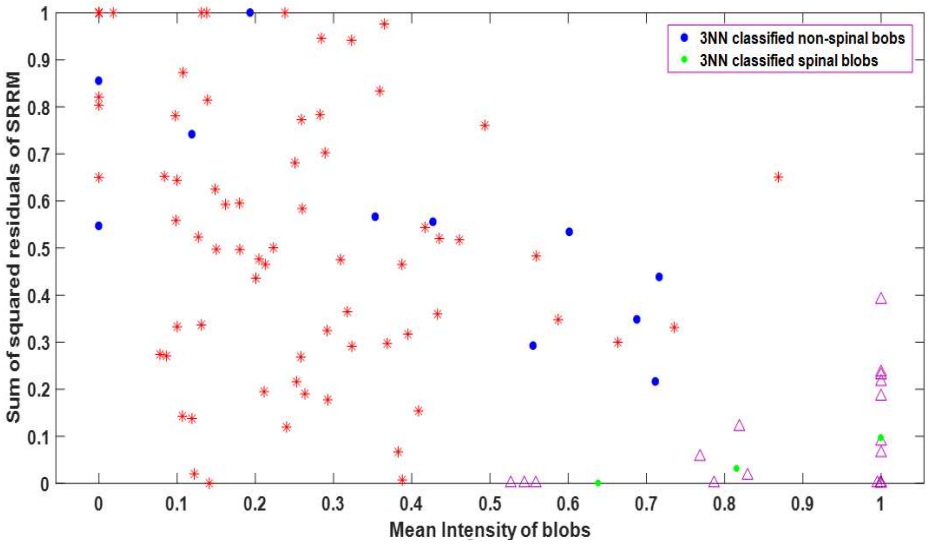

Fig. 2.10. Spine blob classfication into spine (green dots) and non-spine blobs (blue dots) with the training examples for spine blobs (purple triangles) and non-spine blobs (red stars).

In Fig. 2.11, we show the image before classification (Fig. 2.11a) and a binary image with just the spine blobs resulting from the application of the 3NN classification (Fig. 2.11b). Note that only the spine blobs are retained after the classification.

(a) (b)

Fig. 2.11. (a) Product of the PSRE image and the binary image after morphogical opening and (b) Spine blobs retained after the spinal surface recognition step.

2.2.5. Spine Surface Segmentation

According to [54], the actual bone line profile has an equi-probable likelihood of lying in between the point of highest gradient and highest intensity within the spine blob region. Each pixel in the line profile is the midpoint between the medial axis and the top boundary point of the spine blob for the respective scanline. Boundary points are obtained by the internal gradient. The medial axis line profile is obtained by applying the morphological skeleton to the spine blob and tracing the geodesic path between the blob endpoints to avoid spurious branches. An isotropic dilation using the distance transform is then applied to interpolate midpoint pixels between adjoining columns. The resulting spine surface segmentation is shown in Fig 2.12 superimposed on the US image.

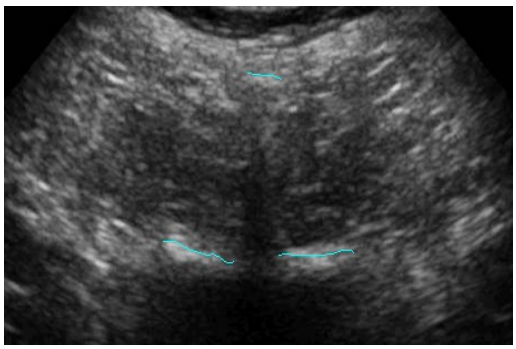

Fig. 2.12. Spine surface automatic segmentation given by the line profile (in cyan) overlayed on the original US image.

2.2.6. Experimental Validation

In-vivo B-mode images were acquired from the lumbar and thoracic regions of 17 healthy human subjects with BMI ranging from 19.5 (normal) to 27.9 (overweight). Data were acquired using a Sonix RP diagnostic ultrasound system (Analogic Medical Corp., Richmond, BC, Canada) that

uses a convex array transducer with bandwidth between 2-5 MHz. For the reported results, all acquisitions were obtained with the center frequency set to either 3.3 MHz or 5 MHz.

The US scans were performed by first seating the subject in an upright position and then, either the transverse or paramedian plane approach was taken. The transverse scan is more advantageous in that it enables a more comprehensive 2D visualization of a vertebral slice showing the laminae, spinous process, articular process, transverse process, LF and the interspaces in between. For the paramedian scanning approach, the articular processes, laminae and the interspaces spread across three vertebrae.

2.2.7. Statistical Evaluation

A set of 108 US B-mode images (size: 349×603 pixels; depth: 70 mm) were randomly selected from 30 cine-loops to perform statistical evaluation of the spine surface detection. An experienced radiologist manually marked the spine and non-spine blobs in the binarized PSRE images corresponding to the visible portions of the vertebra in the B-mode images. These regions are dorsal to the vertebral foramen in spinal US and include spinous process, laminae, articular processes and transverse processes. The blobs from each resulting binarized PSRE image were used as the test set for classification.

For the training set in the spine blob classification, we obtained US B-mode images from scanning the tibia bone of two sheep, radial bone of one healthy individual and the thoracic and lumbar vertebrae of two healthy individuals *in-vivo*. The different types of bones were chosen to encapsulate bone surfaces of various intensity profiles and various shadow regions and

histograms. These images were fisrt enhanced by the PSRE algorithm and the blobs from the binary image were manually marked as bone or non-bone by the radiologist. The training examples were composed of 91 randomly selected blobs from 70 PSRE images. For evaluating the accuracy of the spine surface segmentation, the radiologist manually delineated the surface of the laminae on the US B-mode images.

2.3. RESULTS

2.3.1. In vivo results

Fig. 2.13 shows examples of spine surface automatic segmentation superimposed on a paramedian plane US image (top) and a transverse plane US image (bottom) obtained from a human subject *in vivo*. The paramedian plane US image shows the segmented laminae from lumbar vertebral levels L4, L5 and the Sacrum. The transverse plane US image from the L1-L2 intervertebral level shows the segmented articular processes, transverse processes and the LF. Note also that the skin to LF depth can be clearly visualized in the bottom portion of the transverse image.

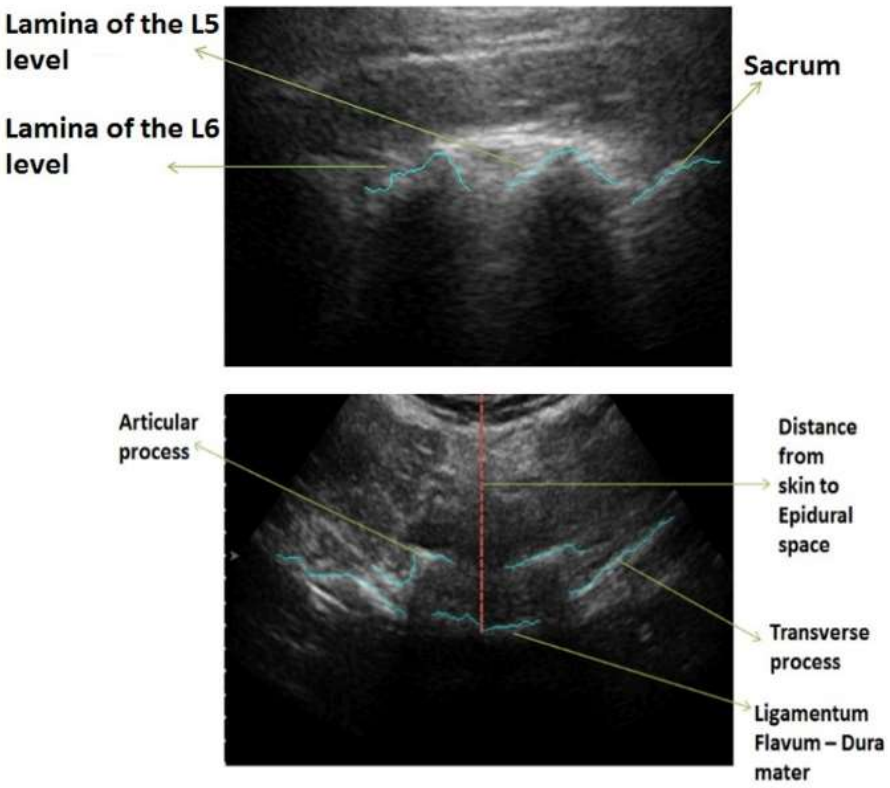

Fig. 2.13. Spine surface automatic segmentation on a 2D US image slice of a human subject's lumbar vertebrae *in-vivo* obtained in the Paramedian plane (top) and transverse plane (bottom).

Fig. 2.14 shows the qualitative performance of the proposed algorithm in three different US images across the lumbar and thoracic spines of three human subjects in-*vivo.* Fig. 2.15 shows the lumbar spines of two human subjects in-*vivo* with the detected LF (highlighted in green).

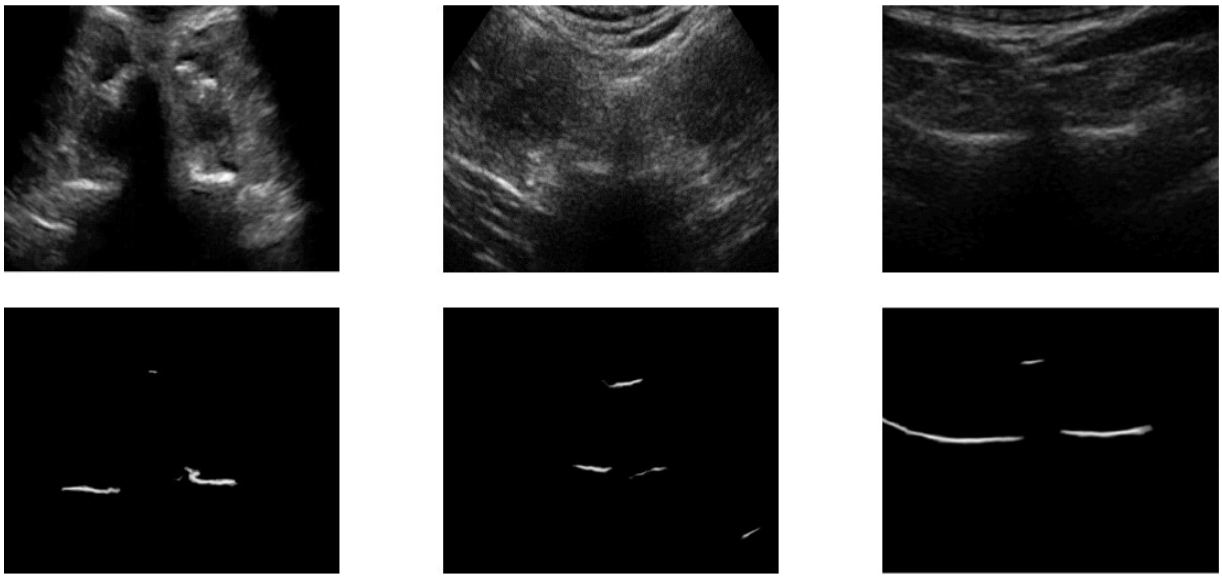

Fig. 2.14. Three original US images of human subjects *in vivo* obtained in the transverse plan (top) and the corresponding images after detection of spine surface regions (bottom). First column shows lumbar spine L3 level from human subject with BMI = 24.1. Second column shows lumbar spine L1 level from human subject of BMI = 27.5. Third column shows thoracic spine T5 level from human subject with BMI = 22.3.

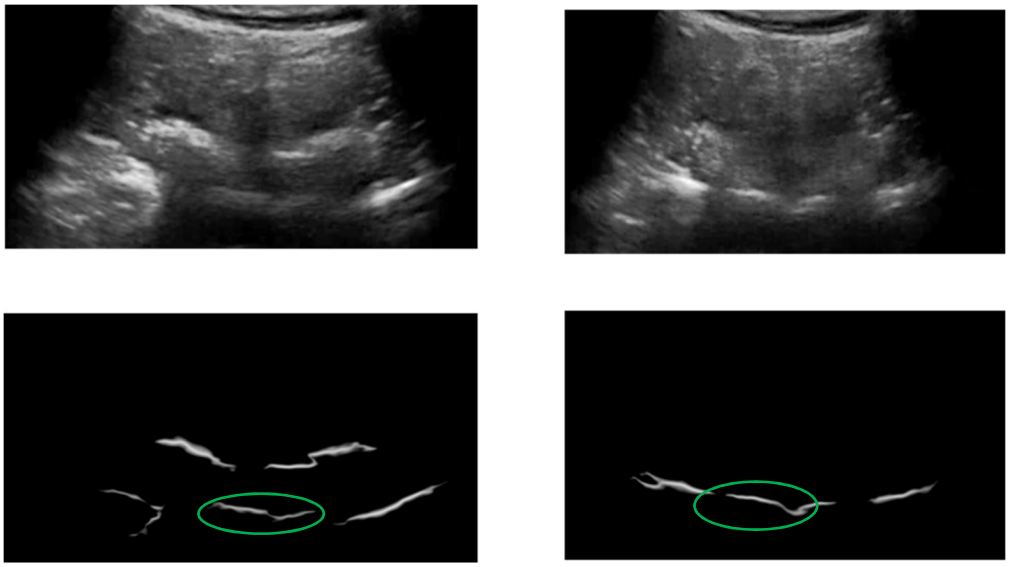

Fig. 2.15. Two original US images of human subjects *in vivo* obtained in the transverse plan (top) and the corresponding images after detection of spine surface regions (bottom). First column shows lumbar spine L1-L2 interspace level from human subject with BMI = 24.1. Second column shows lumbar spine L2-L3 level interspace level. The LF is highlighted in green.

2.3.2. Statistical Evaluation Results

As previously mentioned, an experienced radiologist manually marked the spine and non-spine blobs in the binarized PSRE images. For the purpose of illustration, Fig. 2.16 shows our proposed spine surface segmentation profile (magenta line) overlaid on the radiologist's manual segmentation (yellow dotted line). Note the remarkable agreement between the automatic segmentation results and the radiologist findings.

We validated the spine surface detection by assessing the performance of the 1) Spine blob classification and the 2) Spine surface segmentation.

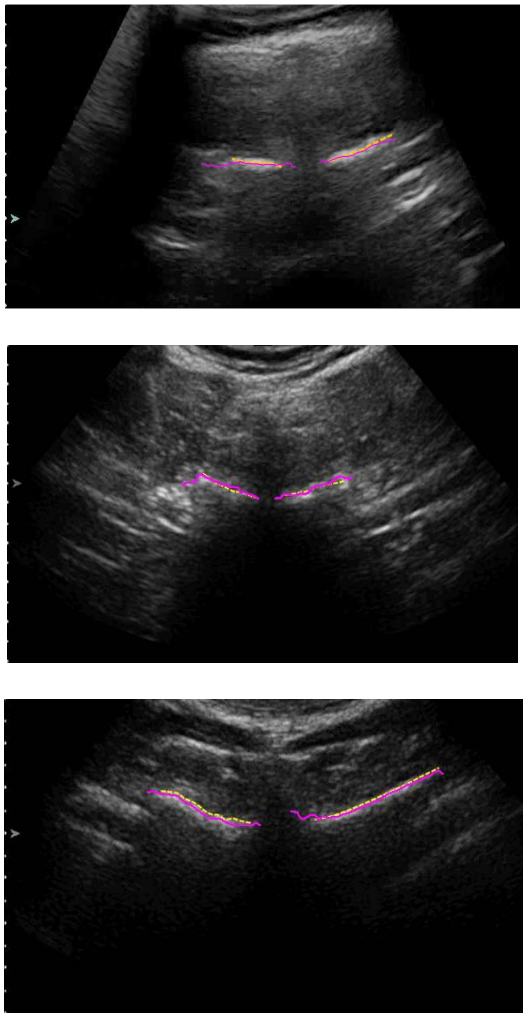

Fig. 2.16. Radiologist's manual segmentation of the laminae line profiles (dotted yellow) overlaid on the automatic segmentation (magenta).

2.3.2.1 Performance analysis of the spine blob classification

The discrimination power of the 3NN classifier in classifying spine blobs is assessed using the Geometric mean (G- mean) and Matthews Correlation Coefficient (MCC) performance measures derived from the confusion matrix given in Table 2.1.

Class	*Actual Values*	
Predicted Values	Spine Blobs	Non-Spine Blobs
Spine Blobs	$T_P = 282$	$F_P = 151$
Non-Spine Blobs	$F_N = 9$	$T_N = 2548$

Table 2.1. Confusion matrix for evaluating MCC and G-mean measures.

These measures, defined below, are chosen based on their immunity to imbalanced class sizes:

$$MCC = \frac{T_P T_N - F_P F_N}{\sqrt{(T_P+F_N)(T_P+F_P)(T_N+F_P)(T_N+F_N)}} \quad (16)$$

$$G-mean = \sqrt{\left(\frac{T_P}{T_P+F_N}\right)\left(\frac{T_N}{T_N+F_P}\right)} \quad (17)$$

The MCC value ranges from -1(never classifies correctly) to +1 (perfect classification) and the G-mean values range from 0 to 1(perfect classification). An MCC value of 0 indicates random classification. The proposed algorithm achieves an MCC of 0.77 and a geometric mean of 0.96.

2.3.2.2. Performance analysis of the Spine surface segmentation

The line profiles from the automatic segmentation corresponding to the laminae are evaluated against the radiologist's manual delineation of the laminae surfaces. The error metric used for our performance analysis is the mean absolute error, which is given by:

$$MAE = \frac{PH}{NS}\sum_{c=1}^{NS}|A(c) - M(c)| \quad (18)$$

where NS is the length of the lamina line profile in scanlines, PH is the pixel height in mm, A and M are the automatic and manual segmentation row value, respectively. The MAE (as shown in

Fig. 2.17) is computed between the intersecting pixels of both the manual and automatic segmentations with respect to each scanline. The mean value of the mean absolute errors is 0.26 mm and the 90^{th} percentile of mean absolute errors is 0.44 mm with a maximum possible absolute error of 2.01 mm. This is comparable to the mean absolute errors as reported in long bones by Berton et al. [0.38 mm between centroids of the spinous process] and Hacihaliloglu et al. [0.31 mm], Kowal et al. [0.42 mm for cadavers], Foroughi *et al.* [0.3 mm for cadavers], Daanen *et al.* [0.45 mm for patients and 0.27 mm for cadavers], Jia *et al.* [0.2 mm] [49, 40, 33, 35, 55, 56].

Fig. 2.18 shows the percentage of automatic segmentation (in length) with respect to the expert segmented lamina length. From this graph, we note that the number of false positives far exceeds the number of false negatives. This is also visible from the false positive and false negative rate boxplots shown Fig. 2.19. These rates correspond to the non-intersecting pixels of the automatic and manual segmentations. The mean false positive rate, which computes the proportion of incorrectly identified spine pixels, is 4.65 ± 4.94%. We encountered false negative pixels in 6 US B-mode images with a maximum false negative rate of 7.14%.

In terms of computational costs, the mean runtime of the algorithm was found to be equal to 7.3 s, when the algorithm is run on MATLAB (Mathworks, Natick, MA) in an Intel Core i3 2.3GHz CPU with 4GB RAM. We observed a 16% decrease in runtime for images obtained from a linear array transducer.

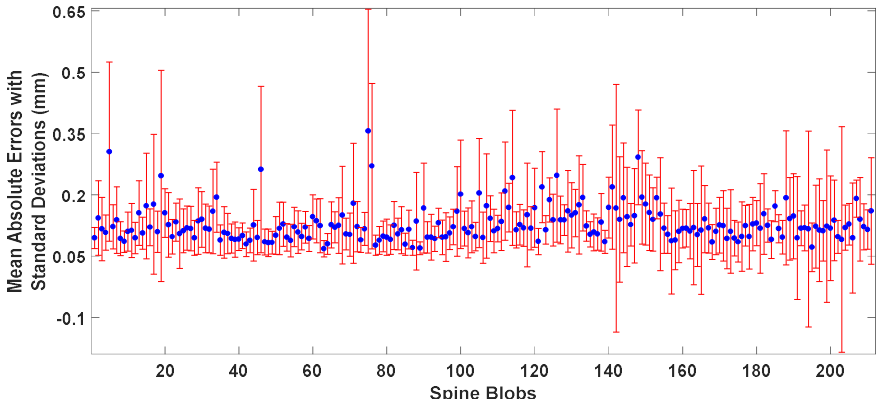

Fig. 2.17. Mean absolute error between the automatic and manual segmentation for the 216 laminae surfaces.

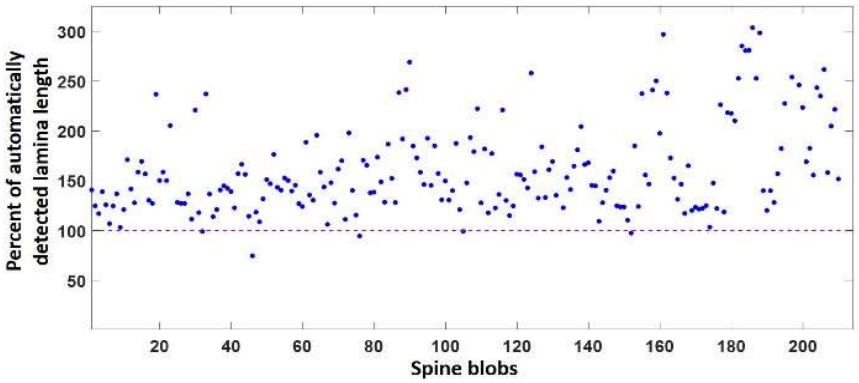

Fig. 2.18. Percent of the detected lamina length value (defined as: automatically identified lamina length/expert segmented lamina length) for the 216 laminae surfaces.

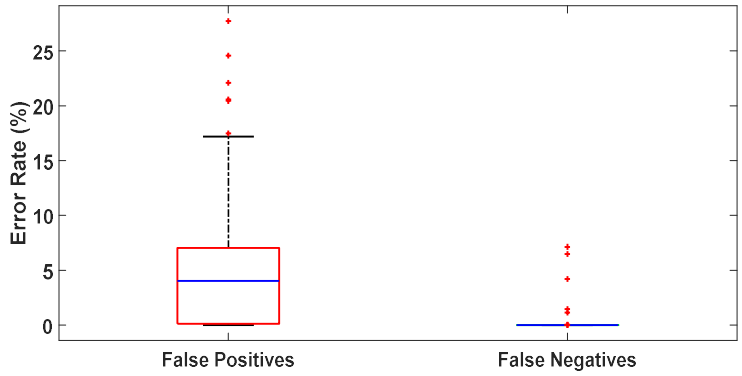

Fig. 2.19. The false positive and negative rate boxplots for the automatic spine surface segmentation.

2.4. DISCUSSION

We have presented a new method to detect spine surfaces in US images. This method was tested on human subjects *in vivo* and validated against the manual measurements of an expert radiologist. A statistical analysis of the proposed method suggests its potentials as a new non-invasive tool to automatically detect spine surfaces in US images both for the transverse and the paramedian approaches. While the performance of our spine surface detection method was found to be statistically comparable to some of the proposed methods for long bones, to our knowledge, no other spine surface detection algorithm with comparable performance is retrievable in the literature. It should be noted that highly accurate detection of spine surfaces in US images is, in general, a very challenging task due to the geometry of the spine and the presence of multiple artifacts in the US images.

Our proposed technique relies on the robustness of the PSRE algorithm in detecting low-level features like ridges in constrained areas of the B-mode image. The PSRE algorithm depends on

orientations extracted from the radon transform for detection of line features that describe the bone surface. These orientations are used to produce ridge strength images from which the three optimal orientations and scales are obtained. The Log-Gabor filters that use these parameters are, in turn, aggregated in the phase-symmetry equation. For each blob obtained as a result, we calculate the mean pixel intensity feature from the fuzzy contrast enhanced image. The sum of squared residuals of the SRRM signal feature provides a measure for the magnitude of posterior acoustic shadowing underneath each blob. The classified blobs are segmented in concordance with the most probable location of the bone surface. Our proposed technique successfully captures line profiles of the laminae, LF, spinous, transverse and articular processes.

A lot of the existing literatures on bone surface segmentation employ cadaveric specimens and phantoms for experiments where the acoustic shadowing area has predominantly zero intensity. Our proposed algorithm should work for any perceivable shadowing. Since the scale and orientation parameter estimation stems from the line feature detection using the radon transform, elongated bone regions can also be detected. The use of multiple orientations for the Log-Gabor filter accounts for any existing curvature of these bone regions. Filtering for optimal orientations enables spine detection even when the transducer is not aligned with the midline in the transverse view as seen in Fig 2.16.

In its present form, the proposed spine surface detection method has some limitations that should be addressed in the future. The acquisition using the curvilinear transducer limits the view to relatively perceivable hyperechoic line profiles corresponding to the top surfaces of the laminae, spinous process, articular and transverse processes. This is due to a viewpoint obtained only at a

90º angle of insonication. So, the vertebral surfaces that lie nearly parallel to the direction of propagation of the ultrasonic beam cannot be interpreted and thereby delineated clearly. This results in large intensity discontinuities in the hyperechoic line profile. In the absence of fractures or abnormalities, this line profile should extend continuously along the vertebra, but it is not picked up by the PSRE algorithm. For example, Fig. 2.12 shows a large acoustic shadow masking most of the spinous process's surface with the exception of the upper surface that has been automatically segmented. Without knowledge of the entire surface of the spinous process, catheter placement could be misguided during the epidural or spinal. Note, however, that this is a cause for concern only when the transducer is placed above the spinous process as opposed to the interspinous space where epidural administration occurs. In the future, this issue could be curbed by acquiring multiple spinal US images in the transverse plane at oblique angles of insonication in addition to the US image obtained at 90º. These images can then be spatially compounded to obtain a more contiguous hyperechoic line profile that represents the entire spine surface dorsal to the vertebral foramen. Additionally, statistical shape priors as proposed in [43, 45] from other modalities could be incorporated during the epidural to enforce vertebral boundary constraints. The extent of some vertebral regions, the spinous process in particular, can be crudely estimated by detecting its acoustic shadow formed underneath as explained in [49].

The false positive rate errors in the spine surface segmentation may be attributed to limited elevational resolution. For example, the PSRE algorithm may pick up a ridge corresponding to the inferior articular process that is not present in the actual slice being imaged due to the intensity invariance of the PSRE algorithm. However, the radiologist may not perceive this because the region is construed as being less hyperechoic than the preceding or succeeding slices. This problem

may be exacerbated when imaging more closely packed thoracic vertebrae, where more than one vertebra can be detected by the transducer in a given plane. The slice thickness artifact may be minimized by increasing the operating frequency, acoustic power or with the use of 2D arrays. The fuzzy contrast enhanced image (shown in Fig. 2.7a) that boosts the intensity of the hyperechoic pixels could be used as the input to the PSRE algorithm so that there is little influence of the vertebral column from slices within the vicinity of the one being imaged. However, this may have the effect of enhancing hyperechoic regions corresponding to extraneous specular artifacts and connective tissue/muscle emulating the bone line profile. Note that the fuzzy contrast enhanced image could also be used to boost the low intensity profile of the LF, which may not be appropriately captured by the PSRE algorithm. In such cases, the ASE power can also be modified (we suggest a range of 1-3) at the expense of masking vertebral regions lateral to LF.

The false positives and negatives in the spine blob classification can also arise from the fact that we are only using hyperechogenicity and acoustic shadowing to model spine blob detection. Additional features like statistical shape priors could be incorporated into the feature space. However, the fact that the algorithm does not require a priori shape information is a strong advantage, which makes it suitable to virtually detect any bone surface in an US image. Furthermore, by adding more features we run the risk of overfitting the classifier by making it too complex when adapting it to different vertebral models. For a larger depth setting covering areas beyond the LF, we are able to visualize the posterior longitudinal ligament/vertebral body (PLL) with the hypoechogenic dural sac located between the PLL and LF. For such cases, we cropped the US images beyond the LF since the sum of squared residuals of the SRRM feature in the spine blob classification is constrained to work for blobs that have acoustic shadowing in the US image

and can fail when there are hyperechogenic structures below the blob. From the vertebral slice geometry, we observe that the LF and PLL are the blobs intersecting the midline in the interspinous regions. So, a midline detection approach as mentioned in [48] can be applied after the PSRE algorithm to facilitate LF segmentation without cropping the US image.

The PSRE algorithm is constrained by the empirical setting of the angular bandwidth σ_φ parameter. We could resort to the data-driven approach for estimating σ_φ using Kurtosis of radon transform [41]. There are some cases where the ridge feature strength can be improved upon by adjusting σ_φ to affect the sharpness or smoothness. But this would increase the computation time due to the radon transform calculated for a large set of possible angles and would not deter the phase-based localization of the spine surface significantly. The relatively high runtime of the proposed method can be alleviated by porting the MATLAB implementation to a GPU. Amir-Khalili *et al*. has shown the feasibility of near real-time bone surface extraction on a GPU using local phase features [57]. Finally, the availability of data from a larger number of human subjects may further help improving the performance of the classifier.

2.5. CONCLUSION

This chapter aims to provide a fully automated spine segmentation technique for US images. The *in vivo* experimental results demonstrate that spine blobs are detected and that the spine surface is segmented with high accuracy. The intensity invariance of the PSRE algorithm results in capturing of the full extent of the laminae, LF, transverse and articular processes and the tip of the spinous process. The ridge detection using the PSRE algorithm and subsequent 3NN classification allow spine surface segmentation in US images acquired in both the transverse and paramedian planes.

CHAPTER 3

AUTOMATED 3D RENDERING OF THE SPINE AND BONE REGENERATION IN FREEHAND ULTRASOUND IMAGING

3.1 3D RENDERING OF THE VERTEBRAE

Intraoperative image guidance is of paramount importance when performing surgical procedures on the spine. One of these being spinal fusion surgery where bone is grafted on the sides of the vertebrae and pedicle screws are used as anchor points. These are highly dependent on x-ray-based fluoroscopy which is the preferred real-time imaging modality for spine surgeons. However, there is the increased risk of ionizing radiation to the surgeon, patient and operating room staff. Visualization of such radiographic images is also restricted to 2D viewpoints which can have inherent limitations.

The majority of the work retrievable in the literature on US bone imaging refers to the use of low-frequency US methods to assess bone density or detect bone abnormalities [58-59]. Neck and back pain attributed to the cervical spine are common ailments experienced by astronauts and military aviators. Recently ultrasound has been proposed in measuring the anatomy and height of cervical intervertebral disc space in order to identify c-spine disorders in extreme acceleration environments [60]. US has also been used as a screening tool for administering spinal injections [18].

Ultrasound imaging is touted as a portable modality capable of provide real time imaging and being cost-effective. It is also known for its safety, superior spatial and temporal resolutions and

portability. This makes it attractive for military applications and emergency medicine. It is well suited for use in settings where traditional radiography and MRI may not be immediately available such as in rural areas, military and humanitarian medicine applications, and in the prehospital setting. However the three-dimensional (3D) capabilities have been unexplored. A large part of this is because ultrasound is plagued with artifacts and is heavily operator dependent. These make image interpretation quite difficult. Spinal ultrasound imaging shows little penetration beyond the bone surface.

Few studies have been reported to date that investigate the use of 3D US imaging techniques for bone applications [62], and none of these studies focuses on spine applications. The studies retrievable in the literature that deal with US imaging of spines typically refer to conventional 2D sonographic applications in a clinical setting, which provide only partial views of vertebral abnormalities and a somewhat qualitative assessment of soft tissue changes [29-30]. Scoliosis assessment has been addressed using 3D freehand ultrasound imaging for measurement of spinal curvature [62, 63]. Visualization of a projection of the spinous processes is sufficient in these cases. However, a 3D structure of the vertebrae that included structural information containing the spinous process, articular processes, laminae and ligamentum flavum has not been presented. To the best of our knowledge, the preliminary data reported in this chapter represent the first spinal 3D US images produced to date (with exception to neo-natal images). This paucity of spinal US imaging data may be explained by the significant challenges typically encountered in spinal US imaging investigations, which are in part due to the peculiar geometry of the spinal tissue but mostly due to the inherently low SNR.

Some have proposed to minimize radiation risk by preoperatively planning the surgery using CT and using this in conjunction with US image slices during the surgery. Fitchinger et al. proposed tracking the 2D US snapshots and registering them to the pre-op CT as part of an integrated computer assisted system framework [64]. 3D visualization of spine would facilitate the intraoperative administration of epidural anesthesia by providing complete visualization not only of the spine but also of epidural needles in all possible viewpoints.

This chapter deals with the 3D reconstruction of the previously obtained enhanced slices containing the spinal ridges. Owing to a third dimension containing structural information along the elevational direction, there is more to be seen. There will also be an extensive validation scheme with regard to the accuracy of the 3D rendering. The performance of the automated reconstruction will be assessed against a expert delineated posterior vertebral surface. We will also show the feasibility of registering the ultrasound slices to CT preoperative CT.

To generate spine 3D US images in vivo with high image quality, robust image-enhancement and acquisition techniques must be provided. The image-enhancement technique of choice should be able to automatically and accurately segment a bone surface in each US image used for the 3D reconstruction. In the past years, a number of segmentation ad image-enhancement methods have been proposed to detect bone surfaces in ultrasonic images [32-42]. After a number of preliminary tests and simulations, our conclusion is that none of these methods alone would be able to provide accurate and reliable spine segmentation results due to the peculiar geometry and the very challenging noise conditions encountered when working with spine US images. Thus, we propose to develop a new image-enhancement and segmentation technique for

spine applications. The proposed method combines shadow, image intensity, image phase information and feature classification to accurately identify the spine surface in noisy US images.

3.1.1. 3D surface rendering of the posterior spine using 2D optimized local phase symmetry features and classification.

Automatic extraction of the vertebrae from 3D US images in-vivo necessitates a robust enhancement of the underlying bone surface in each axial slice. As mentioned in the previous chapter, intensity-based methods do not perform well under varying contrast and noise conditions posed by US images. Discernible ridge-like features are first extracted using the local phase-symmetry model. This is followed by classification of the spine ridges that involve feature vectors incorporating shadowing and bone intensity. This step removes undesirable artifacts and surrounding tissue structures. The algorithm details for extracting the 2D spine is provided in Chapter 2. Each phase-enhanced 2D axial slice is stacked together in forming the 3D volume. The surface rendering is then performed using the open-source ImageVis3D framework. The volume is then scaled according to dimensions concomitant with human spine models.

3.1.2. US-CT registration of 2D point sets

Ultrasound image guidance is becoming increasingly prevalent in surgery scenario due to its real-time accessibility and non-ionizing radiation. However, the modality's use in orthopedic applications has inherent limitations. A major one being the influence of acoustic shadowing under the bone which limits visibility in the regions anterior to the vertebral foramen (or the posterior arch). A question of the surgeon's/physician's interpretation of the spine after our proposed spine surface segmentation scheme can also be raised since it does not provide the

complete picture of the 2D vertebral slice. The real-time capability of ultrasound for imaging the spine surface and the quantification of mechanical behavior of soft tissue surrounding it can be complemented by the use of alternate modalities like CT or MRI for missing structural information. This calls for an accurate alignment protocol of ultrasound images during surgical intervention with pre-operative CT datasets. Our proposed image registration technique aligns the spine surfaces captured in ultrasound images to the corresponding vertebral anatomy in the CT slices. It also has implications in using the elastographic characterization of the spine/soft tissue interface with modalities like CT and MRI.

We have used a point set registration scheme in aligning the vertebral anatomies of the US and CT datasets. The US spine surface point set is first obtained by the spine surface segmentation method. Sequentially, the method incorporates phase-symmetry based ridge detection, classification of the ridges into spine and non-spine regions and spine surface segmentation by morphological skeletonization. The CT point set is obtained by segmenting the vertebra from the respective CT slice in the axial plane using a marker-controlled watershed algorithm. In order to further represent the spine surface as seen in ultrasound, the top half of the vertebra alone is retained in the CT point set. The respective coordinates from the segmented vertebra in CT and US are the point sets being registered. The registration algorithm works by representing each point in the US point set as a Gaussian mixture model (GMM) centroid which, as a collective, is iteratively fitted to the CT point set by using EM optimization to maximize the likelihood function. This is inspired by the seminal work done on point set registration [65]. We set the point set alignment to be an affine transformation that incorporates scaling and skewing of the US point set to the CT point set in addition to a simple rigid transformation of rotation and

translation. Fig 3.1a shows an ultrasound slice of the posterior arch of intact lumbar vertebra and the detected spine region after our proposed US spine segmentation algorithm in Fig 3.1b. The indices of the segmented region serve as the US point set of GMM centroids. Fig 14a shows the US point set in blue and CT point set in red before registration and Fig 3.2b shows the registered point sets. Fig 3.3 shows the transformation applied to the spine surface detected from the US image overlayed on the CT slice. Fig 3.4, 3.5 and 3.6 show another example for a more complex geometry of the spine that includes the spinous process and laminae. Notice how the point set alignment works even when the US and CT images are of different sizes or scale. The registration technique is quite robust to noise when compared to a lot of intensity-based registration techniques which incorporate intensities of the entire image or feature as opposed to our technique that factors in geometry alone. A popular point set registration algorithm called the Iterative closest point (ICP) method involves a least square fitting of the closest points between point sets. ICP issues hard correspondences between points as opposed to our technique that issues soft correspondences between points using probabilities. Since the US elastogram to sonogram registration is a simple translation operation, the affine transformation recovered from the US-CT point set registration can be applied to the strain patterns in order to align them with the CT data to interpret the mechanical behavior of soft tissues surrounding the vertebra.

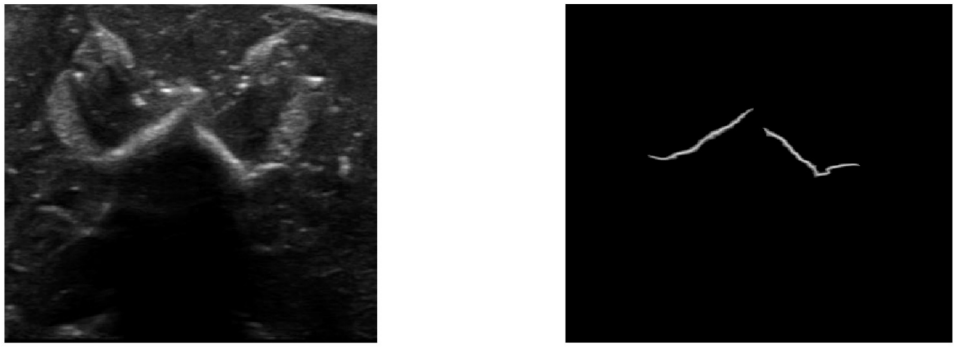

Fig 3.1. a) Ultrasound image of the intact rabbit's posterior arch. b) Detection of the vertebral surface from our proposed spine surface segmentation algorithm.

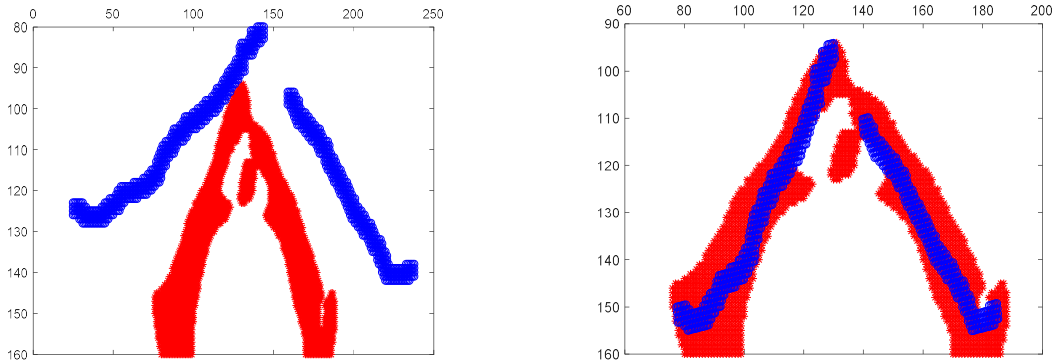

Fig 3.2. a) Ultrasound image of the intact rabbit's posterior arch. b) Detection of the vertebral surface from our proposed spine surface segmentation algorithm.

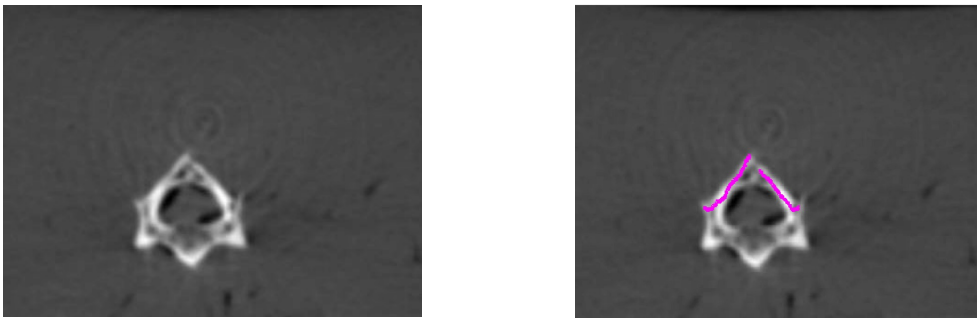

Fig 3.3. a) CT slice of the intact rabbit's posterior arch. b) The registered US veterbral surface in magenta overlayed on the correspoding CT vertebra.

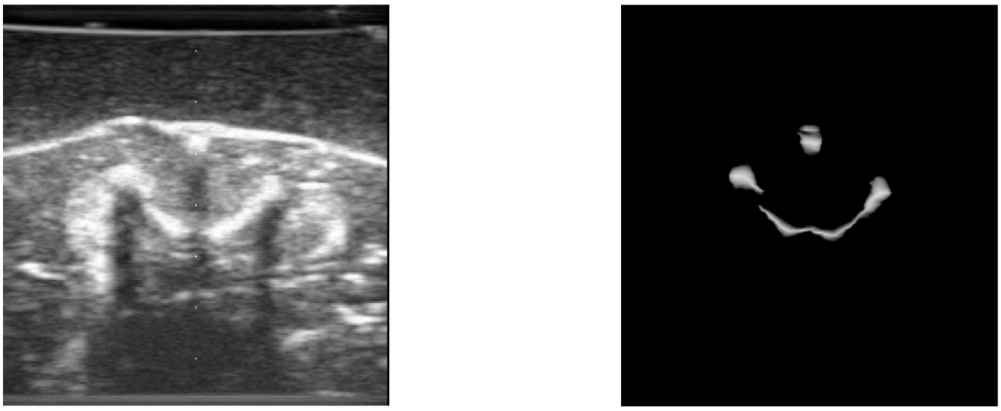

Fig 3.4. a) Ultrasound image of the intact rabbit's spine surface showing the laminae and spinous process. b) Detection of the vertebral surface from our proposed spine surface segmentation algorithm.

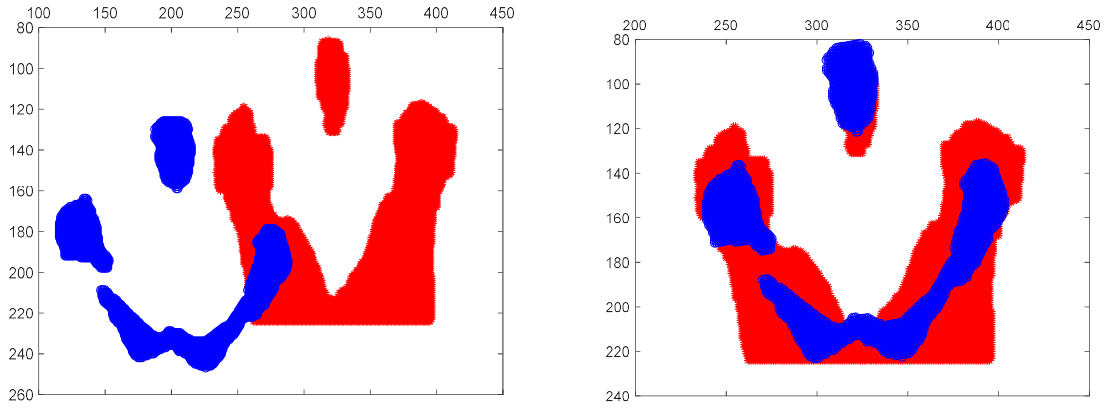

Fig 3.5. a) Ultrasound image of the intact rabbit's spine surface showing the laminae and spinous process. b) Detection of the vertebral surface from our proposed spine surface segmentation algorithm.

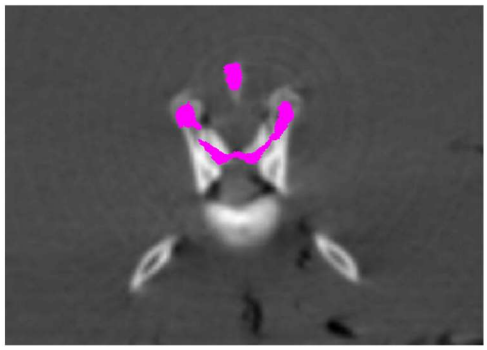

Fig 3.6. a) The registered US veterbra in magenta overlayed on the corresponding CT vertebra. The point set registration algorithm becomes incredibly more difficult with more complex geometry or ex-vivo fracture cases that could potentially misalign transformation from a particular segment.

3.1.3. Statistical analysis

The accuracy of the 3D renditions is assessed by comparing the automatic segmentation with the expert delineated manual segmentation of the posterior vertebral surface. In order to obtain the automatic segmentation, the enhanced spine ridges are transformed to a pixel-thick line profile details of which are given in Chapter 2. Each surface of a single vertebra is manually delineated by a medical expert in the form of digitized contour points for each axial slice. Surfaces that are parallel or near-parallel to the ultrasound beam are not "seen" by the transducer within the transverse view of the vertebra. Such adjoining regions including the lateral sides of the SP and, in some cases, the AP are not delineated. The distance between the manual and automatic delineations of the surface are obtained using the Hausdorff distance which given as follows:

$$d(A,M) = \max_{xA} \left\{ \min_{xM} \|b_{xA} - b_{xM}\| \right\} \qquad (19)$$

Voxels that are falsely identified by the automatic segmentation are considered false positive voxels. Voxels in the manual delineation that are not picked up by the automatic segmentation are considered false negative voxels. The Dice coefficient provides an estimate of the misidentified voxels:

$$DSC = \frac{2TP}{2TP + FP + FN} \qquad (20)$$

3.1.4. Statistical analysis

3.1.4.1. Qualitative performance assessment of the 3D spine surface rendering

The 3D rendering of a rabbit's lumbar vertebrae with one sacral level is shown in Fig 3.7. Although the SP is not quite evident the symmetrical articular processes are seen along with the interspaces. False positive blobs can also be seen on the sides but they are mostly concentrated away from the vertebrae. Fig 3.8 shows the in-vivo results of two human subjects with BMI 21.8

and 22.6 respectively. The thoracic vertebrae in Fig 3.8a with 4 levels is clearly visible. Fig 3.8b shows the transitional region between thoracic and lumbar vertebrae with 4 levels. Intact cervical vertebrae of a human subject with BMI 28.1 is reconstructed in Fig 3.9.

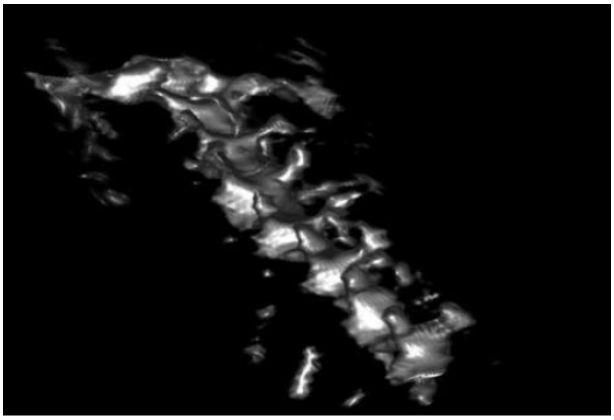

Fig 3.7. Ex-vivo sample representing an intact lumbosacral vertebra (L6-S1) of a rabbit ex-vivo

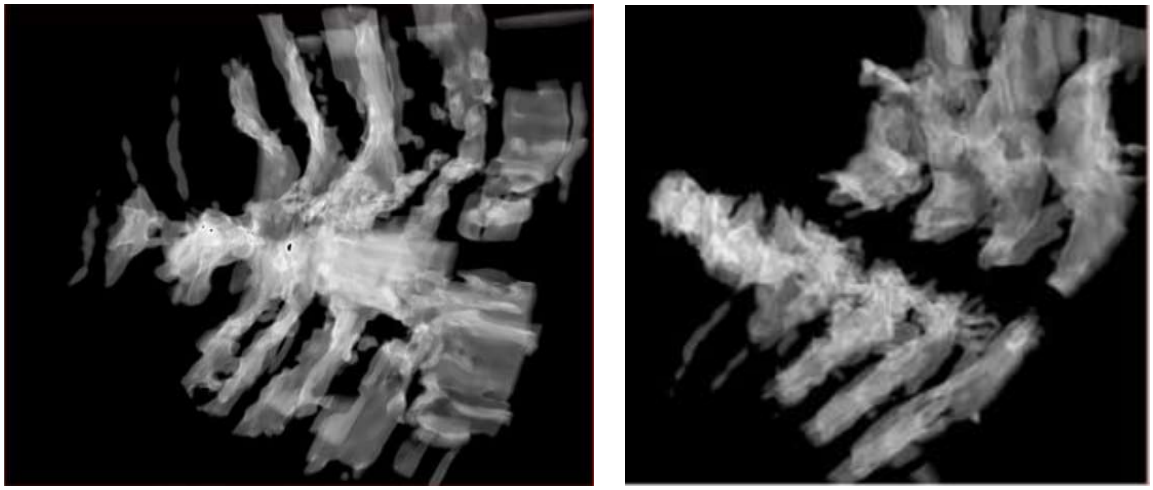

(a) (b)

Fig 3.8. In-vivo 3D rendering of the vertebrae. A) Intact thoracic vertebrae of subject 1 with BMI 21.8. b) Intact thoracolumbar region of subject 2 with BMI 22.6.

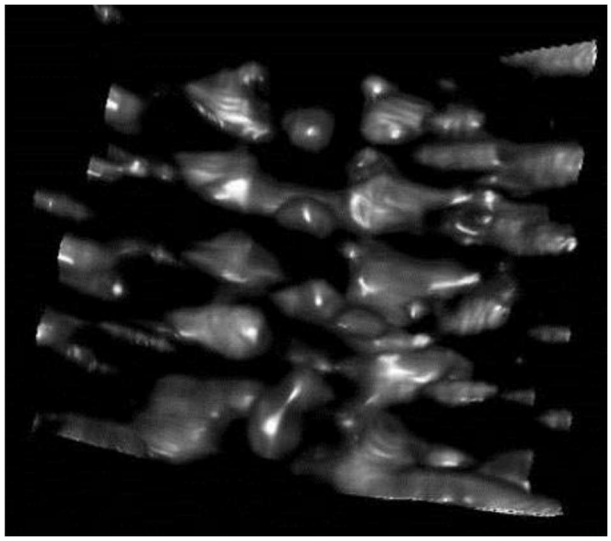

Fig 3.9. Intact cervical vertebrae of a human in-vivo with BMI 28.1.

3.1.4.2. Quantitative performance assessment of the 3D spine surface rendering

Table 3.1 shows the Hausdorff distance obtained for 10 volumes:

Vertebra volume	**Hausdorff Distance (mm)**	**Dice similarity score**
Subject 1	0.38 ± 0.97	0.79
Subject 2	0.41 ± 1.33	0.842
Subject 3	0.23 ± 0.71	0.864
Subject 4	0.28 ± 0.68	0.924
Subject 5	0.24 ± 0.85	0.96
Subject 6	0.36 ± 1.01	0.81
Subject 7	0.39 ± 1.6	0.931
Subject 8	0.34 ± 0.55	0.866
Subject 9	0.35 ± 1.44	0.774
Subject 10	0.39 ± 1.77	0.878

Table 3.1. Hausdorff distance and dice coefficient for a 10 volume in-vivo human subset.

Results show that an average Hausdorff distance of 0.34 ± 0.065 mm. The maximum standard deviation is obtained to be 1.77 mm and the average Dice score of 0.864 ± 0.062 voxels/voxels.

3.2 APPLICATIONS TO BONE REGENERATION IN-VIVO USING 3D PSRE

Bone regeneration is a complex multicellular process of growing new bone to heal fractures or bone defects. Scaffolds or bone grafting is used to facilitate bone growth for complicated fractures with large non-unions. Scaffolds acts as carriers for bone growth cells and biochemical factors or provide suitable mechanical conditions [66]. Imaging modalities are critical in monitoring both the integrity of the scaffold and this process of healing postoperatively. Although CT and MRI remain the gold standard for fractures and regenerative processes in-vivo, there are certain barriers: 1) Ionizing radiation can be a risk factor and better resolution comes with the expense of higher dosage levels with regard to CT. Most reproducible experiments show that radiation can delay and damage bone remodeling by reducing osteogenic cell numbers and altering cytokine capacity [67-68]. 2) The scaffold is engineered in such a manner that it is radiolucent in CT. 3) Soft tissue detail is invisible in CT which can hinder imaging earlier stages of bone ossification. 4) In field applications, for which our technology is intended for, the transportation and management of bulky modalities like CT and MRI is infeasible.

US on the other hand offers excellent temporal resolution that is not possible with the above modalities. Although callus formation and differentiation does not convey sonographic contrast, most stages of newly formed ossified bone are visible in US imaging. We propose a 3D rendering of the bone regeneration process highlighting ossified bone, native bone and the scaffold. Certain studies have explored the possibility of 3D bone surface rendering including

ones with non-union fractures [61]. However, to the best of our knowledge, studies incorporating bone regeneration in US imaging has not been investigated. The intensity invariant PSRE technique employed in the previous chapter is extended to include 3D local phase-symmetry features in enhancing the structural information. Bone surface rendering in this scenario is performed in such a way that the 2D phase analysis above is extended to 3D. We have also found that the incorporation of scale and orientation along the elevational direction this reduces the surrounding artifacts and soft tissue significantly. Multiple objects have to be reconstructed including the shell, bone graft, ossified bone and native bone. This makes the problem more complicated.

3.2.1. Experiments

Surgeries were performed by creating a non-union at the tibial bone and placing a scaffold over it to facilitate bone formation. Postop experiments were then performed by scanning 10 sheep at the lateral side of the tibia. US imaging at the 60 and 90-day time points were obtained to monitor the healing process. Volumetric scans were performed by scanning the entire extent of the tibia from the proximal side to the joint connecting the tibia and tarsal bones as shown in Fig 3.10a. The best of three scans were selected the ones that minimized off plane motion. Fig 3.10b shows one associated axial slice with the scaffold on the right and newly formed bone on the left. The scaffold is distinguishable in Fig 3.10b by its reverberating layers (repeated reflective echoes) that can be seen underneath signifying different material properties from the bone.

(a) (b)

Fig 3.10. Postop scan above the tibia at the 90-day timepoint. a) End of the tibia scan with the transducer roughly above the joint. b) Ultrasound image from the scan at the mid-shaft. The scaffold can be seen on the right (antero-lateral side) by its unique reverberating artifact.

3.2.2. Bone ridge enhancement

The 3D ridge enhancement for in-vivo long bone experiments is similar in flavor to the 2D PSRE algorithm with certain modifications. The three-step bone/scaffold enhancement process constitutes: 1) Speckle reduction. 2) Bone fuzzy contrast enhancement. 3) Ridge enhancement using the 3D local phase symmetry model: Speckle reduction follows from the linear first-order statistics filter specified in Chapter 2. Similarly, the second step involving shadow-based fuzzy contrast enhancement is used to reduce the influence of surrounding tissue structures and artifacts. The procedure for obtaining this step is the same as mentioned in Chapter 2 for obtaining the mean pixel intensity feature for classification. Finally, the 2D local phase analysis described in the previous chapter is extended to a 3D PSRE model incorporating the entire volume.

In this case, the construction of the 3D Log-Gabor filter in the spherical coordinate system is given by:

$$G(\omega, \varphi, \theta) = \exp\left[-\left(\frac{\ln\left|\frac{\omega}{\omega_0}\right|^2}{\ln\left|\frac{\kappa}{\omega_0}\right|^2}\right)\right] \times \exp\left[-\left\{\frac{(\phi - \phi_0)^2}{2{\sigma_\varphi}^2} + \frac{(\theta - \theta_0)^2}{2{\sigma_\theta}^2}\right\}\right] \quad (21)$$

where ω_0 is the filter's center frequency given by the reciprocal of the filter scale or $1/s$, ϕ_0 is the zenith orientation of the filter varying in the axial direction, θ_0 is the azimuthal orientation varying in the elevational direction. Empirical parameters were set to be the same as Chapter 2: the Gaussian angular filter spread $\sigma_\varphi = \sigma_\theta = 50^\circ$ and the ratio related to bandwidth $\kappa/\omega_0 =$ 0.33. The band-pass filtered Log-Gabor filter response with spatial coordinates $\mathbf{x} = (x, y, z)^T$ in turn is obtained by convolution with the original 3D US volume. The zero DC component requires that the analysis be done in the frequency domain and then inverted from the fourier space to the spatial domain shown as follows:

$$L(\mathbf{x}) = \mathcal{F}^{-1}\{\mathcal{F}\{f(\mathbf{x})\} \cdot G(\omega, \phi, \theta)\} \quad (22)$$

A single scale and single orientation (one each for zenith and azimuthal angles) is used to construct filter bank in the phase-symmetry model. The parameters were fixed and did not deviate significantly with a larger parameter vector: $\phi_0 = 90^\circ, \theta_0 = 180^\circ$ and $s = 50$. The modified 3D local phase-symmetry model is now denoted by:

$$PS(\mathbf{x}) = \frac{|Re\{L(\mathbf{x})\}| - |Im\{L(\mathbf{x})\}| - T}{\sqrt{(Re\{L(\mathbf{x})\})^2 + (Im\{L(\mathbf{x})\})^2} + \epsilon} \quad (23)$$

Notice that there is no summation involved here due to single scale and orientation vector. Here, ϵ is a small number that prevents division by zero and T is the shrinkage noise threshold calculated from the smallest scale filter response. T is computed to be 3 standard deviations from the mean of the Rayleigh distributed noise as mentioned in the previous chapter. A

morphological area opening of 100 pixels is used to eliminate small false positives that could stem from specular artifacts. The phase-based ridge enhanced output can be used to reconstruct the surface of the scaffold and bone. This results in a large number of gap regions in the output due to the transition between native bone – scaffold, newly ossified bone – scaffold and, native bone - newly ossified bone. Along with the minimal possibility of false positives that arise from surrounding tissue structures, there is a risk of muddying observer judgement in classifying bone among the transition regions. These complications can be alleviated to an extent by filling the concave regions below the bone surface to preserve continuity between slices.

3.2.3. Concave region filling and 3D surface rendering

Region filling of the concavities within each bone or scaffold point set can be accomplished by unifying all point sets to a convex set. The definition of a convex set is given as follows:

Definition 3.1. - *Let* $C \subseteq \mathbb{R}^n$ *be any set.* C *is convex if* $\lambda x + (1-\lambda)y$ *such that* $\forall x, y \in C$ *and* $\forall \lambda \in [0,1]$.

A convex hull is then used to mask both the bone/scaffold point set and its associated concavity. This is then followed by tapering the region above the unified point set. The convex hull $Conv(B) \subseteq \mathbb{R}^3$ is the smallest convex set containing the 3D bone(s) point set of blobs $B = \left\{ \left(b_x^{(i)} \;\; b_y^{(i)} \;\; b_z^{(i)} \right)^T \middle| \; i = 1,2,..|B| \right\}$. This is equivalent to all the possible convex combinations of points such that.:

$$Conv(B) = \left\{ \sum_{i=1}^{|B|} \lambda_i . \left(b_x^{(i)} \;\; b_y^{(i)} \;\; b_z^{(i)} \right)^T \middle| \forall i, \lambda_i > 0 \;\; and \;\; \sum_{i=1}^{|B|} \lambda_i = 1 \right\} \qquad (24)$$

In order to fill concave regions below the bone surface, we will add a constraint to the above set. The resulting convex hull $Conv(B) = \left\{ \left(c_x^{(j)} \;\; c_y^{(j)} \;\; c_z^{(j)} \right)^T \;\middle|\; j = 1,2,..|C| \right\}$ is bounded by bone points from above (opposite to the direction of the ultrasound beam) such that:

$$Conv_F(B) = \left\{ \left(c_x^{(j)} \;\; c_y^{(j)} \;\; c_z^{(j)} \right)^T \;\middle|\; \forall c_z^{(j)} \; \forall \left(c_x^{(j)} = b_x^{(i)} \right), \; c_y^{(j)} \geq b_y^{(i)} \right\} \qquad (25)$$

The concave region filled 3D bone point set $Conv_F(B)$ is then smoothed with an 8×8×8 gaussian filter. A 3D reconstruction is performed using the open-source ImageVis3D as mentioned in the previous section.

3.2.4. Qualitative Results

The results from the 3D rendering are generated by scaling the dimensions associated with the CT model. The following results show the tibia bone regeneration process at a 60-day time point obtained from 3 sheep. The scaffold is highlighted in pale yellow. Since scaffold is radiolucent, it is invisible in the CT rendering. Fig 3.10 represents segmented volumetric data from a single sheep. Fig 3.11 represents the same for two other sheep. Fig 3.10a shows the 3D surface rendering obtained using 3D PSRE without concave region filling. Fig 3.10b shows the same after applying of the concave region filling method. Fig 3.10c shows the equivalent 3D rendering obtained using CT. The most prominent characteristics of the US 3D renderings visible in the CT are marked with a blue circle. As is evidenced by the images, Fig 3.10b, Fig 3.11a and Fig 3.11c shows a smoother output with the primary feature correspondences intact. Notice the 3D US renderings do not show the fractured bone underneath the surface of the newly formed bone unlike its Ct counterpart due to US limitations mentioned in the above sections. But, all the ultrasound 3D renderings show a higher quantity of ossified bone growth on the surface.

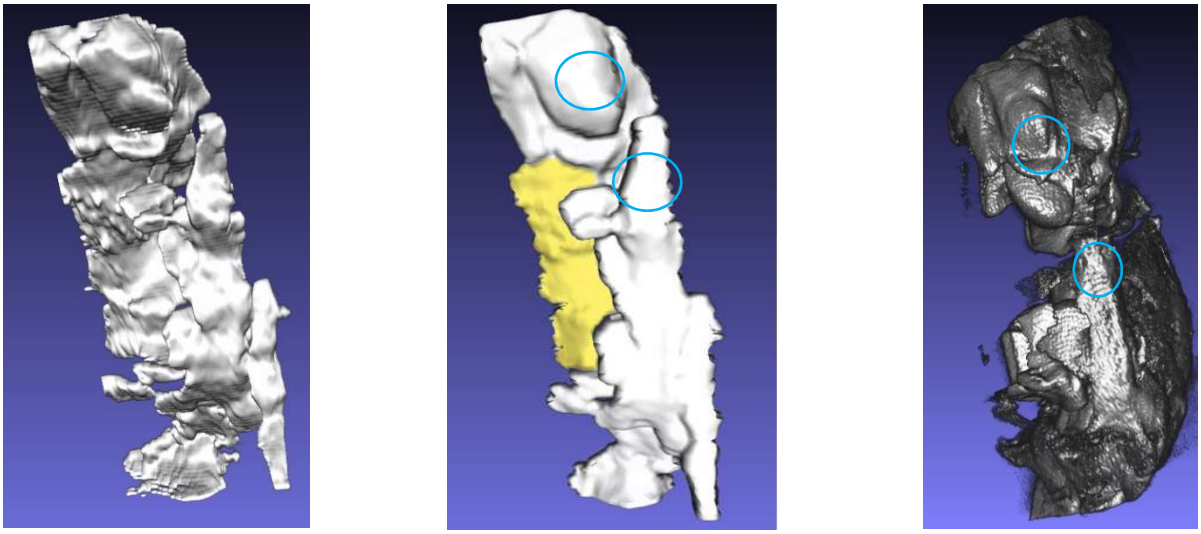

(a) (b) (c)

Fig 3.11. Tibia bone regenerating at 60 days from sheep 1. Scaffold is shown in yellow. a) Ultrasound 3D rendering with concave region filling. The blue circle marks key feature correspondences. b) Ultrasound 3D rendering with concave region filling. c) Associated CT 3D rendering.

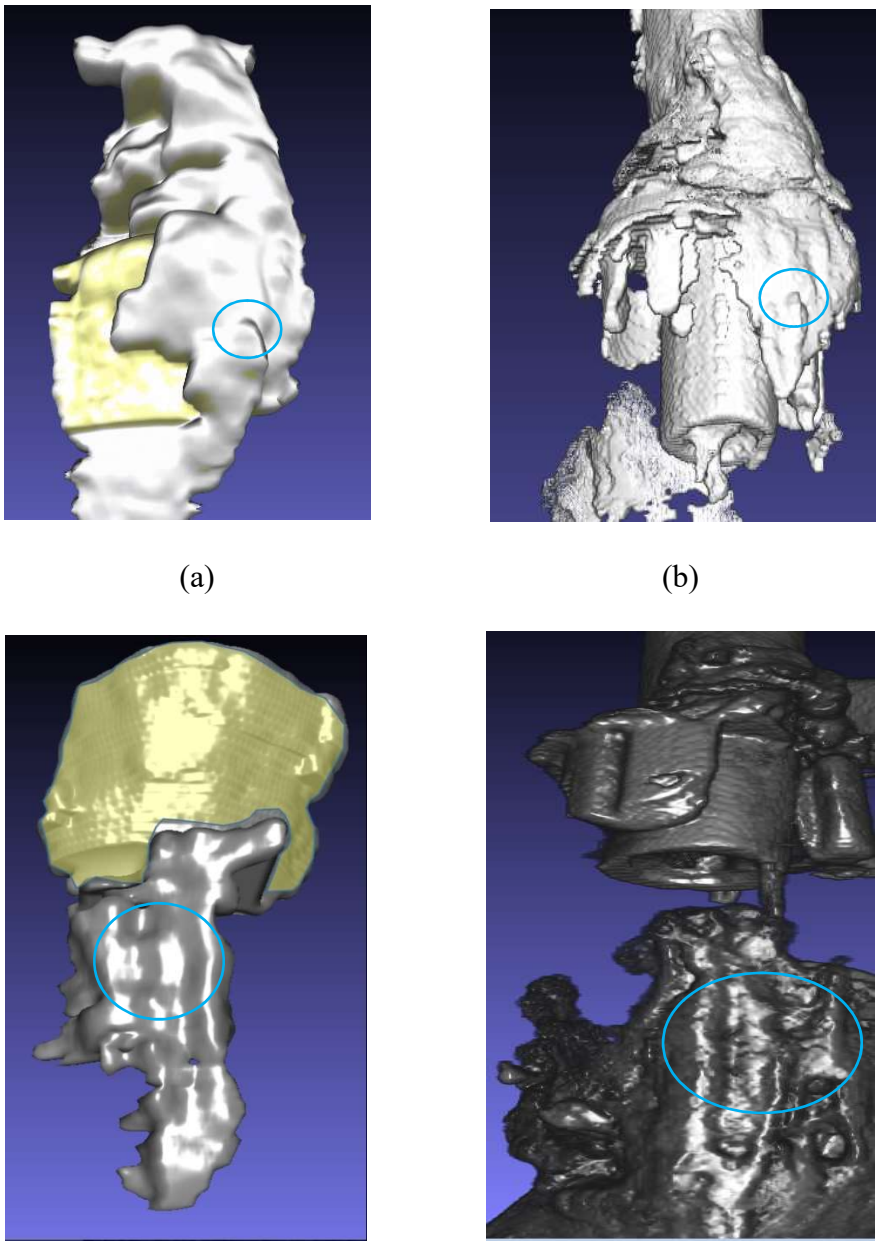

(a) (b)

(c) (d)

Fig 3.12. Tibia bone regenerating at 60 days from two sheep. Scaffold is shown in yellow. The results are generated by 3D PSRE and concave region filling. The blue circle marks key feature correspondences. a) Ultrasound 3D rendering from sheep 2. b) CT 3D rendering from sheep 2. c) Ultrasound 3D rendering from sheep 3. d) CT 3D rendering from sheep 3.

3.3 DISCUSSION AND CONCLUSION

This chapter deals with the 3D surface rendering of the intact spine for human in-vivo and rabbits ex-vivo. The feasibility of the method can be extended to applications like regional anesthesia, pedicle screw fixation and postoperative bone growth. Our study's results show that the posterior surfaces of multiple vertebrae can be automatically reconstructed without any manual intervention. Each US image is segmented using the phase-based ridge enhancement and classification method mentioned in the previous chapter. The segmented slices are the stitched together to form a 3D volume of the vertebrae. The proposed method is assessed by testing the 3D automatically segmented surfaces against manual delineation by a radiologist. (Results). The width of the curvilinear transducer is also sufficient in covering the entire field of view of the posterior vertebrae. Consequently, sophisticated panoramic volume stitching techniques may not be required. However, this not true for long bones. US can be important got military applications where transportation and management of bulky equipment like CT or MRI can be infeasible. While the method does not extract the anterior column or deeper regions of the middle column and spinous process, there is much information to be exploited from the posterior side especially for the above applications. The results show that vertebrae structural landmarks such as the top surface of the SP, AP, TP laminae and interspaces can be reliably extracted and observable in the 3D reconstruction. This way an anesthesiologist is not restricted to identifying the interspaces from either the paramedian or transverse planes alone. Thus, they can guide an epidural needle by recognizing that the interspace is mostly a level surface in between structural landmarks like the SP and AP. Furthermore, spine surgeons can use the 3D rendering to identify landmarks such as the AP and laminae in placing pedicle screws for vertebrae stabilization. Utilization of image

phase information also makes the technique not sensitive to the transducer beam orientations or contrast conditions.

Although the qualitative and qualitative results are promising, there are some improvements to be addressed. An important disadvantage in our technique is the lack of transducer position information. Since US is a heavily operator dependent modality, pose estimation of the transducer is a critical step in obtaining accurate 3D renderings. As the number of vertebrae increases this becomes more of a necessity. It can also be crucial for estimating kyphotic and lordotic angles in scoliosis identification. With regard to the applications mentioned in this chapter, tracking positions helps the surgeon in determining the precise location of placing anchor points. Knowing the position of the interspace can also guide anesthesiologists in accurate epidural placement. However, the most critical quantifiable information that an anesthesiologist would require is the depth from the skin to epidural space which the proposed technique provides. For an untrained operator, augmenting transducer position information can be crucial since there is a high possibility for scanning away from the midline and at oblique orientations. The proposed techniques can still be deemed useful by scanning along the midline minimizing off plane motion. Besides, multiple studies have proven the feasibility of enhancing 3D reconstructions by adding transducer positioning hardware within a closed loop framework. Position tracked 3D US images are also vital for extracting quantifiable information in validation studies involving other modalities like CT or MRI. Despite having such advantages, the additional hardware demanded in such a computer assisted framework can also be infeasible in emergency departments, field-based applications or even present itself as a cost burden in

developing countries. Such inherent limitations can be possibly evaded with the advent of miniatured accelerometer systems that can be cheaply made and shielded onto the transducer.

A promising arena within which the proposed method can be useful for is the postoperative surgery scenario. Radiation risk, by employing CT or radiographs, to a bone in the process of restoration can be alleviated by the US based methods. Bone healing enabled by the grafts after spinal fusion surgeries can be evaluated by 3D reconstruction of the posterior vertebral surface. The availability of generalized statistical shape models of the vertebrae can also be used to register the spine surface information. This can have important implications in field or emergency department scenarios by eliminating the need for extensive positioning hardware. The feasibility of visualizing and tracking newly formed ossified tibial bone has also been explored. The applicability to bone healing in the context of spine has not been investigated in this thesis.

Optimal log-gabor filter parameter estimations accounts for varying orientations of each protrusion on the posterior vertebrae. However, for the bone regeneration scenario, a single scale and orientation analysis suffice. This due to the general level surface posited by lone bone surfaces. Bone surfaces obeying more complex geometries may benefit from a larger parameter space. The computation time has also been significantly reduced. A smoother response can be produced with 3D phase features. However, this would require the computation of a 3D radon transform to determine the that could compound computation time. However, for a single vertebra we expect three azimuthal and one elevational angle to capture the filter orientations. A fixed elevational angle is sufficient due to single oblique angles seen in the paramedian plane.

These volumes can be sectioned into vertebra and interspace region. Multiple scales and orientation also increase the algorithmic complexity and processing times.

One of the drawbacks of optimal parameterization is that it is performed for each image in the volume. Thus, the parameter vector may vary across slices in the elevational direction. This can be inconsistent for the overall 3D volume. Thus, we extend our 2D to 3D phase analysis in bone regeneration. This preserves consistency in the parametrization and thus continuity between slices. The proposed method of 3D reconstruction of vertebral and bone surfaces accurately captures sufficient structural information on the posterior spine and bone regeneration for regional anesthesia, pedicle screw placement and postoperative bone growth evaluation applications.

CHAPTER 4

MODELING AND ANALYSIS OF ULTRASOUND ELASTOGRAPHIC AXIAL STRAINS IN AIDING SPINE FRACTURE LOCALIZATION

4.1 INTRODUCTION

Ultrasound (US) imaging modalities are known for their safety, superior spatial and temporal resolutions, portability and cost-effectiveness. Spinal ultrasound imaging, due to its real-time capability, has been quite well received in the clinical setting for aiding epidural administration and scoliosis detection [69-74]. Applying established techniques in bone detection for the spine can prove to be challenging due to its complex geometry. Yet there has been a growing body of work in the automatic extraction of vertebral surface information. Template driven techniques have been used to detect the laminae and epidural space [71]. Berton et al. proposed automatic segmentation of the superficial spinous process (SP) and acoustic shadow regions [72]. 2D superficial SP detection has also been extended to the entire vertebral column [14]. While this is important progress to scoliosis identification for which a 3D projection may be sufficient, it does not account for the entire SP surface. In fact, only echoes returning from a small "blobbed" area above the spinous process's tip can produce discernible contrast ([72,74]). But its side edges in the sonograms lack a clear definition presumably due to the complex phenomenon of refraction and oblique reflection. As a result, a slight tilt in the spinous process may not be apparent when observed in the transverse view. Moreover, to the best of our knowledge, the above techniques have yet to be contextualized for spinal fractures. The studies retrievable in the literature that deal with fracture detection have been devoted to long bone studies [75-76]. This may be partly due to the fact that spinal ultrasound imaging permits little to no penetration beyond the bone surface. So,

the vertebral body surface cannot be reliably observed thereby limiting the visibility of anterior or middle column fractures. That said, fractures at the posterior column which includes bony protrusions such as the SP, articular process (AP) and transverse process (TP) can provide important diagnostic information. Recognition of these fracture patterns may lead radiologists to infer the likelihood of surrounding soft tissue/neurological injuries. For example, spondylolisthesis appears strongly associated with the occurrence of SP fracture after interspinous process surgery [77]. Also, integrity of the surrounding posterior ligamentous complex is a primary decision-making criterion in assessing spinal stability along with morphology of the fracture. In addition, multiple fractures could contribute to a higher likelihood of spinal instability. Posterior element fractures are difficult to detect from two-dimensional B-mode images due to the inherently low SNR and spatial resolution particularly between fracture segments. Owing to its unpredictable geometry, fractures can be very hard to generalize for statistical shape models obtained from a patient population [45]. Techniques including intensity invariant phase-based methodologies derived from B-mode images can also be prone to low spatial resolution resulting in merging of the fracture sites [47, 71, 75]. We aim to address some of these limitations using ultrasound elastography based strain information at the vertebra-soft tissue boundary.

Ultrasound elastography (USE) has been shown to successfully assess changes in mechanical properties of tissues such as stiffness due to an underlying pathology [78]. The technique has been shown to be feasible in detecting several cancers and liver diseases [79, 80]. According to USE, strains experienced by the tissue under compression relate to its underlying mechanical properties. While axial normal strain elastography (ANSE) has been customarily used to assess the stiffness, other branches of USE have evolved, which aim at measuring new mechanical parameters [81,

82]. One such branch is the axial shear strain elastography (ASSE) that estimates the axial component of shear strains. The hypothesis for ASSE is that, for a non-homogenous tissue under quasi-static uniaxial compression, axial shear strains are produced at the boundaries between the different tissue's components [84]. These shear strains may carry important information, not just about the boundary but about the pathology and structure of the region of interest (ROI) itself [83, 85]. Recently, our lab has presented a study on intact and fractured long bones to obtain elastographic patterns of fracture diagnosis relevance at the bone/soft tissue interface [76].

Our objective is to use elastographic techniques to create contrast mechanisms that factor in the relative stiffness and slippage of the vertebrae and surrounding soft tissues on application of a compressive force. In this study, we use ex-vivo rabbits as our testing specimen. Finite element (FE) elastography simulations and actual experiments are then used to independently analyze strains that could adequately locate the fracture site. Additionally, we have proposed a method for generating strain-based morphological descriptors such as orientation and asymmetry that would in turn aid in the fracture detection process. Finally, statistical analyses are performed to evaluate the significance of the proposed descriptors.

4.1 METHODS

4.1.1. Finite Element Modeling

In order to construct the FE models of bones, an accurate construction of the 3D geometry, appropriate material properties and boundary conditions in the form of applied loads and constraints as well as the bonding at different constitutive components' interfaces should be

considered and developed. We use a 3D FE model to understand the biomechanical behavior of the soft tissue and spine and how it changes in the presence of a fracture.

In the present study, we assume a linear elastic behavior for all constituent materials. The loading on the model is assumed to be static. Thus, the problem is governed by

$$. \nabla \cdot \boldsymbol{\sigma} + \mathbf{f} = 0 \tag{26}$$

σ and **f** are the total stress tensor and body force vector per unit volume, respectively. The linear constitutive behavior is given as

$$\boldsymbol{\sigma} = E\boldsymbol{\varepsilon}, \tag{27}$$

where **ε** is the strain tensor and E is a tensor of corresponding elastic constants. By assuming isotropic elasticity, E can be fully determined using the constitutive material's Young's modulus and poisson's ratio.

The FE modeling procedure for the three-dimensional displacement and strain fields of the fractured and intact vertebra-tissue models under compression is shown in Fig 4.1. Axial slices of the CT image were obtained from rabbit saddle samples (each in intact or fractured conditions) via an Axiom Artis C-arm (d)FC (Siemens Healthcare). Images were then imported into Amira 6.0 (FEI Visualization Sciences Group, Bordeaux, France and the Zuse Institute Berlin, Germany) for vertebra shape segmentation. A solid geometric representation was generated using Rhinoceros 5.0 (Robert McNeel & Associates, Seattle, WA, USA). This platform was used to convert these surface geometries to a non-uniform rational B-spline (NURB) surface. The final solid assembly was finished in CAD (SolidWorks, Dassault Systemes SolidWorks Corp., MA, USA) by combining the spine model with a soft tissue rectangular parallelepiped (40×40×40 mm^3 or

50×40×40 mm^3) adjusted for the vertebra's size. Friction behavior at the vertebra-soft tissue interface obeyed the exponential decay friction model consisting of static, kinetic friction coefficients (μ_s = 0.3, $\mu_k = 0.05$) and decay coefficient ($d_c = 0.1$). For boundary conditions, the bottom of the soft tissue region was fixed (the displacements in all directions are zero.) and the displacement in axial direction was specified as 0.2 mm (0.5% compression) at the top of the tissue. The remaining sides of the tissue were set to be free. Then, each vertebra-soft tissue model was discretized into a non-uniform mesh of tetrahedral elements. After modeling, a static stress analysis was carried out to obtain displacement and strain fields on the soft tissues. FE simulations were performed on the supercomputers located at the Texas A&M High Performance Research Computing (HPRC) facility.

Material	**Young's modulus, *E* (MPa)**	**Poisson's ratio, *v***
Soft tissue	1.53×10^{-3}	0.46
Vertebra	4014	0.3
Reference	[86], [87]	[86], [87]

Table 4.1. Material properties of soft tissue and the lumbar vertebra.

Create surface geometry

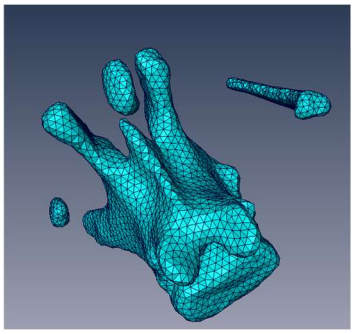

Fractured vertebra

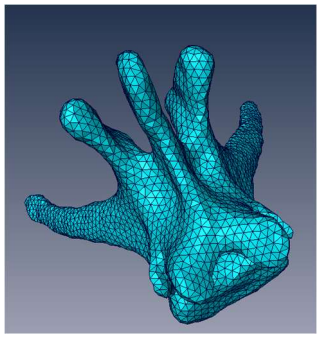

Intact vertebra

Assign material properties & boundary conditions / Generate mesh

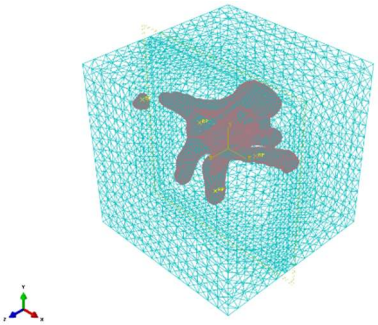

Fractured vertebra-tissue

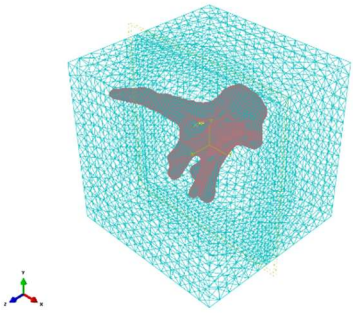

Intact vertebra-tissue

Finite element analysis

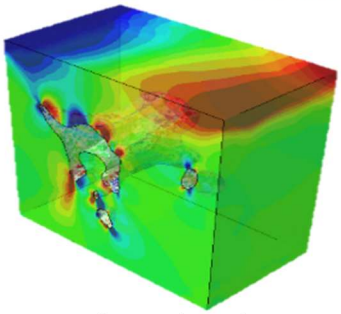

Fractured vertebra-tissue

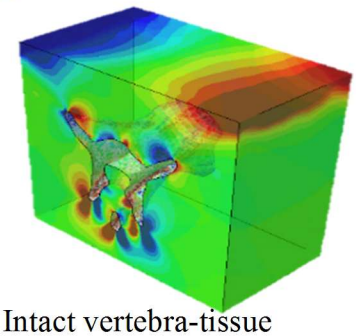

Intact vertebra-tissue

Fig 4.1. Procedure for FE modeling incorporating soft tissue and lumbar vertebra under compression.

4.1.2 Ultrasound Simulation Framework

The mechanical simulation tool allows generation of 3D FE simulation models for each experiment being performed. The resulting simulated mechanical displacements were then used as input to our ultrasound simulation software module as described in [88]. In this model, the point spread function (PSF), which is the impulse response of the system, was convolved with the scattering function (normal distribution of scatterer amplitudes) to obtain the radiofrequency (RF) signals. The simulated transducer configuration follow that in our earlier paper [90]. From the simulated RF data, axial normal and axial shear strain elastograms were obtained using cross-correlation methods. For our study, the length of correlation window for both pre- and stretched post-compression RF signal was chosen as 1.2 mm with 80% overlap between consecutive windows.

4.1.2. Experiments

Five intact rabbit saddles and five more fractured using blunt force trauma were used in this study. Each rabbit was placed in a phantom made with 5% gelatin and 3% agar. The ultrasound transducer fixated onto a compressor plate was then placed in contact with the phantom's top surface using a gel that served as a coupling medium. The sonographic data were acquired using a 38 mm linear array transducer (Sonix RP, Ultrasonix, Richmond, BC, Canada) while the uniaxial compression was being applied via the transducer/compressor combination. The system configuration and data processing protocols refer to a previous study in our lab [90]. Correlation maps were generated by cross-correlating the pre- and post-compressed RF data. These maps indicate the reliability of the strain estimation. Elastograms were further normalized with respect to the mean strain value of a patch in the axial normal strain elastogram representing the soft

tissue region with high correlation values [76]. The complementary value of the elastograms for fracture localization will be illustrated in this paper using composite images. For the purpose of comparing the spine surface localization performance, bony regions of the vertebra were also automatically extracted from only the B-mode images using a phase-based ridge segmentation technique the details of which are described in [74].

4.1.3. Morphological Strain Descriptors for Spine fracture localization

4.1.3.1. Axial normal strain description using distribution-wise symmetry

From our previous study on long bones, it has been demonstrated that the axial normal strains have a tendency to localize at the bone-soft tissue interface, and its local distribution changes in presence of a fracture [76]. Therefore, if a vertebra contains a fracture at the spinous process, a laterally skewed distribution of corresponding strains would be expected, which essentially arises from asymmetric boundary conditions posed by the fractured vertebra. In other words, multiple fractures can lead to half of the transverse imaging plane along the midline (the line parallel to the transverse/axial axis and perpendicular to the axis on which the transducer rests for probing vertebrae) appearing “stiffer” than the other half. We will illustrate this effect by “projecting” the 3D axial normal strain elastogram volumes along the axial direction to help holistically interpret the strain profile. This is obtained by computing the median value of each column from the top to the vertebra-soft tissue boundary within a stack of axial normal strain elastographic slices. A second projection of strain fields on the lateral axis identifies the highest concentration of strains for a single vertebra.

4.1.3.2. Axial shear strain description using principal orientation

Axial shear strains have been demonstrated in our past studies to localize the long bone fracture sites with high CNR. And this is attributed to the fact that discontinuity in the material composition can in general create bidirectional slippage at the interface when compressed uniaxially. However, due to the complexity of spine geometry in 3-D, directly obtaining fracture information from the slippage becomes difficult. [76, 90]. On the other hand, the posterior column of the spine consists of bony protrusions that exhibit unique shape characteristics. An orientation descriptor of the SP in particular can be determined by its deviation from the midline of the transverse (axial slice) cross-section. We quantify this deviation as being the orientation between the straight line passing through the SP and the lateral axis. At the midline, this orientation would ideally amount to 90 degrees signifying zero deviation. Since ultrasound hardly penetrates bones, this orientation information is almost entirely absent in the B-mode images. For axial shear strain elastograms, however, due to the fact that they highlight pointwise discontinuities from the side edges of the spine protrusions, we can see that the SP fracture morphology is easier to glean from them.

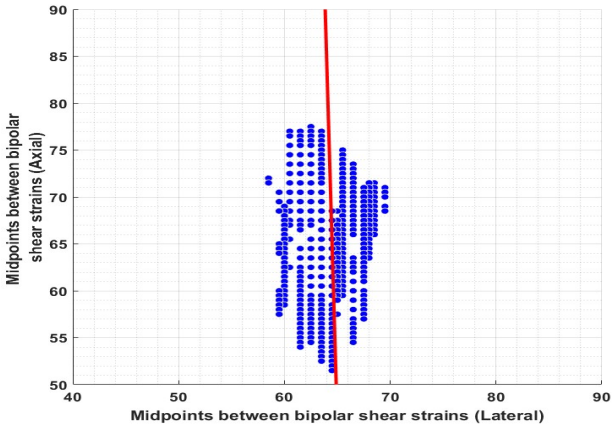

Fig 4.2. Principal orientation obtained from the linear model (red) passing through midpoints (blue) obtained from the axial shear strain elastogram of an intact case.

Principal orientation of the SP is therefore approximated by the following two steps. First, pairwise distances between points in the positive and negative axial shear strain clusters are extracted using a Frechet distance measure. The Frechet distance (M pairwise distances) between positive and negative shear strain cluster of coordinates S^+ and S^- is given by:

$$d(S^+, S^-) = \inf_{\alpha,\beta:[1,M]\to[1,M]} \max_{x\epsilon[1,M]} \left\| S^+\big(\alpha(x)\big) - S^-(\beta(x)) \right\|^2 \quad (28)$$

where α and β $(\beta > \alpha)$ are curves running through each coordinate x in clusters S^+ and S^- respectively. In order to determine the points of both curves that maximize separation between the clusters, we use the midpoints of the Frechet distances:

$$mid(S^+, S^-) = 0.5 \cdot \Big(S^+\big(\alpha(x)\big) + S^-\big(\beta(x)\big) \Big) \quad (29)$$

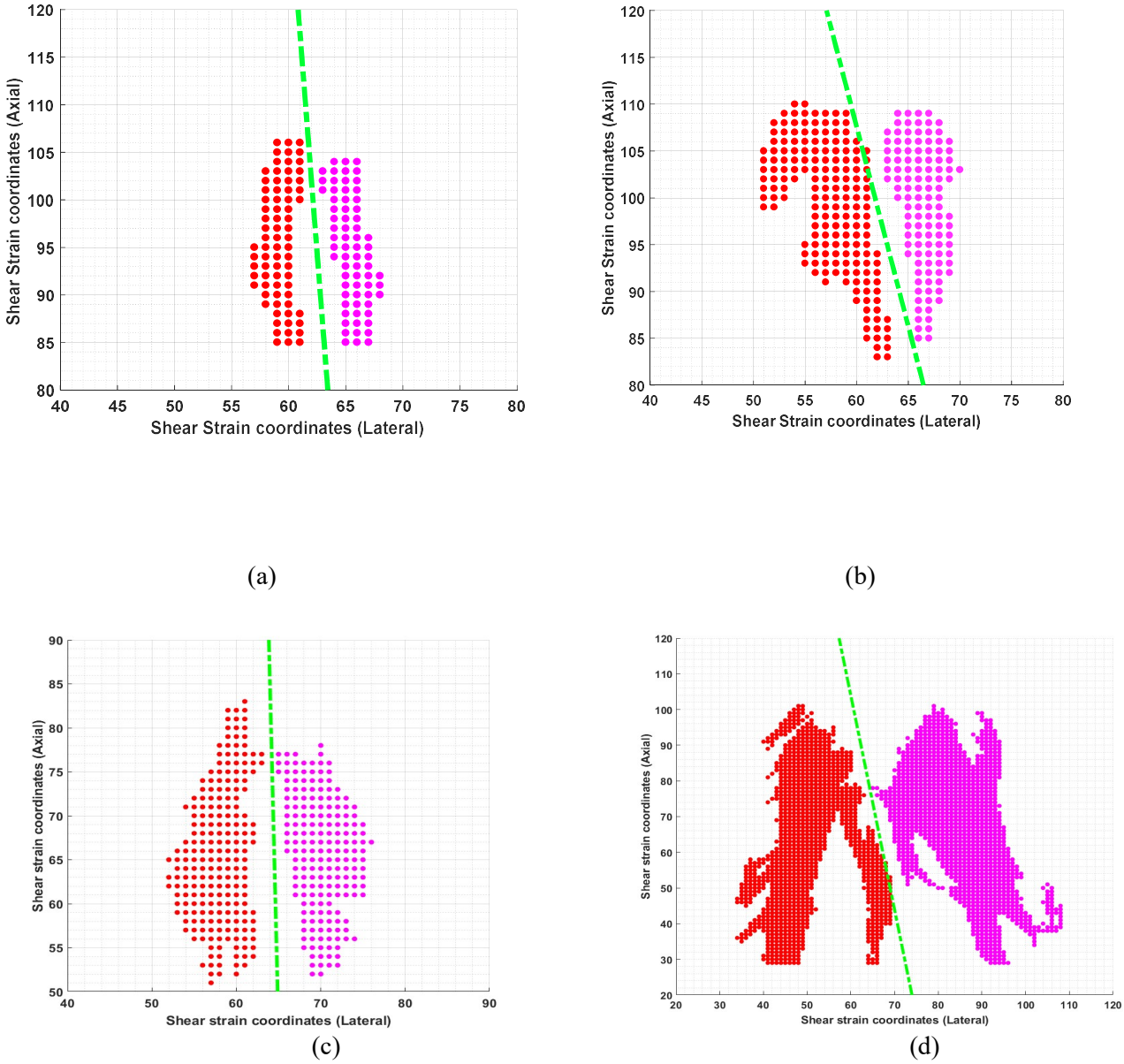

Fig 4.3. Principal orientation (green) between positive (red) and negative (magenta) shear strains for axial slice surrounding the a) Intact SP from the ultrasound simulation. b) Fractured SP from the ultrasound simulation. a) Intact SP from the experiments. b) Fractured SP from the experiments.

Second, a linear least-squares regression model is applied to fit the midpoints, and the orientation can then be computed from the slopes of the fitting lines. Fig 4.2 showcases the midpoints and the linear model for an intact SP. And illustrated in Fig 4.3 is the principal orientation of the shear strain as the angle of the green line with respect to the lateral axis. Clearly, the Fig 4.3a and Fig 4.3c orientations demonstrate a closer angle to the midline. Note that this algorithm does not work for unipolar (positive or negative) strains. In such a scenario we compute the eigenvector of the covariance matrix encoding the shear strain unipolar coordinates to obtain orientation of a single cluster.

4.1.4.3. Statistical Analysis

Fifty ANSE and ASSE simulation and experiment images were used for the statistical assessment of the fractures' influence on the strains. Thresholding (parameters detailed in [74]) was in general performed and test statistics were then constructed from the thresholded images. As for the simulation results, Mann-Whitney U tests were performed to evaluate whether there were differences in the mean and peak value of the thresholded strains between fracture and intact cases. Paired t-tests were performed to test whether there were a higher number of bipolar/unipolar patterns in the fracture as a result of the strain disruption. Principal orientations of the shear strains around the SP were obtained from both simulations and experiments. A non-parametric smoothing kernel was used to fit the distributions and estimate orientation thresholds for an intact SP. For the experimental data analysis, in addition, Wilcoxon signed rank tests were performed to test for the asymmetric strain distribution experienced by fracture cases. The degree of asymmetry was obtained by the difference between the peak value of the median strain projection from the left and right half of each axial normal strain elastogram.

4.3 RESULTS

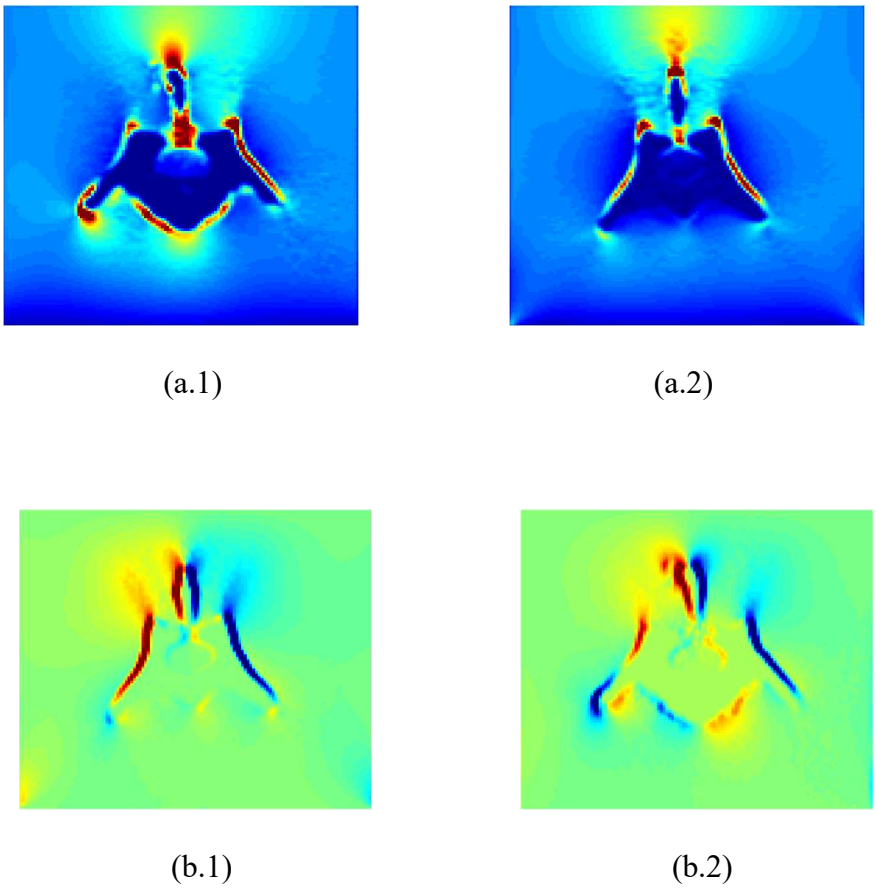

(a.1) (a.2)

(b.1) (b.2)

Fig 4.4. Ideal axial strain and axial shear strain maps.

Fig 4.4a shows the ideal axial slice representing normal strains for an intact and fractured vertebra respectively. High strain regions are accumulated at the interface of soft tissue and the respective bony protrusion (SP in this illustration). Fig 4.4c and Fig 4.4d show the shear strains. Shear strains show an existence of bipolar (positive and negative) strain regions accumulated around the bony protrusion. It is clear from this depiction that the presence of a fracture site can be qualified through the strain concentration region's abnormal geometry. These characteristics can also be observed after application of the ultrasound simulation in Fig 4.5. The first column represents one axial slice from an intact spine and the rest correspond to cases obtained from

spines with a fractured SP and fractured TP, and a fractured SP and left AP, respectively. A common trait among the axial normal strain elastograms of fractured spine columns (Fig 4.4a.2, Fig 4.5a.2, Fig 4.5a.3), is the shifting of the higher magnitude portion of strain fields away from the midline (middle column). Whereas in the axial shear strain elastograms, bipolar and unipolar axial shear strain elastographic patterns in Fig 4.5 are visible around the protrusions and their broken fragments. In particular, Fig 4.5b.3 shows a unipolar pattern around the left fragment of the left AP.

The 3D distributions in Fig 4.6 represent normal strains around a single vertebra with the sample in each column corresponding to that in Fig 4.5a. It is clear from Fig 4.6(a) that the median axial normal strain around the SP (roughly at A-line 64) is higher than those around the AP, and strain values at the bony regions are in general higher than in the background. Most importantly, it indicates symmetrical strain distributed across the spinal protrusions. Fig 4.6c shows the strains asymmetrically distributed with the right AP experiencing a majority of the compressive strain from above. On the other hand, Fig 4.6b shows an isolated SP fracture. While these strains are asymmetrically distributed in both columns b and c, the strains around the SP in Fig 4.6c have been significantly compromised compared to Fig 4.6b. In addition, multiple fractures can be observed at the SP, left AP and right TP in Fig 4.6c which appears to indicate a very high likelihood of spinal instability. This could potentially pave the way for an assessment of stability by tracking strain distributions and their large deviation from axial symmetry. Fig 4.7 shows the filled contour plot at the median coronal slice for the 3D axial normal strain distribution in Fig 4.6c. We observe an elevational asymmetry of the distributions in terms of contour line direction. Two local maxima around the SP have been highlighted. This can be corroborated with the 3D

rendering of the vertebra above in Fig 4.6c showing the SP fracture segments in opposing directions.

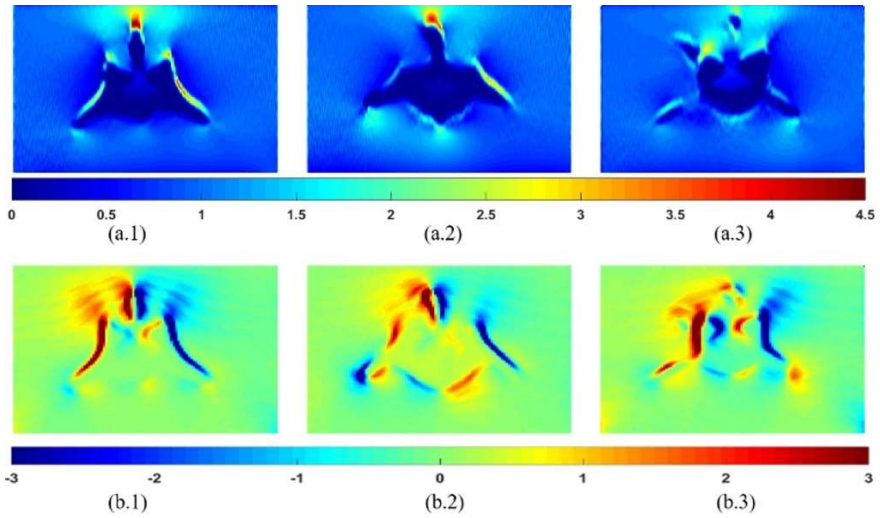

Fig 4.5. Elastograms from the ultrasound simulation showing an axial slice of the intact (first column) case, fracture at the SP (second column), fracture at the SP and left AP (third column) from three vertebrae. a) axial normal strain elastograms. b) axial shear strain elastograms.

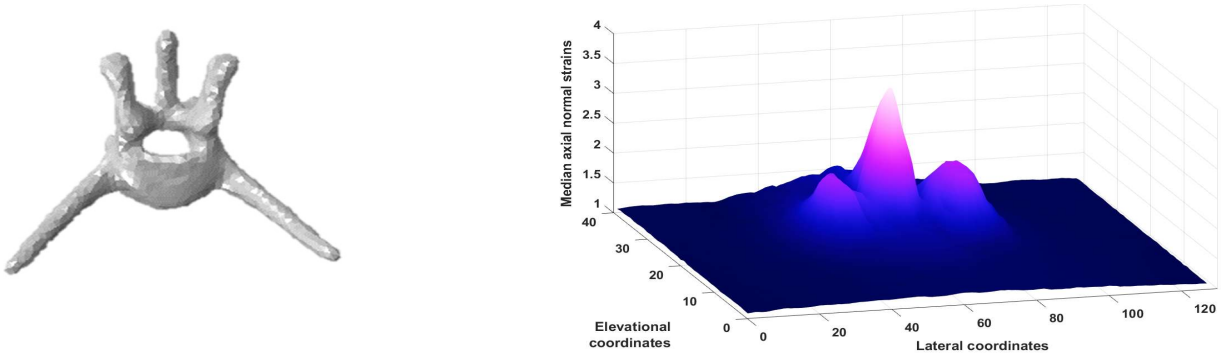

(a)

Fig 4.6. 3D rendering of spines from CT (top) and their associated median projection of axial normal strains (bottom). Large local maxima correspond to bony protrusions of the posterior spine. a) Intact L3 vertebra. The projection is symmetric in this case. b) L7 vertebra with

multiple fracture sites at the SP and left TP. c) L4 vertebra with multiple fracture sites at the SP, left AP and right TP. d) L5 vertebra with multiple fracture sites at the SP, left AP and right TP.

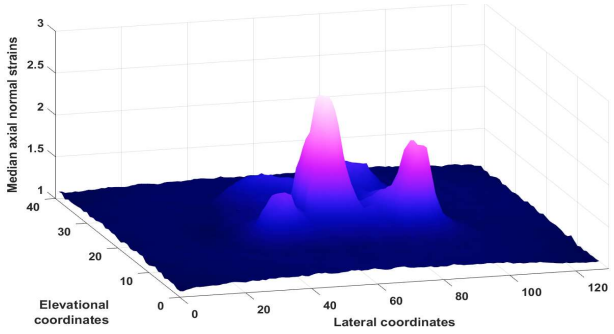

(b)

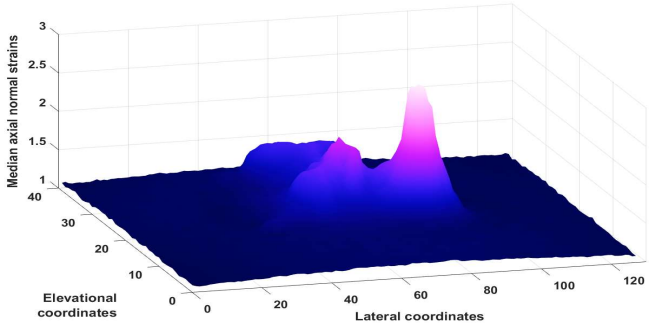

(c)

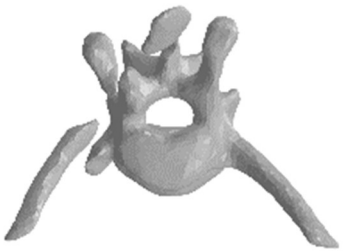

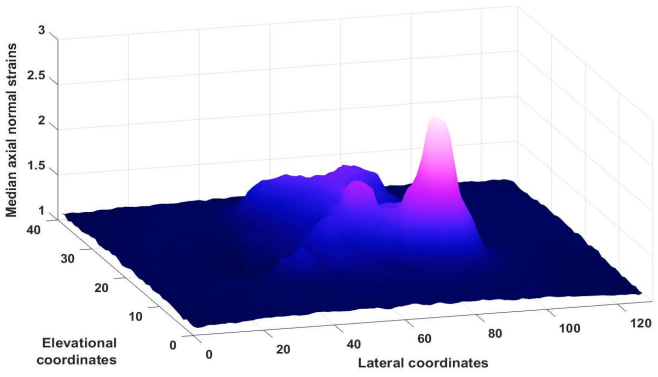

(d)

Fig 4.6. Continued.

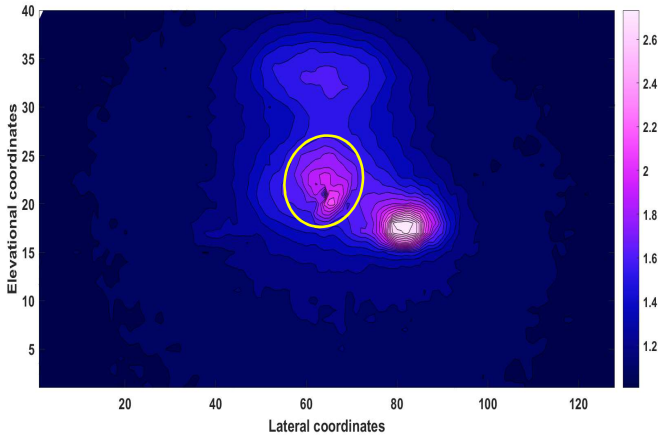

Fig 4.7. Filled contour plot of the median coronal slice obtained from the spine model in Fig 4.6c with multiple fracture sites at the SP and left AP (unstable).

Fig 4.8 shows the principal orientations in simulated axial shear strain elastograms of the fractured and intact SP. The histogram in yellow (Median (Med): 89.21˚, Interquartile range (IQR): 88.3 - 89.8˚) corresponds to the intact cases and the cyan histogram (Med: 77˚, IQR: 71.8 – 81˚) corresponds to the fracture cases. From the smoothing kernels, an orientation threshold of 86.5 degrees was estimated for an intact SP.

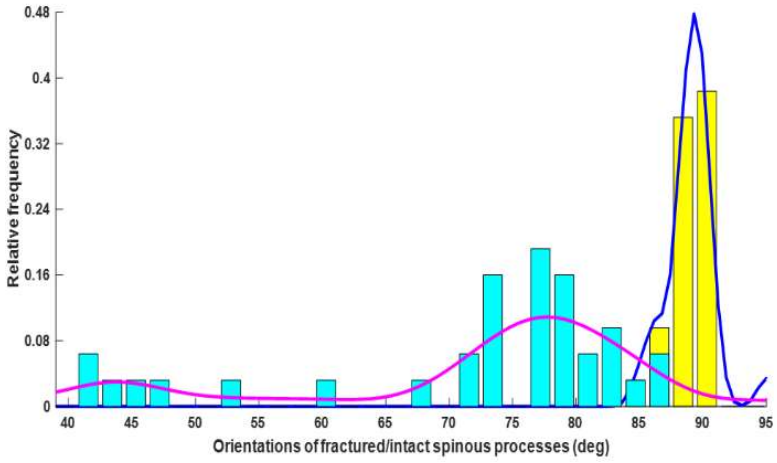

Fig 4.8. Histograms of axial shear strain elastogram principal orientations with fractured (cyan bars) and intact (yellow bars) SP as extracted from the simulations.

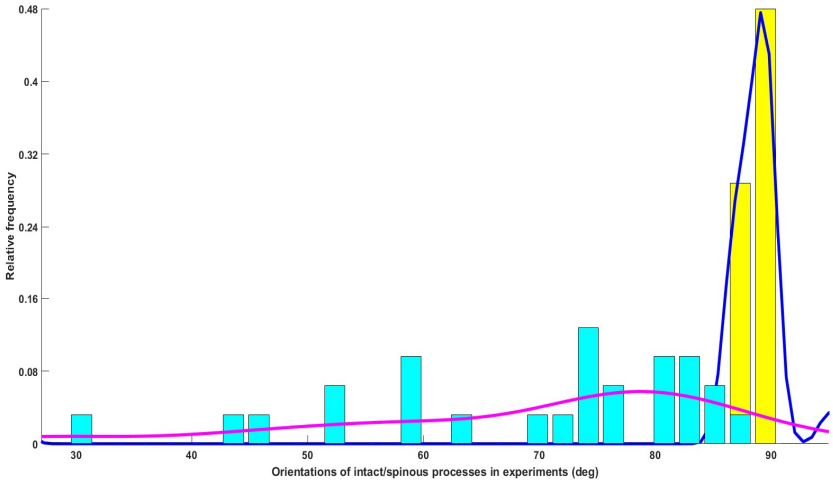

Fig 4.9. Histograms of axial shear strain elastogram principal orientations with fractured (cyan bars) and intact (yellow bars) SP as extracted from the experiments.

Table 4.2 shows the paired t-test comparing the number of bipolar and unipolar strains in simulated axial shear strain elastograms between intact and fracture cases (H_a: $\mu_{fracture} > \mu_{intact}$). The number of bipolar patterns is greater on average for fractured vertebrae ($\alpha = 0.01$).

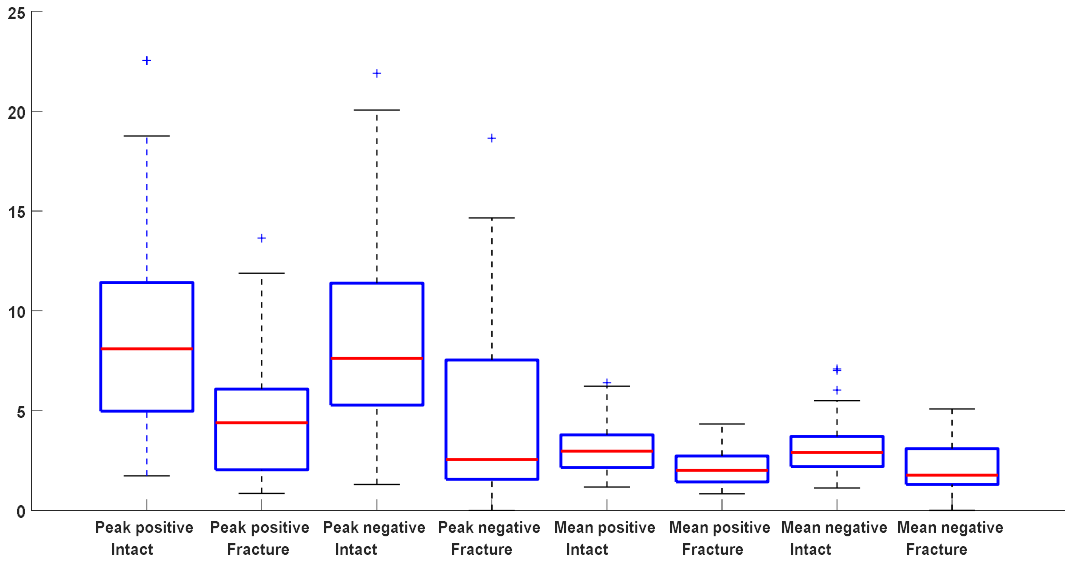

Fig 4.10. Boxplot comparison of axial shear strain elastographic features from the simulations on intact and fractured vertebrae.

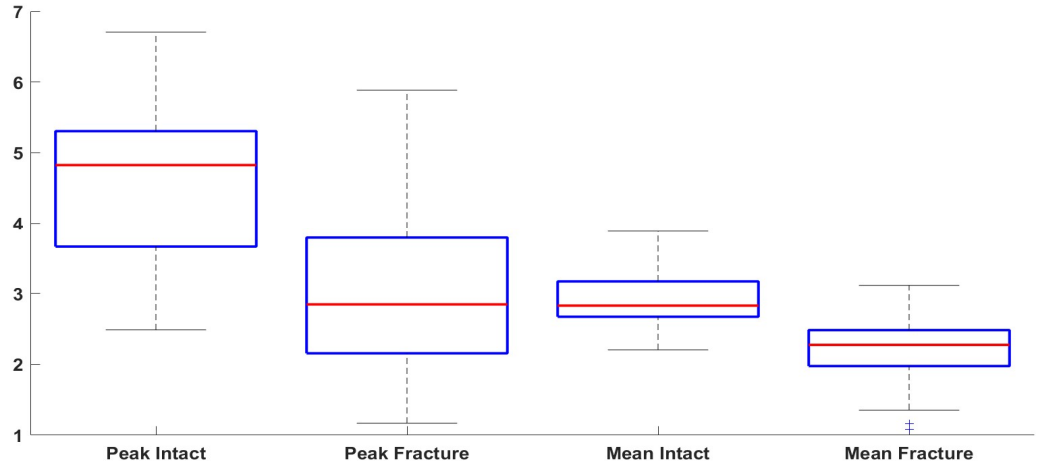

Fig 4.11. Boxplot comparison of axial normal strain elastographic features on intact and fractured vertebrae.

Mann-Whitney U tests were performed to assess statistical significance in contrasting the intact and fractured samples in the form of both axial shear (positive and negative if bipolar) and axial

normal strains at the vertebra-soft tissue interface. Our results from the axial shear strain elastogram boxplots in Fig 10 show that peak values of positive strains ($Z = 4.76$, $p = 9.7\times10^{-7}$) and negative strains ($Z = 3.56$, $p = 1.8\times10^{-4}$) from intact cases are higher than the fracture cases. Mean values of positive ($Z = 4.23$, $p = 1.2\times10^{-5}$) and negative strains ($Z = 2.92$, $p = 0.0017$) are also higher for intact cases. The axial normal strain elastogram boxplots in Fig 4.11 show that both peak ($Z = 5.1$, $p = 1.7\times10^{-7}$) and mean ($Z = 6.18$, $p = 3.2\times10^{-10}$) values are higher for intact cases.

Number of bipolar/unipolar strains	Mean± Standard Deviation (mm/mm)	p-value
Intact vertebra	2.67 ± 0.48	2.06×10^{-6}
Fractured vertebra	3.39 ± 0.69	

Table 4.2. Paired t-test comparing the total number of bipolar and unipolar strains within each axial slice for intact and fractured vertebrae.

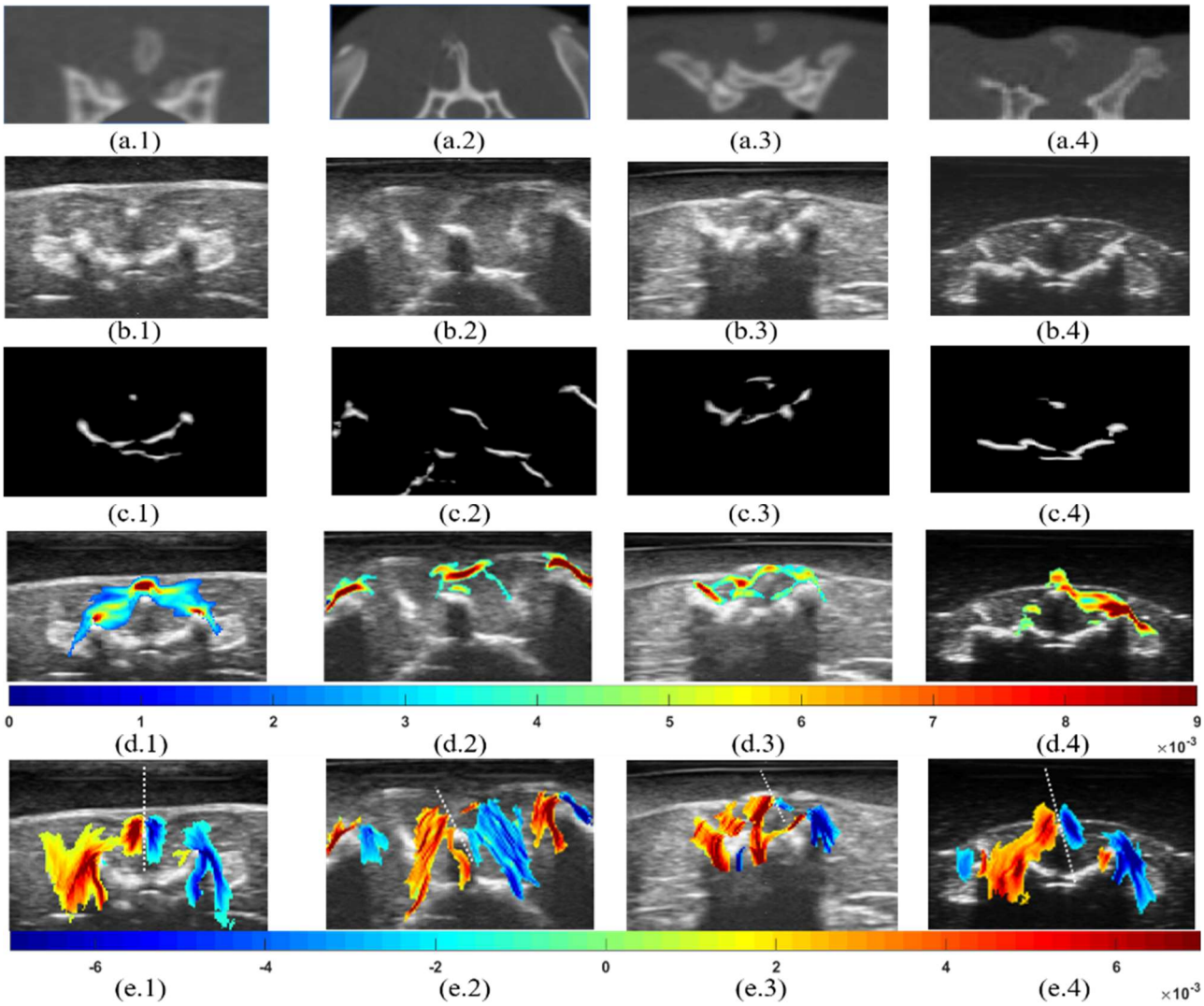

Fig 4.12: The first column shows an axial slice from the L3 intact vertebra, the second, third and fourth columns show vertebra with a fractured L7 SP, fractured L4 SP and left AP and fractured L5 SP and AP respectively. a) CT axial slices. b) Corresponding ultrasound B-mode images. c) Segmented posterior spine from B-mode images. d) Composite axial normal strain and e) Composite axial shear strain elastograms with principal orientation highlighted on the B-mode images respectively.

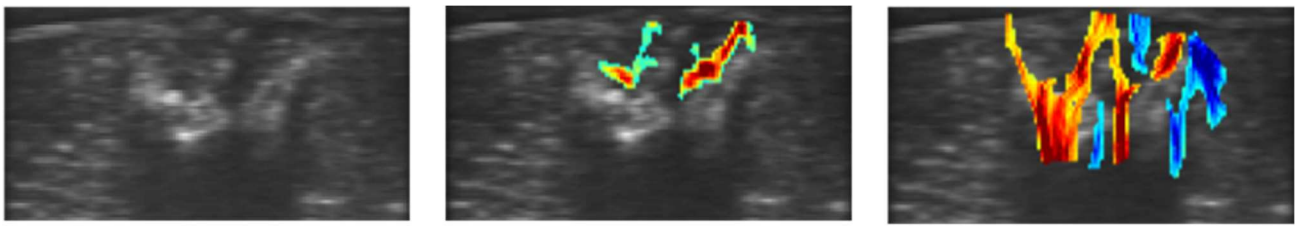

(a) (b) (c)

Fig 4.23. Axial slice of fractured vertebra without the phantom. a) B-mode image b) Composite axial normal strain elastogram and c) Composite axial shear strain elastogram on the B-mode images respectively.

In Fig 4.12, the first two rows indicate the CT slices and corresponding B-mode images. Bony regions segmented from the B-mode images are displayed in the third row. The fourth and fifth rows illustrate the respective axial normal and axial shear strains composited onto their B-mode images. The first column shows slices obtained from an intact rabbit (vertebra and strain projection shown in Fig 4.6a). The second column (vertebra and strain projection shown in Fig 4.6b) shows a single SP fracture along with an intact illiac crest. Slices corresponding to fractures on the SP and left AP are observed in the third (vertebra and strain projection shown in Fig 4.6c) and fourth columns respectively. The intact slice in column 1 shows a larger degree of symmetrical axial normal strain concentration on the left and right AP. Whereas the tilt signifying a fractured SP is quite prominent in the axial shear strain elastograms among columns 2-4 from which our descriptor can be easily obtained compared to the automatically extracted SP in the third row. In particular, Fig 4.13 shows the axial slice of the same sample as present in column 3 of Fig 4.12 in the absence of the phantom. In this case, the transducer was coupled directly with the soft tissue surface through a gel pad. From the segmented axial shear strain

elastogram the orientation estimation of the SP fragment remains consistent with and without the gelatin-agar phantom. In general, the strain morphology at the vertebra-soft tissue boundary is similar across simulation and experimental results. In fact, the 3rd column of Fig 4.5, 4.6 and 4.12 and Fig 4.13 correspond to the same vertebra, and the SP orientations reflected by the axial shear strain elastograms are in line with each other. Also, oblique axial normal strain around the left AP is consistently seen in all the figures. Wilcoxon signed rank test further showed an asymmetrical experimental axial normal strain distribution for spine fractures (Intact: $p = 0.74$, Fracture: $z = -2.79$, $p = 0.0052$).

4.4 DISCUSSION

Spine injuries and abnormalities such as fractures have been an active area of research for many decades [91]. In most cases, spinal injury due to fracture are associated with changes of mechanical properties of the tissue at the bone interface [92]. In this paper, we focus on the thoracolumbar posterior column alone for garnering fracture information. Our hypothesis is that the distinction between intact and fractured vertebrae can be manifested in the morphology and statistics of the strain distribution. As our means of investigation, both FE-based elastography simulations and actual experiments were conducted. To the best of our knowledge, this is the first study of its kind that employs a mechanical model framework in assessing the vertebra-soft tissue boundary. Although a finite element (FE) model-based approach has been employed for differentiating intact and fractured long bones, it has yet to be applied for spinal injuries [90]. Such a framework facilitates a crucial first step in characterizing strain fields that would help make inferences about mechanical behavior of vertebra/soft tissue interface and surrounding ligaments, muscles and fat regions. The strains in turn enveloped at the vertebra soft tissue

interface can be a useful adjunct to B-mode images in detecting fractures and localizing the fracture site. Our results report a manifestation of this in the axial strains especially axial shear strain patterns. The elastographic axial strain disruption may convey additional structural information on the spinal protrusions.

To study the vertebra-soft tissue interface using USE, we designed an FE model and subsequent analysis that are specific to the spine morphology. The geometry was imported from the CT of rabbit spines and relevant material properties were assigned. Intact and fracture cases were simulated to replicate the experimental setup. The importance of the availability of a simulation framework in this paper is highlighted by the fact that there are no imaging methods that can be used to directly validate the experimental results. In general, simulated elastograms give an upper bound of the performance of the proposed techniques, which consider some of the limitations inherent to the ultrasonic estimation [93]. The proposed simulation has been shown to produce elastographic features which can uniquely distinguish intact from fractured spines. The feasibility of spine fracture localization has been quantitatively validated using ex-vivo phantom experiments. A qualitative assessment of an experiment without the phantom has also been included. The results obtained from the simulation and experiments are shown to be consistent.

From the intact vertebra-soft tissue interface, a bipolar pattern around each bony protrusion in the axial shear strain elastograms was observed. Symmetric strain distributions were also observed for the same sample in axial normal strain elastograms. On the other hand, complex strain disruption patterns were observed in the axial normal and axial shear strain elastograms after fracture induction. Results show that fracture sites can be localized based on the quantity of

bipolar/unipolar axial shear strains developed around each fracture segment or an altering of the normal strain geometry. Also, in the presence of a fracture, both axial normal and axial shear strain elastograms show a decrease in the mean/peak strain magnitudes in corresponding segmentation areas.

To partially overcome the aforementioned traits' limitation in characterizing fractures which may get complicated by the spine's intrinsic shape, morphological descriptors were introduced to probe some unique strain elastographic features in the vicinity of the fracture zone. Being one candidate of them, the asymmetrical axial normal strain distributions motivated from the 3D median projections was quantified within the axial normal strains obtained experimentally. Intact and fracture cases were demonstrated to have a statistically significant difference in the symmetry descriptor. The experimental results also confirmed the validity of another descriptor, i.e., the principal orientation of the SP. In the form of the deviation from the midline, this quantity becomes minimal for intact cases. And the IQR of the intact experimental cases showed a similar spread to those obtained in the simulations. Meanwhile, thresholds of principal orientation descriptors obtained for the SP from both simulation and experiments were in close agreement. The non-parametric classification used to determine this threshold can be further employed in future in-vivo test cases for automatic determination of SP fractures and possibly in assessing their severity.

A limitation of the study is the use of FE models with simplified geometry. The vertebrae-soft tissue complex involves a network of intrinsic muscles connecting the vertebrae, PLC and at its most superficial level, the thoracolumbar fascia. Simulations incorporating these factors in

trauma induced soft tissue could provide crucial residual strain information enveloped across each tissue layer including the vertebrae-soft tissue interface. This can be helpful in callus tissue differentiation for bone healing applications as simulated in [94]. Additionally, the inclusion of multiple vertebrae for our FE simulations can help visualize important strain characteristics about the PLC (on the sagittal plane) though this imposes a fair amount of structural complexity to the model. Hence, they will be left as a future work. Sagittal plane axial strain elastograms were not investigated in this study because nearly all multiple fractures were visible in a single axial slice from our models. The superior advantages of capturing deeper structural information from the axial plane have been reported [18, 74]. The modeling of soft tissue surrounding the vertebrae as a cuboid is obviously not representative of the actual tissue geometry. We chose such a model to demonstrate feasibility of visualizing axial normal and shear strains in a controlled setup compatible with perfect uniaxial compression. For rabbits (or humans) in direct contact with the transducer, we use a gel pad spacer to achieve near uniaxial compression. However, there could be locations where the transducer plate may not be in complete contact with the rabbit's back which we do not foresee being a problem in humans.

For most US modalities, there is always a concern on the depth of penetration. We used a rabbit model in this study, which is known to have a relatively superficial spine. In humans, the ROI and depth of spine may vary and could be a concern for obese patients. However, using novel US transducers, elastography experiments up to 10 cm have been successfully conducted which we believe should cover most of the relevant scenarios, since we are mainly concerned about the surface mechanics [95].

Freehand ultrasound elastography can pose complications even with the use of a transducer plate. The compression applied as a result cannot be perfectly uniform without a flat surface contact. Moreover, off-plane motion artifacts can also hinder elastographic SNR. One possible solution to this problem can be the involvement of real-time feedback from the correlation maps. Optimal transducer positioning can in turn be achieved by maximizing correlation that can ensure uniaxial compression. Additional hardware in the form of a robotic arm holding the transducer can also maximize repeatability of experimental conditions. This can happen in the form of automatic control for parameters such as constant force application and strain symmetry calibration.

The correlation method for obtaining axial strain elastograms has not been optimized for frame selection. We have consistently chosen the middle 50 successive frames for producing the averaged elastogram to facilitate a level of automation. Improving frame subset selection can be especially critical for in-vivo applications where motion from the animal and operator can introduce elastogram artifacts. Estimation of the inter-frame compression factor using dynamic frame pairing can be used to alleviate this problem [96]. We can also employ other strain estimation techniques such as DPHS [97] and Analytic minimization [98]. But these techniques are prone to excessive regularization that could miss finer structural details.

The shear strain bipolar/unipolar pattern corresponding to each fracture segment cannot be perceived when adjacent strains from dense connective tissues can be merged with strains surrounding bone to form higher strain concentrations. We encounter this possibility in Fig 4.12(e.4) where the merging happens between the polarities around the two left AP fracture

segments. However, we anticipate this happening when the gap between segments fall below the spatial pulse wavelength. Also, the axial width of the lumbar vertebral body of humans is considerably higher (>= 50 mm) than the rabbit (we measured this to be around 15 mm), reducing such a possibility. But, the higher axial width in humans may call for longer width linear array transducers or a 2D transducer capturing multiple planes.

Segmenting strains for fusion with the B-mode images cannot always be determined by the threshold as a function of applied compression or peak strain. This can especially hold true for ex-vivo or in-vivo studies that aren't based on phantom studies where applied compression cannot be approximated. Deeper connective tissue geometries could influence these strain distributions to be within the range of vertebra-soft tissue interface strain values. In such cases, we can isolate the vertebra-soft tissue interface strains by masking the elastograms with attenuation maps derived from the Bmode image as described in our earlier work or using confidence map estimation.

The automatically segmented spine ridges only show surface information as "seen" by the transducer. However, from slippage conditions it is quite apparent that shear strains show to some extent additional quantifiable surface information (from the sides). These are noticeable around protrusions or angled surfaces of the spine as a consequence of the non-zero axial displacement gradients. By virtue of this, SP deviations from the midline can be observed more clearly and thereby reliably quantified from ASSE than a pure B-mode segmentation alone. This is evident in Fig 4.12 (columns 2, 3 and 4) where the SP could be mistaken as being intact when only observing superficial surface information from the B-mode images or the subsequent

automatic segmentation. Multiple studies have used the acoustic shadowing features of the spinous process in classifying scoliotic spine [70,73]. However, the tilted spinous process in Fig 4.12(b.2-4) shows little evidence about the nature of the abnormality owing to the fact that the shadowing occurs roughly parallel to the midline similar to Fig 4.12(b.1).

Although principal orientation has been used for quantifying midline deviation in this paper, it can be applied for other bony protrusions as well. However, AP and TP can contain a wide range of principal orientations among parallel axial slices due to their oblique geometry. As a result, comprehensive principal orientations for such complex bony protrusions need to be captured using a 2D transducer. Models generalized for different bony protrusions can then be constructed using these range measurements. Fracture classification incorporating such models is left for future work. In this paper the principal orientation obtained from the shear strains have not been validated using the orientations attributed to bony protrusions observed in the CT. This necessitates a proper image registration framework for the SP alignment and is also left for future work. Also, an aggregate of principal orientations from both axial and sagittal planes can have implications for cobb angle measurements for discerning scoliotic spines.

Apart from the morphological descriptors, the strain number, mean and peak strain magnitude features were not extracted from experimental elastograms. This is mainly due to the limited sample size used for the in vitro experiments. However, we believe the corresponding trends observed in the simulation will still hold true in practice. It should be noted that the phantom experiments in conjunction with the one conducted on the actual tissue were meant to show in vivo experimental feasibility to highlight the difference between fracture and intact cases. Hence

the findings of the study are qualitative in nature and encourage a more thorough experimental study providing full quantitative assessment. Distinguishing axial normal strain and axial shear strain for intact and fractured vertebrae will hence be substantiated with more realistic in vivo evidences.

4.5 CONCLUSION

In this study we present the first attempt to assess the spine fracture using USE. Both intact and fracture groups were created, elastographically simulated and assessed using actual experiments. Commonly used numerical characteristics were combined with morphological descriptors motivated from the spine's unique 3-D geometry to give a comprehensive evaluation of the two groups' mechanical behavior subjected to the uniaxial compression. The results indicate that it is feasible to image the spine-tissue interface using USE and that equipped with proper descriptors, axial normal strain and axial shear strain maps may be important media to detect spine fractures and make inferences on other spinal abnormalities.

CHAPTER 5

CONCLUSIONS AND FUTURE WORK

Ultrasound imaging of the spine is generally accompanied by multiple bright tissue structures surrounding it such as muscle, fat and ligaments along with challenging noise conditions. This can cloud a physician's perception of the spinal anatomy. This thesis argued for the importance of strongly suppressing the surrounding soft tissue regions and noisy ultrasound artifacts to enable easy isolation and interpretation of bony regions from ultrasound images. The proposed enhancement methods have been predominantly demonstrated for the intact spine but the applicability towards spinal fractures and tibial bone regeneration has also been explored. Although bone surface segmentation and reconstruction techniques have been extensively explored in the previous literature, emphasis on algorithm robustness for a variety of bone anatomy or spinal fractures is lacking. Moreover, state of the art techniques that employ phase information do not emphasize reduction of soft tissue responses.

5.1 CONTRIBUTIONS

The primary contribution of this work is in the robust 3D surface rendering of the posterior vertebral column surfaces. Additionally, ultrasound elastography techniques that exploit surrounding soft tissue deformation are used to highlight the presence and location of fractures. The ideas around generated around this work can be summarized as follows:

- The 2D local phase-symmetry model using a Log-Gabor filter bank of optimized scale and orientation parameters is employed to extract ridge features. But, regions such as dense connective tissues are also extracted as the by-product in this process. Acoustic

shadowing present underneath the spine surfaces is a discriminating aspect of bony regions. These are used to engineer novel intensity-based features which are in turn populated in a feature space for detection of the spine regions. Furthermore, morphological techniques are used to extract a pixel-thick spine surface for validation against manual delineation.

- Overlaying the detected spine surface on the US image in the transverse plane enables easy visualization of the skin to epidural space distance facilitating accurate epidural placement.
- A majority of the structural information about the posterior spine is extracted by virtue of the 3D spine surface rendering. This is generated by the stacking of individual 2D spine surface slices obtaining along a straight line centered on the midline (the location of the SP). Quantitative performance assessment of the algorithm is validated the against manually obtained 3D spine surface delineation.
- Applications to 3D visualization of the long bone regeneration process has been demonstrated. This is performed by extending the 2D local phase-symmetry model to 3D. Further post-processing by concave region filling of the detected bone regions has been proposed for superior smoothing effect. Results from the visualization show discernible stages of ossification which include surface of the native bone and newly formed bone. The scaffold for facilitating bone growth has also been isolated in this process.
- Ultrasound elastography techniques are realized as a robust mechanism for extracting additional structural information from the spine. These are manifested in the form of axial normal and shear strain deformations of the tissue structures surrounding the spine.

Disruption of axial strains show unique patterns that can be a useful adjunct to US B-mode images in highlighting fracture sites.

- Novel strain-based descriptors as a function of the ultrasound elastograms are proposed to quantify the presence of a fracture. Spatial strain distribution asymmetry using axial normal strain elastograms can assess the presence of a fracture. The degree of spinous process deviation from the midline is assessed by axial shear strain elastograms using the principal orientation descriptor.

5.2 FUTURE WORK

There are bountiful research possibilities that could stem from this work. In order to improve the performance of the spine surface segmentation, we will have to revisit the Log-Gabor filter used for the phase-symmetry model. The broad bandwidth of Log-Gabor filters provides maximal spectral coverage, and the zero DC value ensures maximal spatial localization [63]. Phase-based estimation of ridges is robust to intensity variations in the B-mode image but remains intrinsically noisy. This results in a less than ideal situation for fracture detection where in some cases, the ridges detect an intact surface instead of a fracture. In such cases, it may be worth investigating the choice of quadrature filter such as a Cauchy, Deriche, Gaussian Derivative or a Difference of Gaussian filter kernel (that also possess zero DC values) used for the phase-symmetry model. Fixed parameters such as number of scales, orientations, angular bandwidth coupled with can be adjusted to improve the spine ridge feature strength. Thus, the study can be extended to a general framework that optimizes for the kernel and its associated parameter vector based on ridge feature strength mentioned in Chapter 1. The robustness of such a framework can be advantageous for identification of both multiple bone anatomies and fractures. This

framework can also be extended using 3D local phase symmetry features as demonstrated in this thesis for bone regeneration applications. However, a significant computational expense was observed for the 3D radon transform computation. Other groups have seemingly tackled this computational load problem with a possibility of parallelization by GPUs [57].

The quantitative assessment of the surface rendering can be better validated using alternate modalities with superior resolution rather than reliance on a manual segmentation approach. One avenue that can open of plethora of possibilities for accurate 3D reconstruction is pose estimation. Scanning for volumetric ultrasound data can be done in conjunction with a position sensing device to map the US imaging planes to the alternate coordinate system. This can be invaluable for validation studies involving CT by fiducial marker placement [45-46]. Multiple studies have also demonstrated a 3D registration scheme for intraoperative scenarios. Position sensors can also be important for producing an accurate 3D rendering of the entire vertebral column by virtue of volume stitching techniques.

The value of the strain-based shape descriptors from ultrasound elastography can be significantly boosted with the advent of 2D transducers. By observing the deviation of the protrusions on the posterior spine, various fracture types can be identified. This can be achieved due to principal orientation evaluation in both axial and sagittal planes. Moreover, this also has implications for a comprehensive strain distribution symmetry assessment for the stability of the spine. Such information can be a boon for surgeons' decision to undergo surgical intervention.

Finally, an intelligent feature selection strategy involving elastographic deformation gradient components, phase-based features, intensity-based shadowing features can be used to compute a

probabilistic estimate of the spinal fracture. Such an estimate can be fused with the 3D spine surface rendering. This produces an enhanced 3D visualization of the posterior vertebral column with highlighted fractures.

REFERENCES

[1] J. Crim, K. Moore and D. Brodke, "Clearance of the cervical spine in multitrauma patients: The role of advanced imaging", *Seminars in Ultrasound, CT and MRI*, vol. 22, no. 4, pp. 283-305, 2001.

[2] Schaefer, D.M., Flanders, A.E., Osterholm, J.L. and Northrup, B.E., 1992. Prognostic significance of magnetic resonance imaging in the acute phase of cervical spine injury. *Journal of neurosurgery*, *76*(2), pp.218-223.

[3] An, H.S., Andreshak, T.G., Nguyen, C., Williams, A. and Daniels, D., 1995. Can we distinguish between benign versus malignant compression fractures of the spine by magnetic resonance imaging?. *Spine*, *20*(16), pp.1776-1782.

[4] Hadley, M.N., Zabramski, J.M., Browner, C.M., Rekate, H. and Sonntag, V.K., 1988. Pediatric spinal trauma: review of 122 cases of spinal cord and vertebral column injuries. *Journal of neurosurgery*, *68*(1), pp.18-24.

[5] Tator, C.H. and Fehlings, M.G., 1991. Review of the secondary injury theory of acute spinal cord trauma with emphasis on vascular mechanisms. *Journal of neurosurgery*, *75*(1), pp.15-26.

[6] Sharif, H.S., 1992. Role of MR imaging in the management of spinal infections. *AJR. American journal of roentgenology*, *158*(6), pp.1333-1345.

[7] Ford, J.C., Hackney, D.B., Alsop, D.C., Jara, H., Joseph, P.M., Hand, C.M. and Black, P., 1994. MRI characterization of diffusion coefficients in a rat spinal cord injury model. *Magnetic resonance in medicine, 31*(5), pp.488-494.

[8] Mettler Jr, F.A., Wiest, P.W., Locken, J.A. and Kelsey, C.A., 2000. CT scanning: patterns of use and dose. *Journal of radiological Protection, 20*(4), p.353.

[9] Goske, M.J., Applegate, K.E., Boylan, J., Butler, P.F., Callahan, M.J., Coley, B.D., Farley, S., Frush, D.P., Hernanz-Schulman, M., Jaramillo, D. and Johnson, N.D., 2008. The 'Image Gently'campaign: increasing CT radiation dose awareness through a national education and awreness program. *Pediatric radiology, 38*(3), pp.265-269.

[10] Hu, W.W., Ward, B.B., Wang, Z. and Krebsbach, P.H., 2010. Bone regeneration in defects compromised by radiotherapy. *Journal of dental research, 89*(1), pp.77-81.

[11] Giordano, B.D., Grauer, J.N., Miller, C.P., Morgan, T.L. and Rechtine, G.R., 2011. Radiation exposure issues in orthopaedics. *JBJS, 93*(12), p.e69.

[12] Biswas, D., Bible, J.E., Bohan, M., Simpson, A.K., Whang, P.G. and Grauer, J.N., 2009. Radiation exposure from musculoskeletal computerized tomographic scans. *JBJS, 91*(8), pp.1882-1889.

[13] Rampersaud, Y.R., Foley, K.T., Shen, A.C., Williams, S. and Solomito, M., 2000. Radiation exposure to the spine surgeon during fluoroscopically assisted pedicle screw insertion. *Spine, 25*(20), pp.2637-2645.

[14] Tran, D., & Rohling, R. N. (2010). Automatic detection of lumbar anatomy in ultrasound images of human subjects. *Biomedical Engineering, IEEE Transactions on, 57*(9), 2248-2256.

[15]Tran, D., Kamani, A. A., Lessoway, V. A., Peterson, C., Hor, K. W., & Rohling, R. N. (2009). Preinsertion paramedian ultrasound guidance for epidural anesthesia. *Anesthesia & Analgesia, 109*(2), 661-667.

[16] Grau, T., Leipold, R. W., Fatehi, S., Martin, E., & Motsch, J. (2004). Real-time ultrasonic observation of combined spinal–epidural anaesthesia. *European journal of anaesthesiology, 21*(01), 25-31.

[17] Karmakar, M. K., Li, X., Ho, A. H., Kwok, W. H., & Chui, P. T. (2009). Real-time ultrasound-guided paramedian epidural access: evaluation of a novel in-plane technique. *British journal of anaesthesia, 102*(6), 845-854.

[18]Arzola, C., Davies, S., Rofaeel, A., & Carvalho, J. C. (2007). Ultrasound using the transverse approach to the lumbar spine provides reliable landmarks for labor epidurals. *Anesthesia & Analgesia*, *104*(5), 1188-1192.

[19] Rasoulian, A., Rohling, R. N., & Abolmaesumi, P. (2012, February). Probabilistic registration of an unbiased statistical shape model to ultrasound images of the spine. In *SPIE Medical Imaging* (pp. 83161P-83161P). International Society for Optics and Photonics.

[20] Martin, B.I., Mirza, S.K., Comstock, B.A., Gray, D.T., Kreuter, W. and Deyo, R.A., 2007. Reoperation rates following lumbar spine surgery and the influence of spinal fusion procedures. *Spine*, *32*(3), pp.382-387.

[21] Cho, K.J., Suk, S.I., Park, S.R., Kim, J.H., Kim, S.S., Choi, W.K., Lee, K.Y. and Lee, S.R., 2007. Complications in posterior fusion and instrumentation for degenerative lumbar scoliosis. *Spine*, *32*(20), pp.2232-2237.

[22] Hacihaliloglu, I., 2010. *Towards a novel minimally invasive three dimensional ultrasound imaging based computer assisted orthopaedic surgery system for bone fracture reduction* (Doctoral dissertation, University of British Columbia).

[23] Denis, F., 1984. Spinal instability as defined by the three-column spine concept in acute spinal trauma. *Clinical orthopaedics and related research*, *189*, pp.65-76.

[24] Lee, H.M., Kim, H.S., Kim, D.J., Suk, K.S., Park, J.O. and Kim, N.H., 2000. Reliability of magnetic resonance imaging in detecting posterior ligament complex injury in thoracolumbar spinal fractures. *Spine*, *25*(16), pp.2079-2084.

[25] Claes, L.E. and Cunningham, J.L., 2009. Monitoring the mechanical properties of healing bone. *Clinical Orthopaedics and Related Research®*, *467*(8), pp.1964-1971.

[26] Rajpoot, K., Grau, V. and Noble, J.A., 2009, June. Local-phase based 3d boundary detection using monogenic signal and its application to real-time 3-d echocardiography images. In *Biomedical Imaging: From Nano to Macro, 2009. ISBI'09. IEEE International Symposium on* (pp. 783-786). IEEE.

[27] Felsberg, M. and Sommer, G., 2001. The monogenic signal. *IEEE Transactions on Signal Processing*, *49*(12), pp.3136-3144.

[28] Chin, K. J., Perlas, A., Chan, V., Brown-Shreves, D., Koshkin, A., & Vaishnav, V. (2011). Ultrasound imaging facilitates spinal anesthesia in adults with difficult surface anatomic landmarks. *Anesthesiology*, *115*(1), 94-101.

[29] Mauldin Jr, F. W., Owen, K., & Hossack, J. (2011, October). Three-dimensional spinal bone imaging with medical ultrasound for epidural anesthesia guidance. In *Ultrasonics Symposium (IUS), 2011 IEEE International* (pp. 238-241). IEEE.

[30] Carvalho, J. C. A. (2008). Ultrasound-facilitated epidurals and spinals in obstetrics. *Anesthesiology clinics*, *26*(1), 145-158.

[31] Tumber, S. S., & Liu, H. (2010). Epidural abscess after multiple lumbar punctures for labour epidural catheter placement. *Journal of biomedical research*, *24*(4), 332-335.

[32] Noble, J.A., Navab, N. and Becher, H., 2011. Ultrasonic image analysis and image-guided interventions. *Interface focus*, *1*(4), pp.673-685.

[33] Kowal, J., Amstutz, C., Langlotz, F., Talib, H., & Ballester, M. G. (2007). Automated bone contour detection in ultrasound B-mode images for minimally invasive registration in computer-assisted surgery—an in vitro evaluation. *The International Journal of Medical Robotics and Computer Assisted Surgery*, *3*(4), 341-348.

[34] Beitzel, J., Ahmadi, S. A., Karamalis, A., Wein, W., & Navab, N. (2012, August). Ultrasound bone detection using patient-specific ct prior. In *Engineering in Medicine and Biology Society (EMBC), 2012 Annual International Conference of the IEEE* (pp. 2664-2667). IEEE.

[35] Foroughi, P., Boctor, E., Swartz, M. J., Taylor, R. H., & Fichtinger, G. (2007, October). P6D-2 ultrasound bone segmentation using dynamic programming. In *Ultrasonics Symposium, 2007. IEEE* (pp. 2523-2526). IEEE.

[36] Lopez-Perez, L., Lemaitre, J., Alfiansyah, A., & Bellemare, M. E. (2007, December). Bone surface reconstruction using localized freehand ultrasound imaging. In *Conference proceedings:... Annual International Conference of the IEEE Engineering in Medicine and Biology Society.* (Vol. 2008, pp. 2964-2967).

[37] Alfiansyah, A., Ng, K. H., & Lamsudin, R. (2009, January). Deformable model for serial ultrasound images segmentation: application to computer assisted hip athroplasty. In *13th International Conference on Biomedical Engineering* (pp. 1073-1076). Springer Berlin Heidelberg.

[38] Wen, X., & Salcudean, S. E. (2007, October). P6D-5 Enhancement of Bone Surface Visualization Using Ultrasound Radio-Frequency Signals. In*Ultrasonics Symposium, 2007. IEEE* (pp. 2535-2538). IEEE.

[39] Doctor, A., B. Vondenbusch, and J. Kozak. "Bone segmentation applying rigid bone position and triple shadow check method based on RF data." *Acta of Bioengineering and Biomechanics* 13.2 (2011): 3-11.

[40] Hussain, M.A., Hodgson, A.J. and Abugharbieh, R., 2017. Strain-initialized robust bone surface detection in 3-D ultrasound. *Ultrasound in Medicine and Biology*, *43*(3), pp.648-661.

[41] Hacihaliloglu, I., Abugharbieh, R., Hodgson, A. J., & Rohling, R. N. (2009). Bone surface localization in ultrasound using image phase-based features. *Ultrasound in medicine & biology, 35*(9), 1475-1487.

[42] Hacihaliloglu, I., Abugharbieh, R., Hodgson, A., & Rohling, R. (2009). Automatic data-driven parameterization for phase-based bone localization in US using log-gabor filters. In *Advances in Visual Computing* (pp. 944-954). Springer Berlin Heidelberg.

[43] Khallaghi, S., Mousavi, P., Gong, R.H., Gill, S., Boisvert, J., Fichtinger, G., Pichora, D., Borschneck, D. and Abolmaesumi, P., 2010, September. Registration of a statistical shape model of the lumbar spine to 3D ultrasound images. In *International Conference on Medical Image Computing and Computer-Assisted Intervention* (pp. 68-75). Springer, Berlin, Heidelberg.

[44] Behnami, D., Seitel, A., Rasoulian, A., Anas, E.M.A., Lessoway, V., Osborn, J., Rohling, R. and Abolmaesumi, P., 2016. Joint registration of ultrasound, CT and a shape+ pose statistical model of the lumbar spine for guiding anesthesia. *International journal of computer assisted radiology and surgery*, *11*(6), pp.937-945.

[45] Rasoulian, A., Rohling, R. and Abolmaesumi, P., 2013. Lumbar spine segmentation using a statistical multi-vertebrae anatomical shape+ pose model. *IEEE transactions on medical imaging*, *32*(10), pp.1890-1900.

[46] Nagpal, S., Abolmaesumi, P., Rasoulian, A., Hacihaliloglu, I., Ungi, T., Osborn, J., Lessoway, V.A., Rudan, J., Jaeger, M., Rohling, R.N. and Borschneck, D.P., 2015. A multi-vertebrae CT to US registration of the lumbar spine in clinical data. *International journal of computer assisted radiology and surgery*, *10*(9), pp.1371-1381.

[47] Hacihaliloglu, I., Rasoulian, A., Rohling, R.N. and Abolmaesumi, P., 2014. Local phase tensor features for 3-D ultrasound to statistical shape+ pose spine model registration. *IEEE transactions on Medical Imaging*, *33*(11), pp.2167-2179.

[48] Yu, S., Tan, K. K., Sng, B. L., Li, S., & Sia, A. T. H. (2014). Automatic identification of needle insertion site in epidural anesthesia with a cascading classifier. *Ultrasound in medicine & biology*, *40*(9), 1980-1990.

[49] Berton, F., Cheriet, F., Miron, M.C. and Laporte, C., 2016. Segmentation of the spinous process and its acoustic shadow in vertebral ultrasound images. *Computers in biology and medicine*, *72*, pp.201-211.

[50] Loizou, C. P., Pattichis, C. S., Christodoulou, C. I., Istepanian, R. S., Pantziaris, M., & Nicolaides, A. (2005). Comparative evaluation of despeckle filtering in ultrasound imaging of the carotid artery. *Ultrasonics, Ferroelectrics, and Frequency Control, IEEE Transactions on*, *52*(10), 1653-1669.

[51] P. Kovesi, "Symmetry and Asymmetry from Local Phase," Proc.10th Australian Joint Conf. Artificial Intelligence, 1997.

[52] Kovesi, P., 1999. Phase preserving denoising of images. *signal*, *4*(1).

[53] Bresenham, J.E., 1965. Algorithm for computer control of a digital plotter. *IBM Systems journal*, *4*(1), pp.25-30.

[54] Jain, A. K., & Taylor, R. H. (2004, April). Understanding bone responses in B-mode ultrasound images and automatic bone surface extraction using a bayesian probabilistic framework. In *Medical Imaging 2004* (pp. 131-142). International Society for Optics and Photonics.

[55]] Daanen, V., Tonetti, J., & Troccaz, J. (2004). A fully automated method for the delineation of osseous interface in ultrasound images. In *Medical Image Computing and Computer-Assisted Intervention–MICCAI 2004* (pp. 549-557). Springer Berlin Heidelberg.

[56] Jia, R., Mellon, S.J., Hansjee, S., Monk, A.P., Murray, D.W. and Noble, J.A., 2016, April. Automatic bone segmentation in ultrasound images using local phase features and dynamic programming. In *Biomedical Imaging (ISBI), 2016 IEEE 13th International Symposium on* (pp. 1005-1008). IEEE.

[57] Amir-Khalili, A., Abugharbieh, R. and Hodgson, A.J., 2013. USING GRAPHICS PROCESSING UNITS TO ENABLE REAL-TIME BONE SURFACE EXTRACTION FROM VOLUMETRIC MEDICAL ULTRASOUND IMAGE DATA USING LOCAL PHASE FEATURES. Bone Joint J, 95(SUPP 28), pp.6-6.

[58] Nicholson, P.H.F., Müller, R., Lowet, G., Cheng, X.G., Hildebrand, T., Rüegsegger, P., Van der Perre, G., Dequeker, J. and Boonen, S., 1998. Do quantitative ultrasound measurements reflect structure independently of density in human vertebral cancellous bone?. *Bone*, *23*(5), pp.425-431.

[59] Gregg, E.W., Kriska, A.M., Salamone, L.M., Roberts, M.M., Aderson, S.J., Ferrell, R.E., Kuller, L.H. and Cauley, J.A., 1997. The epidemiology of quantitative ultrasound: a review of the relationships with bone mass, osteoporosis and fracture risk. *Osteoporosis international*, *7*(2), pp.89-99.

[60] Buckland, D.M., 2011. *Ultrasound imaging of cervical spine motion for extreme acceleration environments* (Doctoral dissertation, Massachusetts Institute of Technology).

[61] Hacihaliloglu, I., Guy, P., Hodgson, A.J. and Abugharbieh, R., 2014. Volume-specific parameter optimization of 3D local phase features for improved extraction of bone surfaces in ultrasound. *The International Journal of Medical Robotics and Computer Assisted Surgery*, *10*(4), pp.461-473.

[62] Zhou, G.Q., Jiang, W., Lai, K.L. and Zheng, Y.P., 2017. Automatic Measurement of Spine Curvature on 3-D Ultrasound Volume Projection Image with Phase Features. *IEEE Transactions on Medical Imaging*.

[63] Berton, F., Azzabi, W., Cheriet, F. and Laporte, C., 2015, July. Automatic segmentation of vertebrae in ultrasound images. In *International Conference Image Analysis and Recognition* (pp. 344-351). Springer, Cham.

[64] Ungi, T., King, F., Kempston, M., Keri, Z., Lasso, A., Mousavi, P., Rudan, J., Borschneck, D.P. and Fichtinger, G., 2014. Spinal curvature measurement by tracked ultrasound snapshots. *Ultrasound in medicine & biology*, 40(2), pp.447-454.

[65] Myronenko, A. and Song, X., 2010. Point set registration: Coherent point drift. *IEEE transactions on pattern analysis and machine intelligence*, 32(12), pp.2262-2275.

[66] Lee, S.H. and Shin, H., 2007. Matrices and scaffolds for delivery of bioactive molecules in bone and cartilage tissue engineering. *Advanced drug delivery reviews*, 59(4-5), pp.339-359.

[67] Jegoux, F., Malard, O., Goyenvalle, E., Aguado, E. and Daculsi, G., 2010. Radiation effects on bone healing and reconstruction: interpretation of the literature. *Oral Surgery, Oral Medicine, Oral Pathology, Oral Radiology, and Endodontology*, 109(2), pp.173-184.

[68] Cao, X., Wu, X., Frassica, D., Yu, B., Pang, L., Xian, L., Wan, M., Lei, W., Armour, M., Tryggestad, E. and Wong, J., 2011. Irradiation induces bone injury by damaging bone marrow microenvironment for stem cells. *Proceedings of the National Academy of Sciences*, *108*(4), pp.1609-1614.

[69] H. Rafii-Tari, V. Lessoway, A. Kamani, P. Abolmaesumi and R. Rohling, "Panorama Ultrasound for Navigation and Guidance of Epidural Anesthesia", *Ultrasound in Medicine & Biology*, vol. 41, no. 8, pp. 2220-2231, 2015.

[70] D. Nguyen, Q. Vo, L. Le and E. Lou, "Validation of 3D surface reconstruction of vertebrae and spinal column using 3D ultrasound data – A pilot study", *Medical Engineering & Physics*, vol. 37, no. 2, pp. 239-244, 2015.

[71] S. Yu, K. Tan, B. Sng, S. Li and A. Sia, "Automatic Identification of Needle Insertion Site in Epidural Anesthesia with a Cascading Classifier", *Ultrasound in Medicine & Biology*, vol. 40, no. 9, pp. 1980-1990, 2014.

[72] F. Berton, F. Cheriet, M. Miron and C. Laporte, "Segmentation of the spinous process and its acoustic shadow in vertebral ultrasound images", *Computers in Biology and Medicine*, vol. 72, pp. 201-211, 2016.

[73] C. Cheung, G. Zhou, S. Law, T. Mak, K. Lai and Y. Zheng, "Ultrasound Volume Projection Imaging for Assessment of Scoliosis", *IEEE Transactions on Medical Imaging*, vol. 34, no. 8, pp. 1760-1768, 2015.

[74] P. Shajudeen and R. Righetti, "Spine surface detection from local phase-symmetry enhanced ridges in ultrasound images", *Medical Physics*, vol. 44, no. 11, pp. 5755-5767, 2017.

[75] Hacihaliloglu, R. Abugharbieh, A. Hodgson, R. Rohling and P. Guy, "Automatic Bone Localization and Fracture Detection from Volumetric Ultrasound Images Using 3-D Local Phase Features", *Ultrasound in Medicine & Biology*, vol. 38, no. 1, pp. 128-144, 2012.

[76] B. Parmar, W. Longsine, E. Sabonghy, A. Han, E. Tasciotti, B. Weiner, M. Ferrari and R. Righetti, "Characterization of controlled bone defects using 2D and 3D ultrasound imaging techniques", *Physics in Medicine and Biology*, vol. 55, no. 16, pp. 4839-4859, 2010.

[77] D. Kim, N. Shanti, M. Tantorski, J. Shaw, L. Li, J. Martha, A. Thomas, S. Parazin, T. Rencus and B. Kwon, "Association between degenerative spondylolisthesis and spinous process fracture after interspinous process spacer surgery", *The Spine Journal*, vol. 12, no. 6, pp. 466-472, 2012.

[78] J. Ophir, S. Alam, B. Garra, F. Kallel, E. Konofagou, T. Krouskop and T. Varghese, "Elastography: Ultrasonic estimation and imaging of the elastic properties of tissues", *Proceedings of the Institution of Mechanical Engineers, Part H: Journal of Engineering in Medicine*, vol. 213, no. 3, pp. 203-233, 1999.

[79] A. Itoh, E. Ueno, E. Tohno, H. Kamma, H. Takahashi, T. Shiina, M. Yamakawa and T. Matsumura, "Breast Disease: Clinical Application of US Elastography for Diagnosis", *Radiology*, vol. 239, no. 2, pp. 341-350, 2006.

[80] U. Zaleska-Dorobisz, K. Kaczorowski, A. Pawluś, A. Puchalska and M. Inglot, "Ultrasound Elastography – Review of Techniques and its Clinical Applications", *Advances in Clinical and Experimental Medicine*, vol. 23, pp. 645-655, 2014.

[81] A. Thitaikumar and J. Ophir, "Effect of Lesion Boundary Conditions on Axial Strain Elastograms: A Parametric Study", *Ultrasound in Medicine & Biology*, vol. 33, no. 9, pp. 1463-1467, 2007.

[82] R. Righetti, J. Ophir, S. Srinivasan and T. Krouskop, "The feasibility of using elastography for imaging the Poisson's ratio in porous media", *Ultrasound in Medicine & Biology*, vol. 30, no. 2, pp. 215-228, 2004.

[83] A. Chaudhry, N. Kim, G. Unnikrishnan, S. Nair, J. Reddy and R. Righetti, "Effect of Interstitial Fluid Pressure on Ultrasound Axial Strain and Axial Shear Strain Elastography", *Ultrasonic Imaging*, vol. 39, no. 2, pp. 137-146, 2016.

[84] A. Thitaikumar, L. Mobbs, C. Kraemer-Chant, B. Garra and J. Ophir, "Breast tumor classification using axial shear strain elastography: a feasibility study", *Physics in Medicine and Biology*, vol. 53, no. 17, pp. 4809-4823, 2008.

[85] E. Konofagou, T. Harrigan and J. Ophir, "Shear strain estimation and lesion mobility assessment in elastography", *Ultrasonics*, vol. 38, no. 1-8, pp. 400-404, 2000.

[86] C. Tator and M. Fehlings, "Review of the secondary injury theory of acute spinal cord trauma with emphasis on vascular mechanisms", *Journal of Neurosurgery*, vol. 75, no. 1, pp. 15-26, 1991.

[87] Ford, D. Hackney, D. Alsop, H. Jara, P. Joseph, C. Hand and P. Black, "MRI characterization of diffusion coefficients in a rat spinal cord injury model", *Magnetic Resonance in Medicine*, vol. 31, no. 5, pp. 488-494, 1994

[88] A. Chaudhry, G. Unnikrishnan, J. Reddy, T. A. Krouskop, and R. Righetti, "Effect of Permeability on the Performance of Elastographic Imaging Techniques," *Medical Imaging, IEEE Transactions on,* vol. 32, no. 2, pp. 189-199, 2013.

[89] S. Tang, A. Chaudhry, N. Kim, J. Reddy and R. Righetti, "Effect of bone-soft tissue friction on ultrasound axial shear strain elastography", *Physics in Medicine & Biology*, vol. 62, no. 15, pp. 6074-6091, 2017.

[90] Tang, S., Sabonghy E, Chaudhry, A., Shajudeen P, Islam MT, Kim, N., Cabrera FJ, Reddy, J. N., Tasciotti E & Righetti, R. (2018). A model-based approach to investigate the effect of a long bone fracture on ultrasound strain elastography. *Medical Imaging, IEEE Transactions on*

[91] Stover, S. and P. Fine, *The epidemiology and economics of spinal cord injury.* Spinal Cord, 1987. **25**(3): p. 225-228.

[92] Claes, L. and J. Cunningham, Monitoring the mechanical properties of healing bone. *Clinical Orthopaedics and Related Research*, 2009. 467(8): p. 1964-1971.

[93] R. Desai, T. Krouskop and R. Righetti, "Elastography Using Harmonic Ultrasonic Imaging: A Feasibility Study", *Ultrasonic Imaging*, vol. 32, no. 2, pp. 103-117, 2010.

[94] T. Gardnera, T. Stoll, L. Marks, S. Mishra and M. Knothe Tate, "The influence of mechanical stimulus on the pattern of tissue differentiation in a long bone fracture — an FEM study", *Journal of Biomechanics*, vol. 33, no. 4, pp. 415-425, 2000.

[95] M. Yoneda, E. Thomas, S. Sclair, T. Grant and E. Schiff, "Supersonic Shear Imaging and Transient Elastography With the XL Probe Accurately Detect Fibrosis in Overweight or Obese Patients With Chronic Liver Disease", *Clinical Gastroenterology and Hepatology*, vol. 13, no. 8, pp. 1502-1509.e5, 2015.

[96] R. Xia, G. Tao and A. Thittai, "Dynamic frame pairing in real-time freehand elastography", *IEEE Transactions on Ultrasonics, Ferroelectrics, and Frequency Control*, vol. 61, no. 6, pp. 979-985, 2014.

[97] M. Islam, A. Chaudhry, S. Tang, E. Tasciotti and R. Righetti, "A New Method for Estimating the Effective Poisson's Ratio in Ultrasound Poroelastography", *IEEE Transactions on Medical Imaging*, vol. 37, no. 5, pp. 1178-1191, 2018.

[98] H. Rivaz, E. Boctor, P. Foroughi, R. Zellars, G. Fichtinger and G. Hager, "Ultrasound Elastography: A Dynamic Programming Approach", *IEEE Transactions on Medical Imaging*, vol. 27, no. 10, pp. 1373-1377, 2008.